Characterization of the New Neutron Line at CERN-n_TOF and Study of the Neutron-induced Fission of 237Np

Yonghao Chen

NNT : 2017SACLS204

These de doctorat

de

l'Universite Paris-Saclay

preparee a

l'Universite Paris-Sud

Ecole doctorale n° 576

Particules, Hadrons, Énergie et Noyaux : Instrumentation, Imagerie, Cosmos et Simulation

Spécialité de doctorat: Énergie nucléaire

par

Yonghao Chen

Characterization of the new neutron line at CERN-n_TOF and study of the neutron-induced fission of ^{237}Np

Thèse présentée et soutenue à Orsay, le 8 Septembre 2017.

Composition du Jury :

M,	Ibrahim, Fadi	CNRS (IPNO)	Président
M,	Serot, Olivier	CEA Cadarache	Rapporteur
M,	Morjean, Maurice	GANIL	Rapporteur
M,	Duran Escribano, Ignacio	Université de Saint-Jacques-de-Compostelle	Examinateur
M,	Tang, Jingyu	Académie chinoise des science (IHEP)	Examinateur
M,	Tassan-Got, Laurent	CNRS (IPNO)	Directeur de thèse

Acknowledgements

Standing at the end of my PhD study and looking at the backward path in last three years, I'm impressed by a lot of important moments when I was stepping further with the help from a lot of individuals. I think no one can obtain his or her PhD degree without other people's help. And I did receive a lot of help from a lot of people. I would like to acknowledge these people from the bottom of my heart.

First and foremost, I'd like to express my deepest gratitude to my supervisor Prof. Laurent TASSAN-GOT who is always giving his endless help to me since the very beginning. Laurent is a very nice person and it's always a pleasure to work with him. I'm extremely impressed by his intelligent mind and his rich knowledge in physics, mathematics and computer science. I consequently learned a lot of things from him. In Chinese traditional culture we define a teacher as "one who propagates the doctrine, imparts the professional knowledge, and resolves doubts". This is exactly what Laurent has done to me. I'm always proud of having him and feeling lucky to be his student.

Then I would like to thank all the jury members of my defense. Especially I'd like to thank two reviewers, Prof. Olivier Serot and Prof. Maurice Morjean. They took their holiday time in August to review to my thesis very carefully and gave some good suggestions which finally help me to improve the thesis quality. I'd also like to thank examiner Prof. Jingyu Tang came to my defense from China with a very long trip.

I would like to thank Laurent Audouin who's offering his help to me throughout my PhD period, especially his financial support sending me to the international conference, academic meetings and other professional activities.

These experiences are very important because they can expand my vision and help me to build up professional connections.

I would like to thank n_TOF collaboration at CERN. I did all my experiments at n_TOF which is a unique and strong facility for nuclear data measurement. The collaboration is very efficient and close. I learned a lot of things there which I believe will be very important and helpful for my future career.

I am extremely grateful to all the PACS group members at IPN Orsay. Especially, I thank Claire Le Naour for her outstanding work to make the actinide targets. I thank Marc Ernoult for his good suggestions concerning the manuscript and helpful discussion on physics. I thank Xavier Doligez for his organization for my defense rehearsals and his valuable remarks to the presentation. I thank Alice, Yiman, Coralie and Mingjian for being with me as PhD mates.

I would like to acknowledge all my Chinese friends at Orsay, especially Yaqiong Wang, Zizhao Zong, Yanzhou Wang, Gaoyang Ye, Xing Liu, Yuxiang Song, Zicheng Liu and Yang Wan. Because of your company and help in my personal life, I never felt lonely and helpless and I had a good balance between work and private life in the past three years.

Last but not least, I'd like to give my sincerest appreciation to my family: my parents, my sister and her husband. Thank you very much for your endless love to me. We did not have that much time together since 11 years ago when I entered the university. But I know your hearts were constantly going on with me and you were always on my side to support me. I thank you all more than I can say.

Contents

List of Figures

List of Tables

Chapter 1

Introduction

In this introduction chapter, we will give the motivation of this thesis work respectively on measurement of neutron-induced fission of ^{237}Np and measurement of a new neutron beam line at neutron time-of-flight (n_TOF) facility at CERN. Then we will give a overview of this thesis.

1.1 Motivation

1.1.1 Brief overview of nuclear energy industry

Since the neutron was discovered by James Chadwick in 1932 [1], scientists realized that it would make a good probe of the atomic nucleus. Subsequently, with a series of research work by Fermi, Hahn, Strassman, Meitner and Frisch [2, 3, 4] in late 1930s, fission phenomenon accompanied with release of a large amount of energy was discovered when the Uranium was bombarded with neutrons.

Fermi and his group created the first self-sustaining nuclear chain reaction at University of Chicago in 1942. They transformed scientific theory into technological reality successfully.

From the mid of 20th century, attention was given to harnessing this nuclear energy in some peaceful applications, such as for making electricity. Then, the nuclear energy industry came out and has been undergoing a rapid development in past 70 years.

The world first "nuclear power plant", which is an experimental breeder reactor located in Arco, Idaho, generated electricity to light four 200-watt bulbs on December 20th, 1951. This milestone symbolized the beginning of the nuclear power industry.

The world first large-scale commercial nuclear power plant, located in Shippingport, Pennsylvania, began operation on December 2nd, 1957 and reached its full design power three weeks later.

Since 1960s, several different types of reactors were built and nuclear power industry grew rapidly worldwide. Until January 2017, there are over 440 commercial nuclear power reactors operating in 31 countries, with over 390,000 MWe of total capacity. About 60 more reactors are under construction. They provide over 11% of the world's electricity without carbon dioxide emissions [5]. The use of nuclear energy will probably keep increasing in the future due to its cleaness with respect to dioxide emission and reliability.

1.1.2 Neutron-induced fission cross section of ^{237}Np

^{237}Np is one of the most important minor actinides in spent nuclear fuel since it is a byproduct abundantly produced in present nuclear reactor and it has a long half life (2.14 million years). Therefore it can be considered as a potential target of incineration in fast reactors. This requires a good knowledge of ^{237}Np's behavior under irradiation and in particular its neutron-induced fission properties. Consequently, its fission cross section received a special attention in the last decade and has been measured at different facilities. The recent measurement at CERN n_TOF facility in 2010 [6] indicates some discrepancies by comparison to previous measurements and evaluations.

Figure 1.1 presents the fission cross section of ^{237}Np from fission threshold to 1 GeV, where the n_TOF data is shown together with evaluations and some experiment data as a comparison. It can be seen that the cross section shape of the n_TOF data is identical with evaluations. And the data from Garlea [7], Meadows [8], Marla [9] and Alknazov measured with monoenergetic neutron sources around 14 MeV are also in agreement with n_TOF data within the error bars. Besides, our result is also identical with Jiacoletti's data [10] up to 5 MeV. However, n_TOF data is higher by about 6% above 1 MeV compared with ENDF/B-VII.0 and JENDL-3.3 evaluations. Even larger differences of 8% are found above 6 MeV respecting to JENDL-3.3 evaluation, which is significantly beyond the 3-4% systematic uncertainty of the present data. This singularity of the n_TOF data could shed some doubt on its validity.

Figure 1.2 shows the fission cross section ratio of ^{237}Np relative to ^{235}U where n_TOF data presents discrepancies compared with evaluation data and other mea-

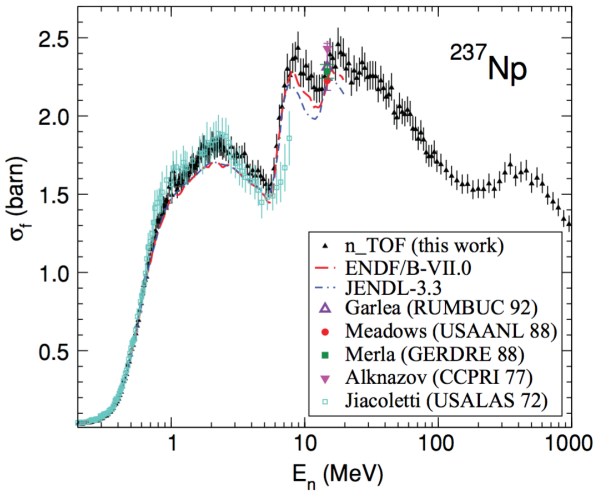

Figure 1.1: The fission cross section of the ^{237}Np from threshold to 1 GeV. - n_TOF data is compared to the ENDF/B-VII.0 and JEFF-3.1 evaluations and some experiment data. The error bars include the statistical and systematic uncertainties. The figure is extracted from [6].

surements. However, some of them are arbitrarily renormalize to each other instead of using an absolute renormalization based on targets' quantities. Tovesson's measurement [11] is normalized by reproducing the ENDF/B-VI ratio at 14.8 MeV since their targets' quantities are not well known, which is finally following the results of Meadows [8]. Shcherbakov's measurement [12] is actually also a shape measurement based on the evaluated data below 14 MeV. Therefore the data based on the absolute fission cross section ratio with a good knowledge of target quantity and detection efficiency are scarce.

A simulation was carried out to check the validity of ^{237}Np fission cross section data measured at n_TOF . A ^{237}Np criticality benchmark experiment performed at Los Alamos [13] was simulated [14]. The simulation predicts a multiplication factor k_{eff} in better agreement with the experiment results when we replace the ENDF/B-VII.0 evaluation of the ^{237}Np fission cross section by the n_TOF data, thus supporting the validity of the latter.

Moreover, a series of measurements relevant to the fission cross section of ^{237}Np have been done recently by P. Salvador-Castiñeira et al [15, 16] at the Van de Graaff facility at JRC-IRMM (Joint Research Center Institute for Reference Materials and

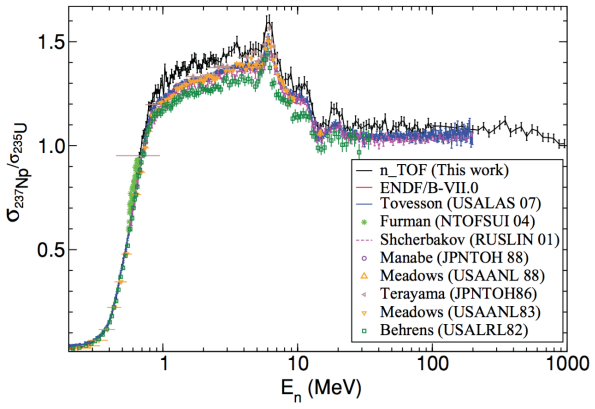

Figure 1.2: The fission cross section ratio of ^{237}Np relative to ^{235}U from threshold to 1 GeV. - n_TOF data is compared to ENDF/B-VII.0 evaluations and some experimental data. The error bars correspond to the statistical uncertainties only. The figure is extracted from [6].

Measurements) by using ^{7}LiF(p, n)^{7}Be and T(p, n)^{3}He neutrons. They use ^{238}U and ^{237}Np as references to measure the fission cross section of ^{240}Pu and ^{242}Pu. For the cross section of ^{237}Np, they use both ENDF/B.VII.1 and n_TOF data [6] as references. They find that n_TOF data leads to a better consistency with existing Pu data.

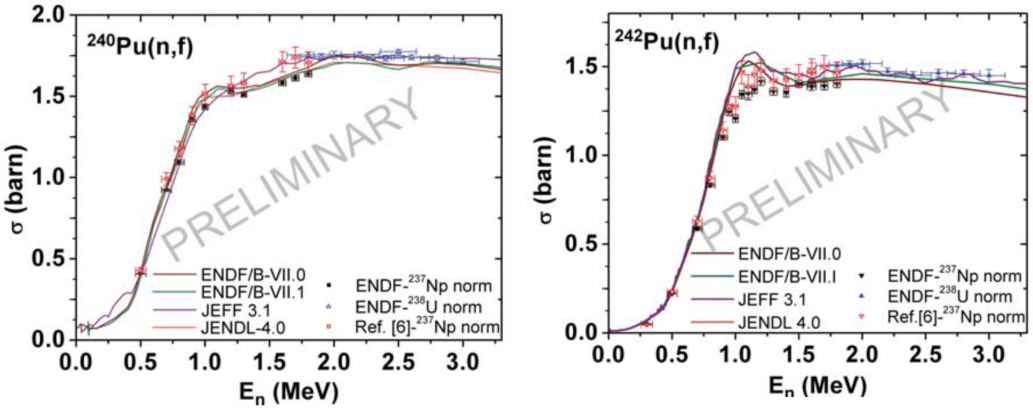

Figure 1.3: Preliminary results on the neutron-induced fission cross section of ^{240}Pu and ^{242}Pu

Figure 1.3 extracted from [15] shows their preliminary results on the fission cross section of ^{240}Pu and ^{242}Pu where the colored curves are the evaluation data. The

symbol dots are the results of their measurements, where the black and blue symbols are obtained by using ENDF/B.VII.1 data of ^{237}Np and ^{238}U respectively as references, the red one is obtained by using n_TOF data (Ref. [6] in figure 1.3). Firstly, we can see that the results based on n_TOF data (red symbols) have a good agreement with the results using ^{238}U (blue symbols) as reference around 1.8 MeV. Whereas, the results based on the ^{237}Np evaluation data (black symbols) present discrepancies compared with the other two results around 1.8 MeV. Additionally, in figure 1.3b, the n_TOF data can reproduce the resonance-like structure around 1 MeV shown in different evaluations. This is not the case when they use ^{237}Np evaluation data.

Following their previous study, Salvador-Castiñeira et al [16] have also measured neutron-induced fission cross section of ^{237}Np, as shown in figure 1.4, by using ^{235}U and ^{238}U as references. The red crosses dataset in figure 1.4 are weighted average results using the data of ^{235}U and ^{238}U in ENDF/B-VII.1 evaluation as references. The green stars dataset are weighted average results obtained by taking the ^{238}U data measured by themselves as reference. We can see clearly that both of them are higher than the evaluations but have an agreement with n_TOF data (black circles) within the error bars.

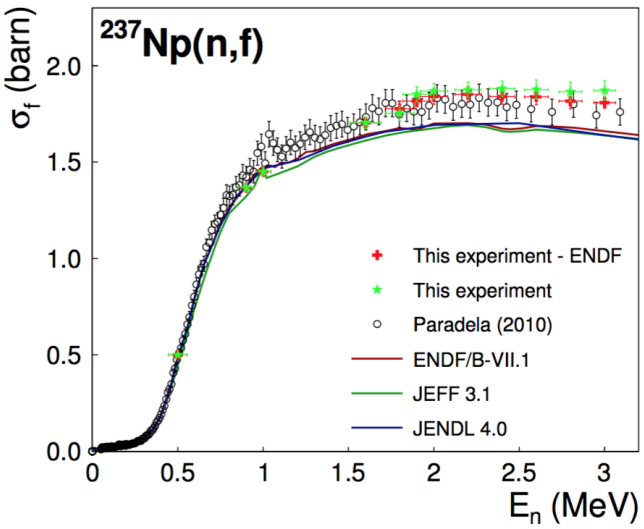

Figure 1.4: Neutron-induced fission cross section of ^{237}Np. - The figure is extracted from [16]

In the above measurement of Salvador-Castiñeira et al [15, 16], their target quan-

tities and detection efficiencies are well known, which means they achieve the absolute cross section ratio instead of using arbitrary renormalization. Therefore the agreement between their results and our n_TOF data is favoring our validity.

From the above discussion and present status we can conclude that a measurement of the absolute fission cross section of ^{237}Np is highly desired to give a definite answer. Therefore we are motivated to measure the absolute fission cross section ratio of ^{237}Np relative to ^{235}U with accurate control on the detection efficiency and target quantities.

1.1.3 Commissioning of a new neutron beam line at n_TOF

A new second experimental area (EAR-2) at CERN n_TOF facility, having a flight path of ∼20 m from the spallation lead target and at 90° degrees with respect to the incoming proton beam, was constructed and under commissioning since 2014. It is offering following advantages compared with the former experimental area 1 (EAR-1): 1) much higher neutron flux (by about a factor of 40) due to its short flight path (EAR-1 has a ∼185 m flight path) and larger solid angle; 2) for highly radioactive samples an additional factor 10 is obtained for the signal to noise ratio due to shorter time interval resulting from the 10 times shorter flight distance [17, 18], thus fulfilling the demands of the neutron science community for a Time-of-Flight (TOF) facility with a higher flux [19].

With the successful commissioning of the EAR-2, it is urgent and important to know its beam property (flux and beam profile) since it is essential for the experimental proposal, design and analysis. The neutron flux is even mandatory to be known in some experiments, for example neutron-capture measurement. Therefore, a precise measurement of EAR-2 neutron flux in a large energy range is indispensable. Our parallel plate avalanche counter (PPAC) detectors are good candidates to perform the beam measurement due to their good time resolution, fast signals and position sensitive ability. That's the reason why we've done this beam measurement for this new neutron line.

1.2 Overview of the thesis

In chapter 1, we introduce the background and motivation of this thesis work.

In chapter 2, the theories about fission model and the fission fragment angular distribution (FFAD) are presented, since fission theory can help us to understand the design of the experimental setup and analysis method. The typical fission models, liquid drop model (macroscopic approach) and the liquid drop model with shell effect correction (macroscopic-microscopic approach), are discussed concerning the deformation and the fission of the nucleus. GEF (GEneral Fission description) code, a semi-empirical model, is also presented since it is a powerful tool to describe the fission. Then a theory on the FFAD taking into account the quantum effect of the nucleus is discussed qualitatively.

In chapter 3, the n_TOF facility at CERN, where the experiments presented in this work took place, is generally presented. The main characteristics of the facility, such as geometric information, flux and energy resolution, are introduced. The high flux, very broad neutron energy spectrum and good energy resolution make n_TOF a unique facility worldwide to measure nuclear data.

In chapter 4, our experimental setups at n_TOF are shown. Firstly, the PPAC and the actinide targets, such as ^{237}Np, ^{238}U and ^{235}U, are described in details. Secondly, the specific setups are shown. In this thesis framework, there are two independent experiments done in different experimental areas. The first experiment is done in EAR-2 for measuring the beam properties (integral neutron flux, beam profile). The second one is in EAR-1 to measure the fission cross section and FFAD of ^{237}Np. Their experimental setups are shown independently.

In chapter 5, the data analysis of beam measurement at EAR-2 is presented in details. The data analysis begins with the raw data treatment. The current programs for treating the raw data are generally depicted. Then, we discuss how we proceed the data analysis specifically as following: i) select the fission events, ii) define the neutron energy, iii) locate the fission fragment and reconstruct the fission trajectory, iv) extract the detection efficiency. Finally we show the results: the integral neutron flux and beam profile of EAR-2.

In chapter 6, we discuss the data analysis of fission of ^{237}Np. The same analysis approach discussed in chapter 5 is applied here to obtain the fission rate and reconstruct the fission trajectory. Then, we present the characteristics of tilted setup which is different from the perpendicular setup described in chapter 5, based on which we extract the FFAD.

In chapter 7, we introduce the method for deducing the cross section and give the first results of ^{237}Np's fission cross section from fission threshold to 5 MeV. It is compared to the evaluation and some other experimental data as well.

In chapter 8, we give the conclusion of the two experiments and present the outlooks of this thesis work.

Chapter 2

Fission theory

To begin with this chapter, we will firstly present three nucleus fission model: the liquid drop model, nuclear shell model and GEF model. Then we will introduce and quantitatively discuss the theory about fission fragment angular distribution.

2.1 Fission model

2.1.1 Liquid drop model

The liquid drop model, which is also referred as macroscopic model, of nucleus was proposed by G. Gamow [20] in 1930 based on the following hypothesis:

- The nuclear fluid is made of nucleons (protons and neutrons), which are held together by the strong nuclear force. Hence it is not compressible.
- Like the liquid drop, the nucleus is compact as a spherical volume due to the surface tension.
- The charge and mass densities of nucleus are homogeneous and constant.

2.1.1.1 Binding energy

Based on the liquid drop model of nucleus, one of the first theory which could describe very well the behavior of the nuclear binding energy and therefore of nuclear mass is the semi-empirical mass formula (SEMF) proposed by C. F. V. Weizsäcker in 1935 [21].

The nuclear binding energy as a function of the mass number A and the number of protons Z can be calculated by SEMF as equation 2.1:

$$E_b(MeV) = a_V A - a_S A^{2/3} - a_C \frac{Z^2}{A^{1/3}} - a_A \frac{(A-2Z)^2}{A} \pm a_\delta A^{-3/4} \tag{2.1}$$

The physical meaning of this equation can be discussed term by term.

(1) Volume term - $a_V A$. The first positive term $a_V A$ is known as the volume term and it is caused by the attracting strong forces between the nucleons. The strong force has a very limited range and a given nucleon may only interact with its direct neighbors. Therefore this term is proportional to A.

(2) Surface term - $a_S A^{2/3}$. The second surface term is also based on the strong force, it is a correction to the volume term. In the volume term, it is suggested that each nucleon interacts with a constant number of nucleons, independent of A. This is true for the nucleons deeply inside the nucleus, but causes an overestimation of the binding energy on the surface since the nucleons on the surface are interacting with less nucleons compared with interior ones. If the volume of the nucleus is proportional to A, then the geometrical radius should be proportional to $A^{1/3}$ and therefore the surface term must be proportional to the surface area which is proportional to $A^{2/3}$.

(3) Coulomb term - $a_C \frac{Z^2}{A^{1/3}}$. The third term describes the Coulomb repulsion between the uniformly distributed protons and is proportional to the number of proton pairs $\frac{Z^2}{R}$, whereby R is proportional to $A^{1/3}$. This effect lowers the binding energy because of the repulsion between protons.

(4) Asymmetry term - $a_A \frac{(A-2Z)^2}{A}$. The fourth term is a quantum correction that is not based on any of the fundamental forces but only based on the Pauli exclusion principle (two fermions cannot occupy exactly the same quantum state in an atom). The heavier nuclei contain more neutrons than protons. These extra neutrons are necessary to stabilize the heavier nuclei. They provide some compensation for the repulsion between the protons. On the other hand, if there are significantly more neutrons than protons in a nucleus, some of the neutrons will be in higher energy level in the nucleus. This is the basis for a correction factor, the so-called asymmetry term.

(5) Pairing term - $a_\delta A^{-3/4}$. The last term is the pairing term who captures the effect of spin-coupling. It is 0 for odd mass nuclei, proportional to $+A^{-3/4}$ for nuclei with an even number of protons and neutrons, and proportional to $-A^{-3/4}$ for nuclei with an odd number of protons and neutrons.

The coefficients of the five terms have units of MeV and can be calculated by fitting to experimentally measured masses of nuclei. They usually depend on the fitting methodology. According to J. W. Rohlf [22] the coefficients in the equation are following:

$$E_b(MeV) = 15.76A - 17.81A^{2/3} - 0.711\frac{Z^2}{A^{1/3}} - 23.7\frac{(A-2Z)^2}{A} \pm 34A^{-3/4} \quad (2.2)$$

2.1.1.2 Nucleus deformation

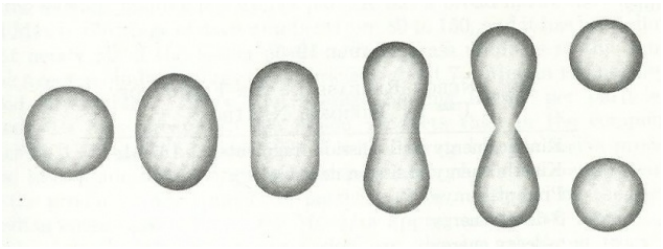

Figure 2.1: The stages of binary fission in a liquid drop model - Energy input deforms the nucleus into a oval, then a dumbbell, followed by binary fission as the two fragments exceed the short-range nuclear force attraction distance, then are pushed apart and away by the Coulomb force. The penultimate drawing corresponds to the scission point.

Bohr and Wheeler studied fission mechanism based on the quadrupole deformation of a liquid drop in 1939 [23]. The radius elongation at deformation can be described as a function of polynomial:

$$R(\theta) = R_0[a_0 + a_2 P_2(cos\theta)] \quad (2.3)$$

where θ is the angle of the radius vector, R_0 is the original radius of the spherical nucleus, a_2 is a parameter quantifying the deformation ($a_2 = 0$ for a sphere) and P_2 is a Legendre second order polynomial.

The overall variation of the energy brought by this deformation is:

$$E_{def} = E_{LDM}(a_2) - E_{LDM}(0) \quad (2.4)$$

where $E_{LDM}(0)$ is the energy of the undistorted sphere, $E_{LDM}(a_2)$ is the energy at deformation status.

According to the liquid drop model the nucleus is incompressible, therefore its volume is not changing at deformation. So the volume term is conserved. Besides, the

asymmetry term and the pairing term are not affected by the deformation neither, because they only depend on the number of the nucleons which are also conserved during deformation. Therefore only surface and Coulomb terms need to be taken into account. The surface and Coulomb energies for small distortion are [23]:

$$\begin{aligned} E_S(a_2) &= E_S(0)(1 + \frac{2}{5}a_2^2) \\ E_C(a_2) &= E_C(0)(1 - \frac{1}{5}a_2^2) \end{aligned} \tag{2.5}$$

where $E_S(0)$ and $E_C(0)$ are the surface and Coulomb energies of the undistorted sphere.

Based on equation 2.4 and equation 2.5, the deformation energy is:

$$\begin{aligned} E_{def}(a_2) &= E_S(a_2) + E_C(a_2) - E_S(0) - E_C(0) \\ &= \frac{2}{5}a_2^2 E_S(0) - \frac{1}{5}a_2^2 E_C(0) \end{aligned} \tag{2.6}$$

With the deformation of the nucleus, the surface energy is increasing because any deformation results in a larger surface, whereas the Coulomb energy is decreasing since the average distance between protons is increasing. Therefore these two terms compete along the deformation. The deformed nucleus is able to return to the undistorted shape when the potential energy of a spherical nucleus is lower than the deformed one, i.e. $E_{def} > 0$, since the nucleus always tends to have the lowest potential energy. Otherwise, the nucleus will stay at this deformation or even go to further deformation and undergo fission. Therefore the stability of a spherical nucleus is given by $E_{def} > 0$ which is equal to $E_C(0) < 2E_S(0)$. This leads to the definition of the fissility parameter:

$$x = \frac{E_C(0)}{2E_S(0)} \simeq \frac{1}{50}\frac{Z^2}{A} \tag{2.7}$$

from which we can see that nuclei with $Z^2/A > 50$ are unstable against even small deformation. It is confirmed by the fact that when the fissility parameter is close to 1, only a small deformation is needed to go to the critical state for the fission, as presented in figure 2.2. It can be seen in figure 2.2 that with the decrease of fissility parameter, a higher deformation is needed to reach the saddle point and finally go to fission, which means more external energy is needed by the nuclei of low fissilities to undergo fission.

As depicted in in figure 2.3, the deformation energy of the nucleus is a net outcome of both changes in the surface energy and Coulomb energy. It reaches a maximum value at a certain deformation (Δ in the figure), which is the critical state for fission

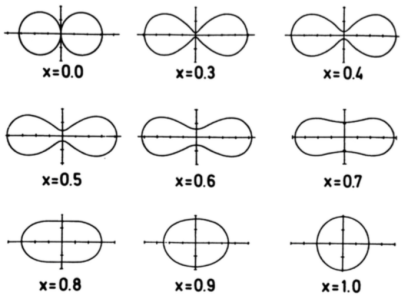

Figure 2.2: Nuclear shapes at the saddle point for various values of x - The figure is extracted from [24]

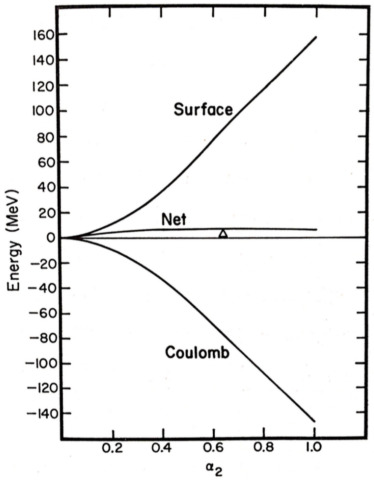

Figure 2.3: Correlation of the surface and Coulomb energy and the net deformation energy with the quadrupole deformation (a_2). - The Δ indicates the position of the saddle point of the nucleus. The figure is extracted from [25]

and corresponds to the saddle point of the nucleus. From this point, the decrease in the Coulomb energy begins to overwhelm the increase in the surface energy. As a consequence, the potential energy of the nucleus starts to decrease. Then the nucleus is not able to recover from the deformation and it will continue deforming and will finally fission. This maximum of the deformation energy is the fission barrier, indicating that fission may occur if the excitation energy of the nucleus is beyond this value.

The liquid drop model gives a theoretical interpretation for the fission process and provides a satisfactory order of magnitude of fission barrier. However it cannot explain some important fission properties such as the asymmetric fission and “magic numbers".

They can be explained by the Nuclear Shell Model which takes into account the quantum nature of the nucleus.

2.1.2 Nuclear shell model

2.1.2.1 Nuclear shell structure

The observation [26] of the enhanced stability of nuclei due to "magic numbers" of protons and neutrons pushed forward the development of the shell model of nucleus [27, 28]. In this model, nucleons are assumed to be independent, freely moving in a potential well generated by other nucleons and obeying the Schrödinger equation.

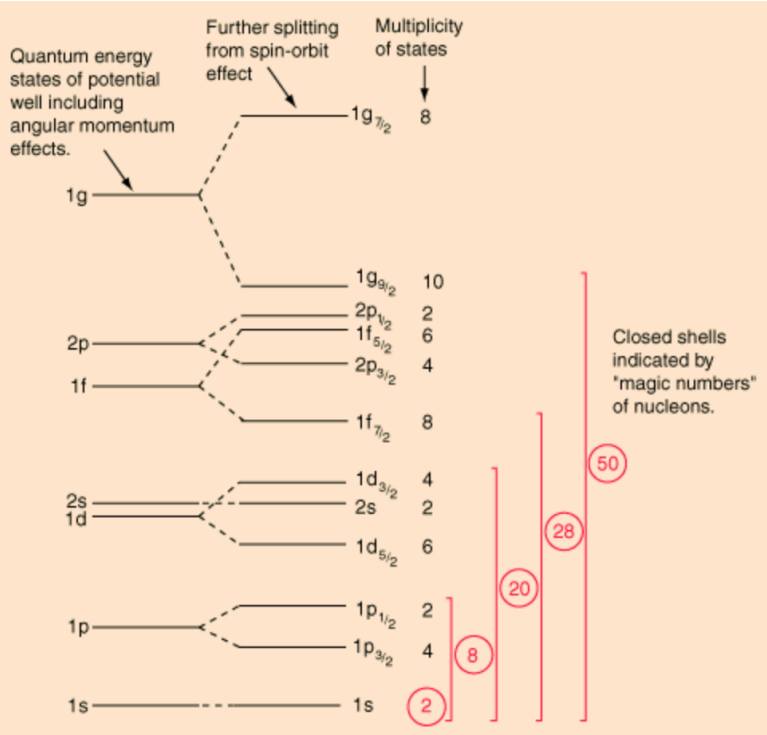

Figure 2.4: Nuclear energy levels - The figure is extracted from [29]

As figure 2.4 shows, the nuclear energy states are quantized in a way similar to the atomic case. The numbers and letters at the left side of energy level stand for the principal quantum number n and orbital angular momentum quantum number l where s, p, d, f, ... symbols are used for l=0, 1, 2, 3, ... like in the atomic case. However, l here is not limited to the n as in the atomic case. The energy levels are split by the spin-orbit coupling which cause the overlapping levels as shown in the figure 2.4. The

subscripts at right side indicate the value of the total angular momentum number j, and the multiplicity of the state (degeneracy) is $2j + 1$. 2, 8, 20, 28, 50 are the magic numbers where the nuclei are more stable due to the shells closure with a large energy gap.

2.1.2.2 Strutinsky's method

Nilsson extended the shell model to deformed nuclei [30]. He developed diagrams to show single-particle energy levels as a function of the nuclear deformation.

However, the calculation of the total energy and mass of the nucleus based purely on the shell model was not precise. Then Strutinsky applied shell correction into the liquid drop model to take advantage of both models which is named as the macroscopic (liquid drop model)-microscopic (shell effect) method. In this method, the total energy of the nucleus is taken as the liquid drop model energy E_{LDM} with the shell (δU) and pairing (δP) correction,

$$E = E_{LDM} + \delta U + \delta P \tag{2.8}$$

The shell correction, just like the liquid drop model energy, is a function of the nuclear deformation. It tends to lower the ground state masses of spherical nuclei with magic or near-magic numbers of nucleons. It also tends to lower the ground state mass of midshell nuclei at some finite deformation, thus accounting for deformed nature of the actinides.

The deformation energy calculated for a typical actinide nucleus with the Strutinsky's procedure is schematically illustrated in figure 2.5 through which we can tell the double-humped fission barrier. The energy is lowest at a deformation corresponding to the known ground state quadrupole moments of actinide nuclei. The second minimum is due to the strong negative shell correction and it corresponds to fission isomers. The second minimum persists for the actinide nuclei up to californium. For heavier nuclei the outer barrier disappears mainly because the liquid drop energy falls off more steeply at a smaller deformation. The dashed line is the potential energy purely calculated by liquid drop model without shell effect correction.

This hybrid macroscopic-microscopic approach overcame the main weakness of liquid drop model and nuclear shell model and gave a good description of the fission.

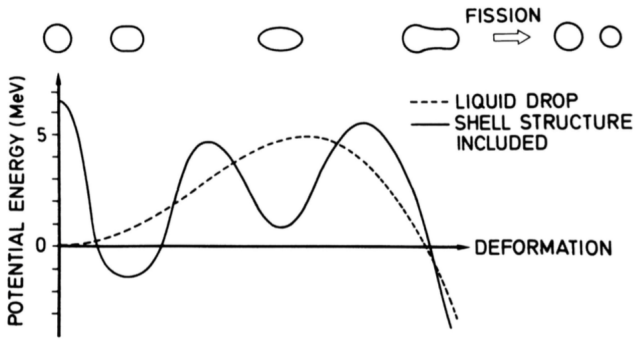

Figure 2.5: Schematic illustration of the fission barrier of a typical actinide nucleus - The figure is cited from [31]

2.1.3 Semi-empirical model GEF (GEneral Fission description)

The GEF model code has been developed in recent years by K. H. Schmidt et al [32] with the aim to provide dedicated nuclear data for application in nuclear technology and engineering. This model has a high degree of generality. Firstly, it treats spontaneous fission and fission up to an excitation energy of about 100 MeV for a wide range of heavy nuclei from polonium to seaborgium, secondly it calculates the majority of all possible fission quantities, thirdly, it is based on general properties of microscopic systems and general properties of a function in multidimensional space. More details about its theoretical ideas and physical models can be find in references [32, 33].

2.2 Fission Fragment Angular distribution (FFAD)

A theory about FFAD is presented here since we also measured FFAD of ^{237}Np in our experiment.

2.2.1 Description of the deformed rotating nucleus

The anisotropy of FFAD was observed for the first time in 1952 when studying the photonfission of ^{232}Th [34]. In later experiments, anisotropic angular distributions of fission fragments were also found in neutron-induced fission [34, 35].

R. Vandenbosch and J. R. Huizenga [25] developed a theory to describe the FFAD based on the model of axially symmetric transition states at the saddle point of the fissioning nucleus. As figure 2.6 shows, when a nucleus is deformed with an axial

symmetry (fission direction), its total angular momentum is $\vec{J}$. $\vec{M}$ is the projection of $\vec{J}$ on an arbitrary fixed axis, which is usually taken as the neutron beam direction in neutron-induced fission, $\vec{K}$ is the projection on the symmetric axis and $\vec{R}$ is the projection on any axis perpendicular to $\vec{K}$. $\vec{J}$ is conserved in the entire fission process because of the conservation of the total angular momentum.

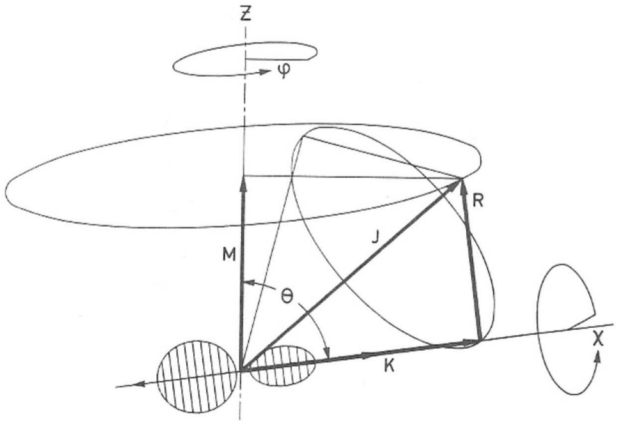

Figure 2.6: Angular momentum of fissioning nucleus - $\vec{J}$ is the total angular momentum of the deformed nucleus. $\vec{M}$, $\vec{K}$, $\vec{R}$ are, respectively, the projections of $\vec{J}$ on the space fixed axis z, on the symmetry axis of the fission and on an axis perpendicular to $\vec{K}$.

$\vec{K}$ is the projection of the angular momentum of the nucleons in the frame of the deformed nucleus which is also rotating like a rigid body with an angular momentum $\vec{R}$. Therefore

$$\vec{J} = \vec{K} + \vec{R} \tag{2.9}$$

In figure 2.6, θ is the angle between the nuclear symmetry axis and the space fixed axis, ϕ is the azimuthal angle around it, χ is the azimuthal angle around the symmetry axis. The angular wave function Ψ of the rotating deformed nucleus obeys the equation 2.10 [36]:

$$\frac{\hbar^2}{2J_\perp}\left[\frac{1}{sin\theta}\frac{\partial}{\partial\theta}(sin\theta\frac{\partial\Psi}{\partial\theta}) + \frac{(cos\theta\frac{\partial}{\partial\chi} - \frac{\partial}{\partial\phi})^2\Psi}{sin^2\theta}\right] + \frac{\hbar^2}{2J_\parallel}\frac{\partial^2\Psi}{\partial\chi^2} + E\Psi = 0 \tag{2.10}$$

where $J_\parallel$ is the moment of inertia of the rotation around the symmetry axis, $J_\perp$ is the moment of inertia around an axis perpendicular to it.

The solution of the equation is:

$$\Psi = \sqrt{\frac{2J+1}{8\pi^2}} \cdot e^{iM\phi} \cdot e^{iK\chi} \cdot d^J_{M,K}(\theta) \tag{2.11}$$

where $d^J_{M,K}(\theta)$ is the rotation matrix, independent of ϕ and χ and introduced by Wigner [37]:

$$d^J_{M,K}(\theta) = \sqrt{(J+M)!(J-M)!(J+K)!(J-K)!}\times \sum_n (-1)^n \frac{[sin(\theta/2)]^{M-K+2n}[cos(\theta/2)]^{2J+K-M-2n}}{(J-M-n)!(J+K-n)!(M-K+n)!n!} \tag{2.12}$$

Therefore the angular distribution for the fission fragments $W^J_{M,K}(\theta)$ at angle θ is

$$W^J_{M,K}(\theta) = \frac{2J+1}{2} \mid d^J_{M,K}(\theta) \mid^2 \tag{2.13}$$

and the rotational energy levels of the fissioning system is:

$$E_{rot} = \frac{\hbar^2}{2J_\perp}[J(J+1) - K^2] + \frac{\hbar}{2J_\parallel}K^2 \tag{2.14}$$

2.2.2 Angular distribution in neutron-induced fission

As has been mentioned, the fission direction is the symmetry axis and the FFAD is given by equation 2.13. Here we assume that the projection of $\vec{J}$ on symmetry axis, $\vec{K}$, remains constant along the fission process from the saddle point, where the fission is decided, to the scission point when the fragments are separated. This hypothesis is true if the nucleons stay on their individual orbits along the fission, since $\vec{K}$ is the projection of the angular momentum of the nucleons in the frame of the deformed nucleus.

In the case of neutron-induced fission, we need to take into account both the neutron's spin $\vec{s}$ (1/2) and the target's spin $\vec{I_0}$. Hence the channel spin (total spin of the compound nucleus) is:

$$\vec{S} = \vec{I_0} + \vec{s} \tag{2.15}$$

and the total angular momentum $\vec{J}$ of the compound nucleus is given by the sum of $\vec{S}$ and its orbital angular momentum $\vec{L}$:

$$\vec{J} = \vec{S} + \vec{L} \tag{2.16}$$

2.2.2.1 Case of even-even targets

The spin of even-event targets, for example ^{238}U, is equal to 0 ($\vec{I_0} = 0$). According to equation 2.15 and 2.16, the relations of the corresponding quantum numbers are :

$$\begin{aligned} S &= s = 1/2 \\ J &= l \pm 1/2 \\ M &= \pm 1/2 \end{aligned} \tag{2.17}$$

From equation 2.13, we can obtain the FFAD for a given J and K by:

$$W^J_{\pm 1/2,K}(\theta) = \frac{2J+1}{4}(\mid d^J_{1/2,K}(\theta) \mid^2 + \mid d^J_{-1/2,K}(\theta) \mid^2) \tag{2.18}$$

Figure 2.7 shows the FFAD calculated by equation 2.18 for even-even target with different couples of (K, J), from which we can deduce following arguments.

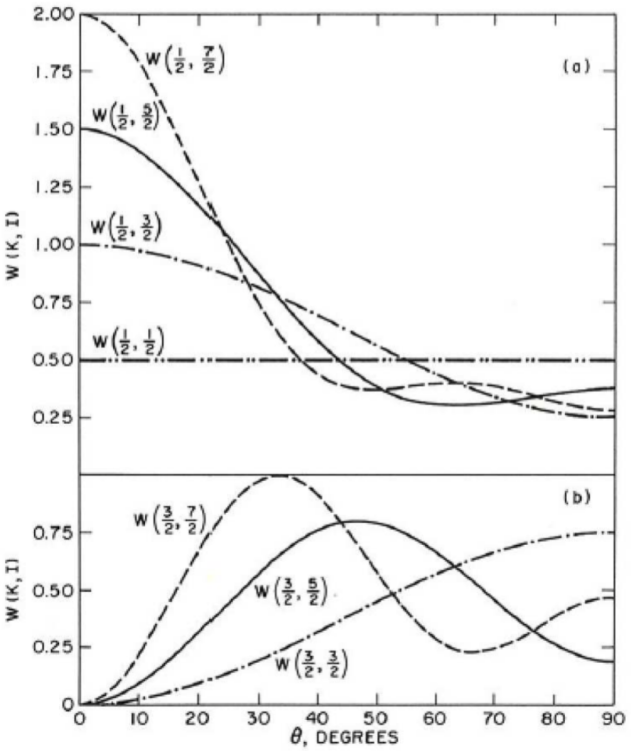

Figure 2.7: Theoretical FFAD calculated by equation 2.18 for even-even target.
- The figure is cited from [25]

- If only s-waves ($l = 0$) are involved, $J = K = \frac{1}{2}$, the FFAD is flat because $\vec{J}$ is fully de-oriented and the probability of the different emission angle is the same. The theoretical FFAD curve is shown in figure 2.7 labeled with $W(\frac{1}{2}, \frac{1}{2})$.

- When $K \ll J$, the emission is forward-backforward peaked. In this case, the direction of $\vec{J}$ is very close to l which is orthogonal to the beam axis, which means fragments are emitted orthogonally to $\vec{J}$. Beam axis is the only direction that all the contributions from all directions of $\vec{J}$ add up, therefore the angular

distribution, as the curves with $W(\frac{1}{2},\frac{7}{2})$ and $W(\frac{1}{2},\frac{5}{2})$ in figure 2.7, is peaked at 0 degree.

- When $K \approx J$, the fission axis is along $\vec{J}$. As $\vec{J}$ is orthogonal to the beam axis, so is the fission direction and the FFAD is sideward peaked as the curve of $W(\frac{3}{2},\frac{3}{2})$ in figure 2.7.

2.2.2.2 Case of even-odd targets

The spins of the even-odd targets, such as ^{235}U and ^{237}Np, are not 0: $I_0^\pi = \frac{7}{2}^-$ for ^{235}U, $I_0^\pi = \frac{5}{2}^+$ for ^{237}Np. The corresponding channel spin is $S = 3$ or $S = 4$ for ^{235}U, $S = 2$ or $S = 3$ for ^{237}Np. Since the channel spin is unpolarized here and larger than the case of even-even targets, $\vec{S}$ contributes significantly to the de-orientation of the $\vec{J}$.

An even-odd target becomes a compound even-even target after capturing a neutron. Due to the pairing effect, the neutron binding energy is larger. As a consequence, the excitation energy of the compound nucleus is much larger than the fission barrier for the even-even target. At high excitation energy the distribution of K becomes statistical and the probability is proportional to the number of intrinsic single particle states contributing to this K at the saddle point. So statistical method is needed to describe the states.

The distribution of K probability has a Gaussian form like:

$$\rho(K) \propto exp(-\frac{K^2}{2K_0^2}), K \leq J \tag{2.19}$$

where $K_0^2 = \frac{J_{eff}T}{\hbar^2}$, J_{eff} and T are, respectively, the effective moment of inertia and the thermodynamic temperature of the fissioning nucleus. J_{eff} can be calculated by:

$$J_{eff} = \frac{J_\perp J_\parallel}{J_\perp - J_\parallel} \tag{2.20}$$

where $J_\perp$ and $J_\parallel$ are respectively the parallel and perpendicular moment of inertia as have been introduced in section 2.2.1.

From equation 2.19 we can see that K distribution extends to higher values when the temperature is increasing or the mass is increasing which can cause the increase of the moment of inertia. At high incident energy l increases more rapidly than K_0 so that K is generally lower than J. According to the above discussion, the FFAD is often forward-backward peaked.

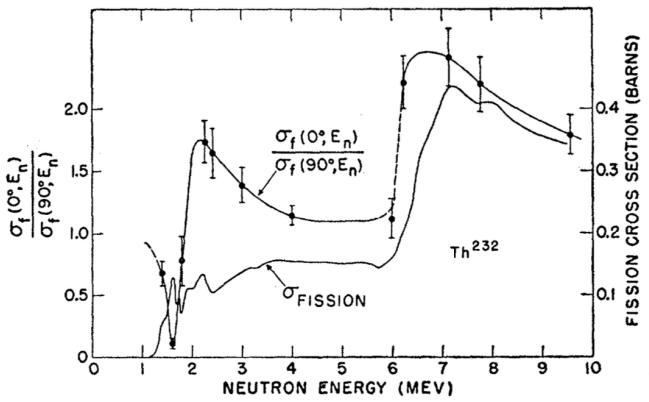

Figure 2.8: Comparison of total fission cross section and relative differential fission cross sections (anisotropy parameter) for ^{232}Th - The multiple-chance fission structure is visible both in cross section and FFAD. The figure is cited from [35]

Anisotropy also shows a multiple chance structure similar to the fission cross section as shown in figure 2.8. A structure occurs at an excitation energy where second-chance (n, nf), third-chance (n, 2nf), ..., become energetically possible. When a new fission chance is open, the total angular momentum J is slightly affected whereas K_0 drops significantly due to the drastic decrease of the temperature due to the emission of the neutron. Therefore anisotropy is enhanced.

Chapter 3

n_TOF facility at CERN

The experiments in this thesis work have been performed at the n_TOF facility at CERN. In this chapter, we will briefly present the structure of n_TOF facility and its features for measuring nuclear data.

The idea of n_TOF was proposed by C. Rubbia et al [38] in 1998. It is based on a spallation neutron source by impinging 20 GeV/c protons to a thick lead target which can provide neutrons from thermal energy up to GeV. The proton beam has a typical intensity of 7×10^{12}/pulse and a cycle of 1.2 s or a multiple of it, yielding about 300 neutrons per single incident proton. The layout of n_TOF facility is shown in figure 3.1.

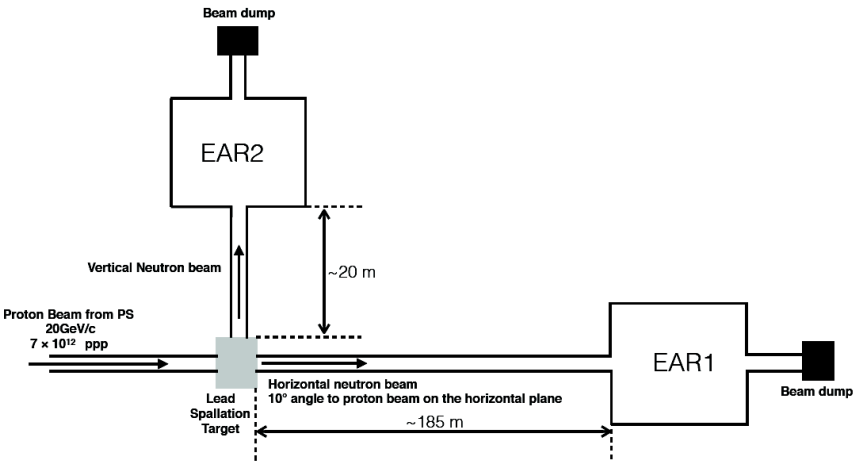

Figure 3.1: Layout of the of n_TOF facility.

There are currently two neutron beam lines running in parallel and sending neutrons to two different experimental area where samples are mounted and neutron-induced

reactions are studied. The first one is horizontal and has a length of 185 m. It sends neutrons to the experimental area 1 (EAR-1) which is operational since 2001. The second beam line is vertical and sends neutrons to experimental area 2 (EAR-2). It has been running since 2014, performing as a complementary to EAR-1 for its high neutron flux due to 20 m flight path.

3.1 Proton beam

The 20 GeV/c proton beam is from CERN's Proton Synchrotron (PS) accelerator, which is capable of accelerating $\approx 3 \times 10^{13}$ protons per cycle. This extraordinarily prolific beam is concentrated in a very short pulse to serve a tremendous precise time-of-flight (TOF) determination for neutron energy. The proton beam line allows to vary the beam spot size at the lead target level[39].

The proton beam can be delivered on spallation target in two different operational modes: dedicated (primary) mode and parasitic mode. In primary mode a typical 7×10^{12} protons bunch with 20 GeV/c momentum is sent to the target with a 1.2 s PS cycle fully dedicated to n_TOF . The bunch time distribution has a Gaussian shape with 7 ns RMS. In parasitic mode, $\sim 3.5 \times 10^{12}$ protons bunch is extracted from PS and sent to n_TOF . The pulse shape and beam profile at the spallation target are almost the same as the one in dedicated mode.

The number of protons per pulse is determined pulse by pulse by using a Beam Current Transformer (BCT) located in proton beam about 6 m upstream from spallation target. A resistive Wall Current Monitor (WCM) is mounted immediately after the BCT which provides a signal proportional to the proton beam current and could be used either for timing reference or to monitor directly the proton beam intensity[40].

3.2 Spallation target

The spallation target, figure 3.2, is a cylindrical lead block of 60 cm in diameter and 40 cm in length with a high purity of 99.99%. It is surrounded by a 1 cm layer of demineralized water dedicated for cooling and in the forward direction is attached an additional 5 cm moderator layer filled with ^{10}B-loaded water. The water in the moderator layer can moderate the initially fast neutrons into the desired energy spectrum,

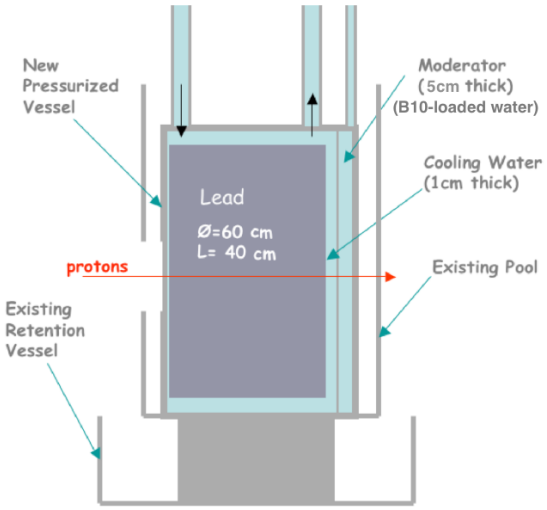

Figure 3.2: Schematic of n_TOF spallation target.

which ranges down to thermal energies. ^{10}B is used for absorbing the 2.23 MeV γ rays emitted from the neutron capture in water to reduce the background.

3.3 Neutrons beam lines

3.3.1 Horizontal beam line to EAR-1

The neutrons emitted from the spallation target are traveling in a vacuum tube kept at 10^{-2} mbar to avoid the scattering by nitrogen and oxygen in the air. The angle on the horizontal plane between the proton beam axis and neutron beam is 10° in order to minimize the collection of unwanted secondary particles in the EAR-1. A sweeping magnet at a distance of ∼150 m is used to remove all the remaining charged particles. Neutrons fly toward to EAR-1 at ∼185 m downstream from the target through two collimators as shown in figure 3.3.

The first collimator located at ∼135 m has a 11 cm aperture in diameter and consists of iron and concrete with a total thickness of 2 m. The second collimator close to experimental area located at ∼175 m defines the beam spot which is changeable. For the neutron capture measurement a collimator with a small aperture, 1.9 cm in diameter, is used to reduce the neutron halo around beam. In the case of neutron-induced fission measurement, when samples with large size are used, we can enlarge the collimator

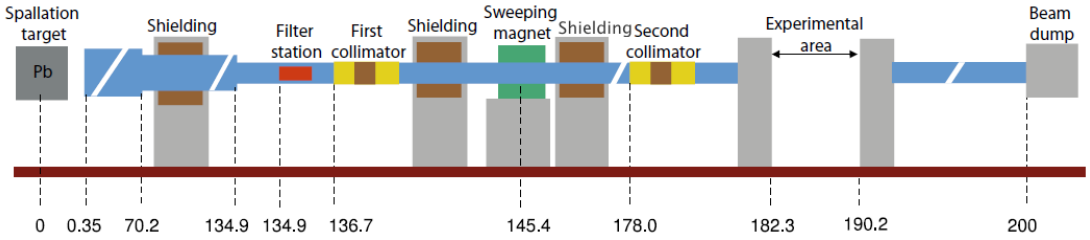

Figure 3.3: Layout of the n_TOF horizontal neutron beam line to EAR-1 from the spallation target to the beam dump (distances are given in meters).

aperture to 8 cm in diameter.

Several shielding walls have been installed in order to intercept particles traveling out of the neutron pipe. Shielding at ∼140 m is separating the primary area from the secondary area. It's a concrete wall with 2.4 m in length partially equipped with iron around the tube. A muon shielding completely made with iron is at ∼150 m, a few meters right after the sweeping magnet. Two shieldings made of concrete at the entrance (at ∼180 m) and exit (at ∼190 m) of the experimental area are installed to minimize the neutron and γ background.

Filter station can hold some filters inserted in the beam line to measure the background in the resonance region. Filters are typically made of thick materials having strong resonances: neutrons having an energy corresponding to the resonance are totally absorbed by filters so that those which are still seen at this energy come from a background or from neutrons outside the expected time-energy dependence. Silver, tungsten, cobalt, molybdenum and aluminum filters have been used as filters at n_TOF for neutron energies at 5.1, 18.8, 45, 132, 3.5×10^4 and 8.7×10^4 eV respectively.

After the shielding at the exit of the experimental area, the neutron escape line, a tube with a ϕ=400 mm in diameter and ∼8 m in length ending at 200 m from the spallation target, is used to avoid neutron back-scattering in the experimental area. After that, neutrons reach the beam dump composed of borated paraffin.

Thanks to the above very efficient collimating and shielding system, the background at EAR-1 of n_TOF is very low.

3.3.2 Vertical beam line to EAR-2

The beam line to EAR-2 stands vertically above the spallation target and is $\sim$ 20 m long as shown in figure 3.4.

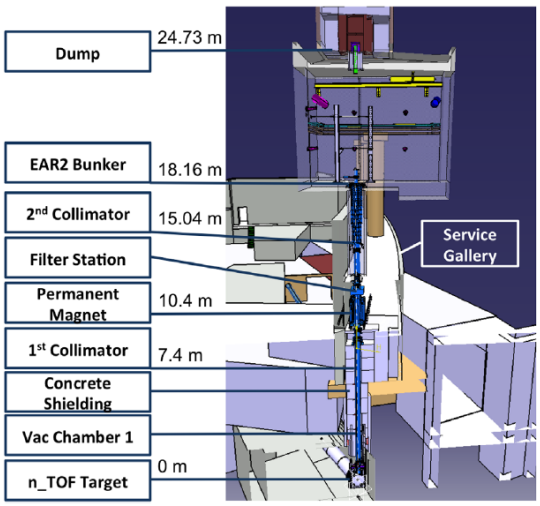

Figure 3.4: Layout of the n_TOF vertical neutron beam line to EAR-2 from the spallation target to the beam dump.

The first collimator is installed at 7.4 m above the target inside the first vacuum tube of the beam line. It consists of a iron cylinder of 1 m in length and 20 cm in inner diameter. The second one locating at 15.04 m above the target is composed by 2 m iron and 1 m borated polyethylene (B-PE) where the last 0.4 m have a core of boron-carbide cylinder. Several shielding blocks along the path are at the bottom, middle part of the beam line and entrance of the experimental area respectively.

The beam dump installed on the roof of the experimental hall consists of three layers to fully absorb the neutron beam. The core of the dump is a block of B-PE to slow down and capture neutrons from the beam and back-scattered neutrons from the consecutive beam dump layers as well. This core part is a block of $400 \times 400 \times 400\ mm^3$ with a hole, 250 mm in height and 340 mm in diameter, where the last vacuum tube of the beam line is inserted. The B-PE is surrounded by iron blocks to absorb the fast neutrons and photons in the beam with outer dimensions of $1600 \times 1600 \times 1600\ mm^3$. The beam dump is finally shielded by concrete with outer dimensions of $3200 \times 3200 \times 2400\ mm^3$ [41].

A permanent dipole magnet is installed at 10.4 m above the spallation target to deflect out all the charged particles originated in the spallation process in the lead target. The magnetic field in the center of the magnet is 0.253 T, over the total dipole length of 1.134 m. The integrated field is 0.287 Tm.

A neutron filter station is placed at 11.4 m above the spallation target. Filters can be used are molybdenum, tungsten, cobalt, silver, aluminum, lead, bismuth and cadmium with a thickness from less than 1 to tens of millimeters to blank out different neutron energies from the beam or to attenuate the in-beam photons.

3.4 Neutron flux

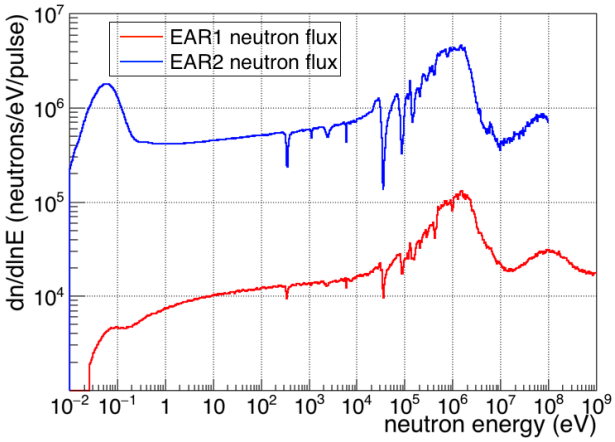

Figure 3.5: Neutron fluxes of EAR-1 and EAR-2. - The number of neutrons per equidistant logarithmic energy bin (dn/dlnE) per 7×12 protons integrated over a radius of r= 0.87 cm for EAR-1 and r=2.5 cm for EAR2.

The fluxes of n_TOF are measured by a series of experiments in different energy regions. The flux of EAR-1 is characterized by three different reactions and four different detection systems: a silicon monitor (SiMon) with ^{6}Li(n, α) reaction, a Micromegas detector (MGAS) with ^{10}B(n, α) and ^{235}U(n, f) reactions, a calibrated fission chamber from Physikalisch Technische Bundesanstalt (PTB) with ^{235}U(n, f) reaction, a PPAC chamber with ^{235}U(n, f) reaction. The flux of EAR-2 is characterized by the same reactions and similar detection systems (PTB was not used) as EAR-1. More details about the flux measurement can be found in references [42, 43].

The measured neutron fluxes of EAR-1 [42] and EAR-2 [43] are shown in figure 3.5. The shapes the EAR-1 and EAR-2 fluxes are similar. The high energy neutrons above 10 MeV are from the high energy processes of spallation. The strong peak around 1 MeV is the evaporation of neutrons from spallation process. The falling tail from 1 MeV to tens of keV is due to the moderation in the lead target. The flat part less than ∼10 keV is caused by the moderation in the water surrounding the target. The strong absorption at thermal neutron peak in EAR-1 caused by the ^{10}B-loaded moderator on the target only attached to the forward direction to EAR-1 (see in figure 3.2). The several deeps between 100 eV and hundreds of keV are caused by the absorption of aluminium, manganese and oxygen in the beam.

The flux of EAR-2 is higher than EAR-1 with a factor of about 40 due to its shorter flight path and larger solid angle. This much higher flux makes it possible to measure targets of low mass and/or for reactions with low cross section in a reasonable time. However this higher flux comes with the price of lower energy resolution compared with EAR-1 since the time-of-flight (TOF) is shorter.

3.5 Time-energy correlation

Neutron kinetic energy can be calculated in relativistic framework as:

$$E_n = (\gamma - 1)m_n c^2 \tag{3.1}$$

with:

$$\gamma = \frac{1}{\sqrt{1-\beta^2}} \tag{3.2}$$

$$\beta = \frac{v}{c} \tag{3.3}$$

where m_n is the neutron rest mass, c is the speed of light, v is the neutron velocity. So the incident neutron energy can be obtained directly from its velocity which is calculated as:

$$v = \frac{L_{geom}}{TOF} \tag{3.4}$$

in equation 3.4, L_{geom} is the geometric fixed flight length from the outer surface of the moderation layer around the spallation target to the experimental area where the neutron-induced reaction happens. TOF is the neutron time of flight of this path.

When neutrons are generated in the spallation target, to begin with, they are slowed down in the lead target and further moderated in the cooling and moderation layer, then they fly through the geometric flight path L_{geom} with a constant velocity. The experimental measured time of flight T is the difference between the detection of a neutron-induced reaction and the generation of neutrons, which is a sum of the moderation time T_{mod} and TOF.

$$T = T_{mod} + TOF \tag{3.5}$$

so the neutron velocity is

$$v = \frac{L_{geom}}{T}\frac{T}{TOF} = \frac{L_{geom}}{T}\frac{TOF + T_{mod}}{TOF} = \frac{L_{geom}}{T}(1 + \frac{T_{mod}}{TOF}) = \frac{L_{geom} + vT_{mod}}{T} \tag{3.6}$$

vT_{mod} can be defined as an equivalent moderation length λ which can be obtained by simulation, so the velocity can be written as

$$v = \frac{L_{geom} + \lambda}{T} \tag{3.7}$$

where $L_{geom} + \lambda$ can be regarded as an effective flight path L.

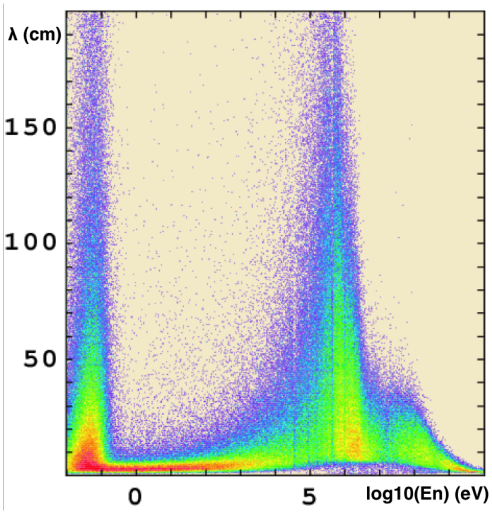

Figure 3.6: Distribution of moderation distance λ for EAR-1 as a function of neutron energy.

λ is a stochastic quantity with a probability density distribution depending on the neutron energy or time-of-flight.The distribution of λ as a function of the neutron energy at EAR-1 and as a function of neutron time-of-flight at EAR-2 simulated by FLUKA are

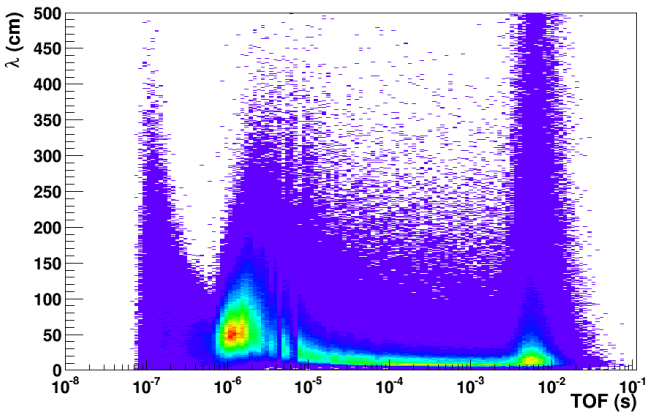

Figure 3.7: Distribution of moderation distance λ for EAR-2 as a function of neutron TOF.

respectively shown in figure 3.6 and figure 3.7. The deeps around 100 keV in figure 3.6, and the ones below 10^{-5} s in figure 3.7 are due to the absorption as mentioned in neutron flux section (section 3.4).

In the subsequent data analysis, we will use the well-known resonances of $^{235}U(n, f)$ at low energy to determine a effective L which includes a most probable value of λ at this resonance energy. Then based on the λ distribution shown in figure 3.6 and 3.7 (we use the most probable λ at each given energy), we can deduce the effective L at different energy. This approach will be discussed in section 5.4.1.

3.6 Energy resolution

According to equation 3.1, 3.2 and 3.3, we have

$$\frac{dE}{E} = \frac{d\gamma}{\gamma - 1} = \gamma(\gamma + 1)\frac{d\beta}{\beta} = \gamma(\gamma + 1)\frac{dv}{v} \tag{3.8}$$

from which it can be seen that energy resolution is directly related to the velocity resolution. Therefore the energy resolution is

$$\frac{\Delta E}{E} = \gamma(\gamma + 1)\sqrt{(\frac{\Delta L}{L})^2 + (\frac{\Delta T}{T})^2} \tag{3.9}$$

where Δ stands for the standard-deviation. ΔL is from the fluctuation of the moderation distance $\Delta\lambda$ from the simulation, ΔT is due to the width of proton bunch which is of order of 7 ns. Apparently the longer the flight path, the better the resolution.

E_n	$\Delta E_n/E_n$	
(eV)	EAR-1	EAR-2
1	3.2×10^{-4}	4.8×10^{-3}
10	3.2×10^{-4}	5.7×10^{-3}
10^2	4.3×10^{-4}	8.1×10^{-3}
10^3	5.4×10^{-4}	1.4×10^{-2}
10^4	1.1×10^{-3}	2.3×10^{-2}
10^5	2.9×10^{-3}	4.6×10^{-2}
10^6	5.3×10^{-3}	5.6×10^{-2}

Table 3.1: The energy resolution as function of neutron energy for EAR-1 and EAR-2

At high energy ΔT dominates the energy resolution and at low energy ΔL is dominant. The simulated energy resolution as function of neutron energy in EAR-1 [44] and EAR-2 [45] are shown in table 3.1, through which it can be seen that the energy resolution in EAR-2 is limited compared with EAR-1.

Chapter 4

Experimental setup at n_TOF

In this PhD work, two experiments have been done at n_TOF facility at CERN, one in each of the experimental areas. Their setups will be discussed in this chapter. In the last section, other detection systems at n_TOF that are not used in our experiments will be briefly introduced.

4.1 Parallel Plate Avalanche Counter

The high energy neutrons generated at n_TOF , up to GeV, make it possible to study neutron-induced fission in spallation region. In this domain, on one hand, other reaction channels are opened to compete with fission; on the other hand, the instantaneous counting rate is very high. These constraints lead us to select fission event by the detection of two fission fragments in coincidence and to use PPAC due to its excellent time resolution.

4.1.1 Principle of the fission detection by PPAC

The principle of the fission event detection by PPACs is sketched in figure 4.1. A target (yellow circle) is closely surrounded by two PPACs to detect two fission fragments, fission fragment 1 (FF1) and fission fragment 2 (FF2) in figure 4.1, in coincidence to identify the fission event. Most of the background other than fission event could be rejected by this coincidence method. Since PPAC is position sensitive, the fission angle θ and azimuth angle ϕ could be measured as well.

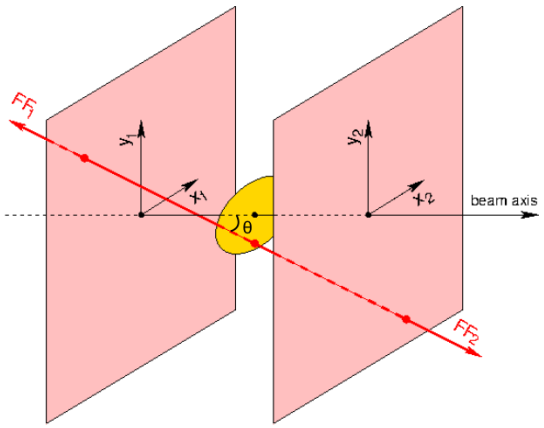

Figure 4.1: Principle of fission event detection and fission angle measurement with 2 PPACs

Concerning the detection method and n_TOF facility characteristics, the detection system is designed as following to fit them well:

1) detector is close to target to cover a large solid angle.

2) target and its backing are very thin so that more fission fragments can go through and come out from it.

3) target size is large to suit the large beam spot size and accumulate as much statistics as possible.

When two fission fragments are localized on the detectors, as figure 4.1 shows, the emitting point on the target can be reconstructed out based on the assumption that two fission fragments are emitted in a back to back direction in laboratory system. This is true for the fission induced by the low energy neutrons because the momentum transferred to the fission nucleus is very small. However it's not the case for high energy neutrons where large momentum is transferred which can distort the back to back emission of the fission fragments.

A simulation based on 1 GeV neutrons and ^{235}U target is done to evaluate this effect. Figure 4.2a is the simulation setup simplifying the target to a point at the center between two PPACs. Asymmetric fission is considered in the simulation. The blue trajectories are the back to back emission of fission fragments in the center of mass frame which is slightly distorted by a momentum transfer P_n in the laboratory frame. So the real track are the red ones and the emission angle changes to θ_m from θ_{cm}. The momentum transfer for 1 GeV incident neutron is 331 MeV/c [46].

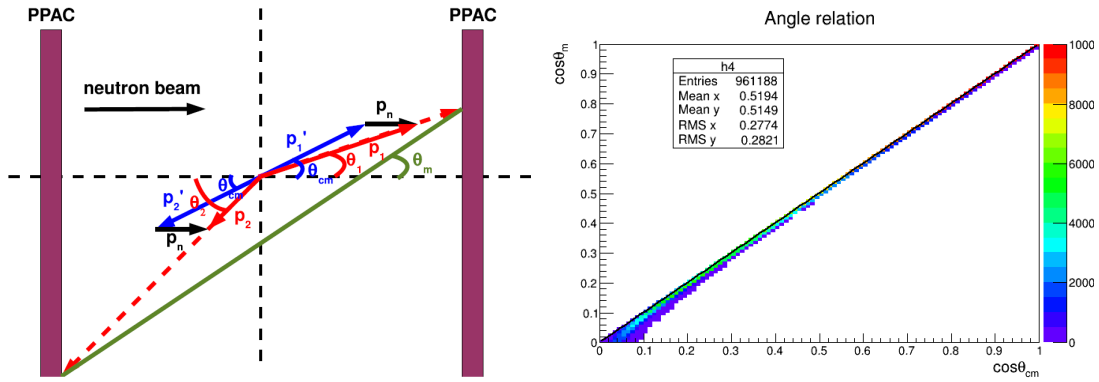

(a) (b)

Figure 4.2: Simulation on the effect of momentum transfer from high energy neutrons on the emission angle of fission fragments. - (a): simulation setup, (b): Relation between the measured angle cosθ_m and the emission angle in center of mass frame cosθ_{cm} as given by the simulation for a momentum transfer of 331 MeV/c from 1 GeV incident neutrons

According to the simulation result, 4.2b, most of the events are concentrated on the diagonal of cosθ_m = cosθ_{cm}, some differences are present only at large emission angles about cosθ_{cm} less than 0.3. However, in the real case these large emission angles can not be detected due to the detection efficiency which will be described in latter chapter, so the emission of fission fragments could be treated as back to back in our case.

4.1.2 PPAC description

Each PPAC consists of a central anode for timing measurement and two cathodes with 2 mm separated strips for position measurement in two orthogonal dimensions. PPAC has a square active surface of 200×200 mm^2, and the overall assembled dimensions of a PPAC is a square of 305 mm × 305 mm with 13 mm in thickness. A global scheme of a PPAC is shown in figure 4.3.

Electrodes are made of 1.7 μm thick mylar on which an aluminium or gold layer is deposited to make it conductive. The deposition is done by evaporating the melted aluminium or gold under vacuum so that atoms travel straightly and deposit uniformly on the mylar foil. For the anode an uniform layer of 30 nm is deposited on both sides of the mylar foil since it's the central electrode facing gaps on each side. Cathode is coated with an layer of 60 nm only on the side facing the gap. It is divided into 2 mm

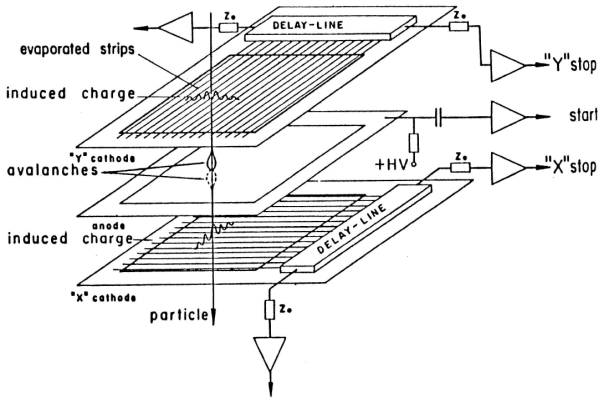

Figure 4.3: Principles of bidimensional, induced charge, read-out from parallel plate avlanche counters. - The figure is extracted from [47].

wide strips for localization of the detected particles. This is obtained by depositing the aluminium or gold with a mask of parallel wires of 0.1 mm in diameter in every 2 mm. Electrodes are glued on epoxy resin frames coated with a thin copper layer for shielding against electromagnetic noise and gold layer to prevent oxidation. Circuitries for signal extraction are drawn on the epoxy frame, preamplifiers and delay lines are plugged directly on it as well. Pictures of electrodes are shown in figure 4.4.

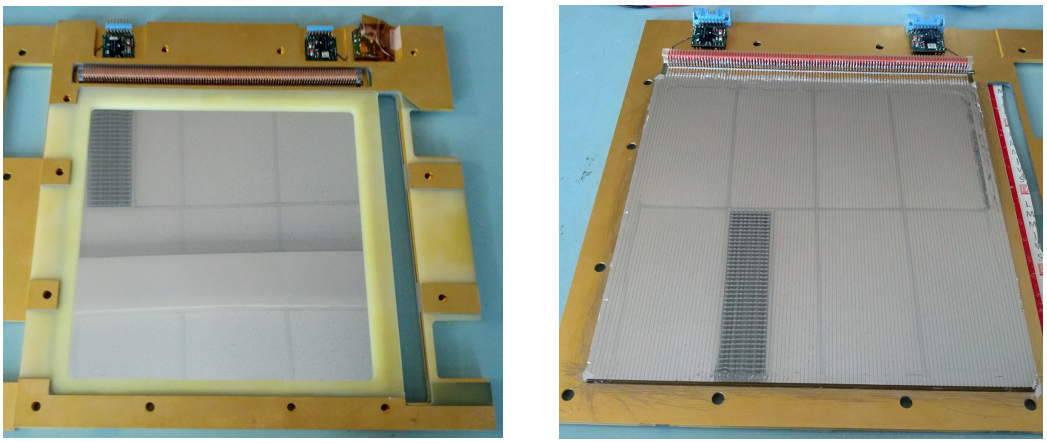

(a) Anode frame **(b)** Cathode frame

Figure 4.4: PPAC electrodes

The distance between electrodes is 3.2 mm since the gap between them must be limited to a few millimeter to keep a high electric field, which is typically around 550 V

over 3.2 mm. This high electric filed combined with a low gas pressure at about 4 mbar create a condition of proportional regime and a good time resolution.

The filling gas is C_3F_8 (octafluoropropane) at a pressure of 4 mbar. It is preferred to isobutane which is used more generally because octafluoropropane gives more stable working conditions and overall for safety reasons since it is not flammable. A gas flow is mandatory to evacuate degassed molecules absorbed in the electrodes to keep a stable pressure. In this regulation a sensor measuring the pressure is connected to an automaton which gives orders to control valves insuring the constant pressure with 1% precision. A monitor program allows to control the regulation remotely at the n_TOF control room.

4.1.3 PPAC signal readout

When a charged particle is going through the gap, the gas is ionized and primary electron-ion pairs are generated along the trajectory. The electrons and positive ions drift towards the anode and cathode respectively. During this drift, electrons create an avalanche to the anode plane. Electrons drift so fast that their collection time is only around several nanoseconds. This anode signal is fed to a current preamplifier and finally output a signal with typical full width of 20 ns and rise time of 5 ns whose typical time resolution is 0.3 ns. This fast and high resolution anode signal helps avoiding pile-up when the counting rate is high. In the meanwhile, negative charges induce positive charges in the cathode with the position centered on the avalanche position, thanks to the strips and delay line the accurate position can be obtained.

The delay line as shown in figure 4.5 built at Institut Physique Nucléaire d'Orsay (IPNO) is a plastic rod of 7 mm in diameter holding a cell of 1.4 mm in length in every 2 mm. Each strip on the cathode is connected to a delay line cell where there is a coil composed by 6 windings copper wire of 0.3 mm in diameter. A capacitor of 6.8 pF joints adjacent strips and a 10 pF capacitor connects each strip to ground. With such a setup, the delay line has a typical impedance of about 300 Ω and its propagation velocity for signals is about 3.2 ns/strip. These delay lines have a better rise time and less amplitude attenuation than commercial ones. Both ends of one delay line are connected to a charge preamplifier which is matching its resistive impedance to minimize the reflection. When a signal is delivered out from a strip, it is split into two and transmitted oppositely to the ends of the delay line. The time for a signal to

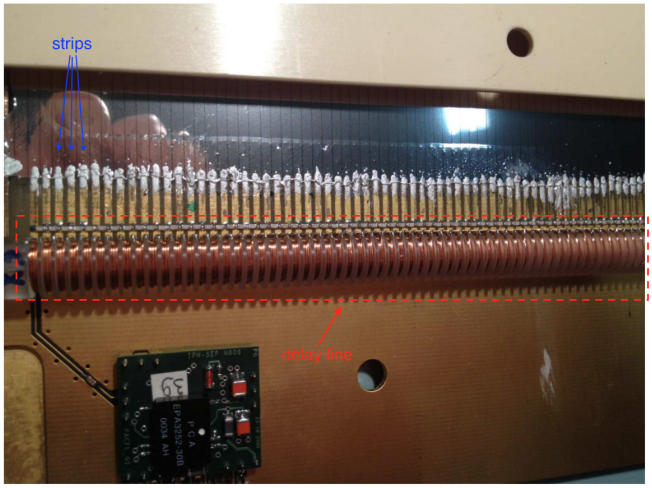

Figure 4.5: Picture of delay line plugged on a cathode frame

reach one end of the delay line is proportional to the travel distance. Therefore, the time difference between two signals of a delay line delivers a position information on the corresponding cathode. The two cathodes of each PPAC provide orthogonal positions, so that the position of the particles can be determined.

4.2 Isotopes targets

A good compromise between a small energy loss of fission fragments in a thin target for good detection efficiency and a reasonable statistical counting rate can be obtained with a target thickness from tens to hundreds of $\mu g/cm^2$. All the targets were made by electrodeposition of hydroxides in an organic solvent made conductive by adding some nitric acid. The deposition was done on a very thin aluminium backing (a few micrometers in thickness) placed as cathode in an electrolytic cell. The dimension of the target deposit is a circle of 8 cm in diameter. The yield of electrolysis was found to be better than 90% from the measured amount of deposit.

^{237}Np target material was from IPNO, ^{235}U and ^{238}U material were from CSNSM Orsay. All of the targets were made at IPNO. Some of them are shown in figure 4.6.

The purity of isotope targets is important to know. The purity of ^{235}U targets was measured by mass spectrometry with following results: 92.71% of ^{235}U, 6.28% of ^{238}U, 0.74% of ^{234}U and 0.27% of ^{236}U. The ^{238}U targets have a high purity since they are

prepared from natural uranium by a mass separator with a factor of separation better than 10,000.

The total mass of targets were measured by α-counting with a silicon detector in a well defined geometrical system. The solid angle of the silicon detector to the target was determined precisely with less than 1% uncertainty. The time duration of the measurement was determined by taking more than 10,000 counts in the silicon detector for the target isotopes. Consequently, the uncertainty of the target mass is lower than 1%.

(a) ^{237}Np target **(b)** ^{238}U target

Figure 4.6: Actinides targets.

4.3 PPAC experimental setup

A minimal measuring system consists of one target and two surrounding PPACs as sketch in figure 4.1 representing a basic cell. However a simultaneous measurement of several targets is highly desirable to optimize the use of the beam and accumulate more statistics which can be realized by adding more such cells along the beam. In this case neutrons travel across several detectors and targets, but the neutron flux attenuation due to the neutron scattering is still very low because the materials in the beam are very thin. For example, the neutron flux loss is less than 1% even at the top of the strong resonances. This kind of multiple target and detector setup can possibly show multiple coincidences, for example one fission fragment crosses two PPACs along its trajectory, which constrain us to identify the fissioning target. It can be easily done based on the time-of-flight of the fission fragment thanks to the fast timing of anode.

We did one experiment at each experimental area. First one is the beam measurement of the EAR-2, second one is the measurement of the ^{237}Np(n, f) cross section and fission fragment angular distribution at EAR-1. Their setups are described in following sections.

4.3.1 PPACmon setup at EAR-2

A PPAC monitor chamber, which is called PPACmon, was designed and constructed by IPNO, jointly with the University of Santiago de Compostela (Spain) and CERN for monitoring the EAR-2 neutron beam. Its experimental setup is shown in figure 4.7a. Neutrons coming from the underneath tube traverse the chamber and enter the above escape line which is connected to the dump at the end. There is a kapton foil with a thickness of 80 μm at both entrance and exit of the chamber. Inside chamber (5.4), there are 3 PPACs and 2 ^{235}U targets with 0.7 μm thick aluminium backings perpendicular to neutron beam. Detectors are centered on the beam axis. The distance between each anode to target is 17.1 mm. The results of this experiment is shown in chapter 5.

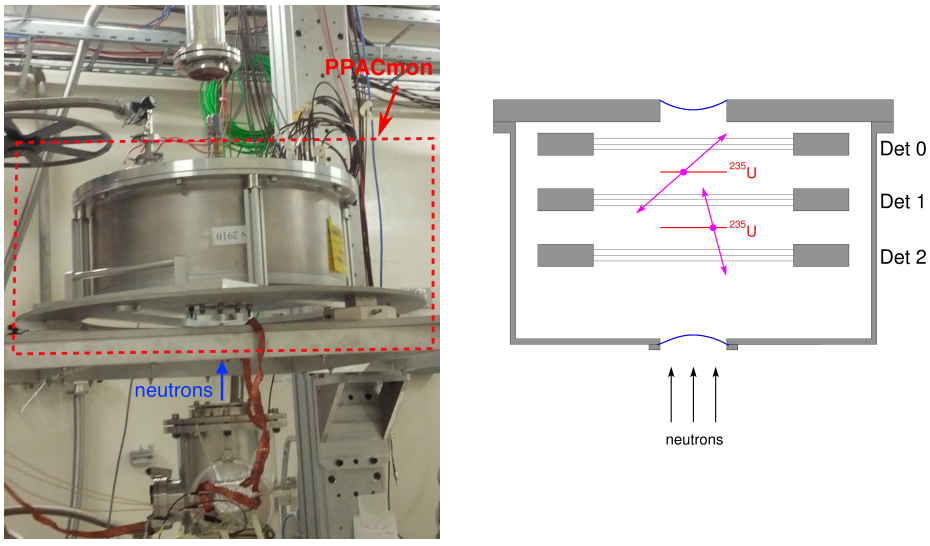

(a) **(b)**

Figure 4.7: PPACMon setup at EAR-2 - (a) PPACMon located on the vertical beam line (b) Drawing of 3 PPACs and 2 targets inside PPACMon which are orthogonal to the incoming neutron beam

4.3.2 PPAC setup at EAR-1

Figure 4.8 is the setup for measuring the ^{237}Np(n, f) cross section and FFAD at EAR-1. The horizontal neutron beam enters the chamber and goes through a stack of 10 PPACs interleaved with 9 target, figure 4.8b shows the inside structure of the chamber. The 45° tilted setup of detectors and targets regarding to neutron beam is used for decoupling the efficiency and FFAD and to cover FFAD in entire range. It will be dedicatedly discussed in chapter 6.

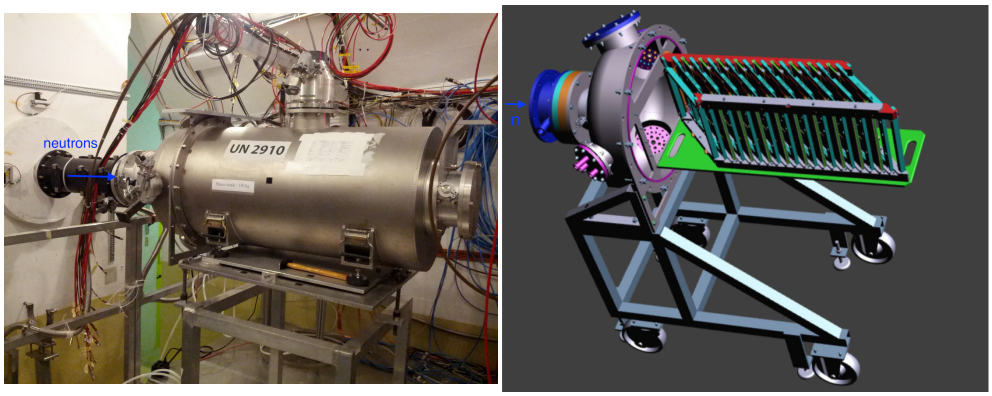

(a) (b)

Figure 4.8: PPAC chamber setup at EAR-1-(a) PPAC chamber located on the horizontal beam line (b) Ensemble drawing of the 10 detectors and 9 targets tilted by 45° against the incoming neutron beam

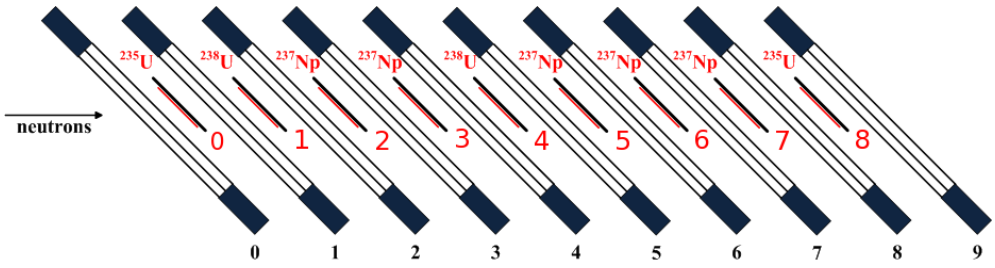

Figure 4.9: Detector and target sequence inside chamber - top view of detectors and targets

The detector and target sequence is sketched in figure 6.1. They are named consecutively from number 0 along the beam direction. There are 5 ^{237}Np targets. The first 2 of them (target 2 and 3) have thinner aluminium backings with a thickness of 0.7 μm,

the rest (target 5, 6, 7) have aluminium backings of 2 μm. Apart from ^{237}Np targets, we have 2 ^{235}U and 2 ^{238}U targets as reference targets. The first ^{235}U target (0) and the second ^{238}U target (4) have backings of 0.7 μm, while the other reference targets are 2 μm.

4.4 Detection systems at n_TOF

Several kinds of neutron-induced reaction measurements have been commissioned at n_TOF facility, among which the most significant ones are neutron-induced fission (n, f), capture and charged particle (n, cp) measurements. These systems have not been used in our experiments, but here we give a brief introduction to them.

4.4.1 Fission measurement

Apart from PPACs, a multi-stack Fission Ionization Chamber (FIC) and MicroMegas detector can be used for fission measurements.

FIC was used at n_TOF during phase-I (2001-2004) for fission cross section measurement. The target inside the chamber does not have to be as thin as for the PPAC since only one fission fragment is detected. It can be also used for monitoring the neutron beam.

Micromegas detector was used since n_TOF Phase-II (2009-2012) which is characterized by its good signal-to-noise ratio. It's a double-stage parallel plate chamber, a conversion gap and an amplification gap, separated by a micromesh. Charged particles firstly travel through the conversion gap where electron-ion pairs are produced and electrons drift toward micromesh. Then electrons enter into the amplification gap and they are multiplied due to the high electric field. The subsequent electron avalanche induces signals on the anode strips which can give the position information. Micromegas detector can also be used to detect neutron beam with a neutron/charged particle converter on the entry face[48].

4.4.2 Capture measurement

Two different detection systems have been set up for capture measurement: a segmented array of 40 B_aF_2 Total Absorption Calorimeter (TAC) [49] and an array of deuterated liquid scintillation detectors (C_6D_6).

40 BaF_2 crystals for detecting the $\gamma - ray$ cascade emitted in neutron capture reactions form a spherical shell, which covers 95% of 4π solid angle. The neutron sensitivity of the TAC is inhibited by combining the spherical neutron moderator/absorber made of $C_{12}H_{20}O_4(^6Li)_2$ surrounding the sample with the ^{10}B loaded carbon fiber capsules of the crystals. Capture events can be identified from competing reactions by reconstructing the total energy of the γ-ray cascade. TAC performs a high quality way for neutron capture measurements of small mass and/or radioactive samples at EAR-1.

The feature of C_6D_6 liquid scintillator is its low sensitivity to background signals induced by scattered neutrons thanks to the use of a thin-wall carbon fiber cell to cover the scintillator [50]. It's suitable for measuring light isotopes whose elastic scattering cross section is much higher than for capture.

4.4.3 (n, cp) measurement

(n, cp) reactions can be measured by Micromegas or Silicon-based detectors. Particularly, the setup of n_TOF EAR-2 facilitates the (n, cp) measurements with very low cross section thanks to its high neutron flux. For example, Micromegas has been used for ^{33}S(n, α) and ^7Be(n, α) measurements[18]. Recently, a new concept of Si-based detector has been developed with the sample sandwiched between two silicon detectors for detecting the back-to-back emission products in coincidence to reject the background.

Chapter 5

Flux and beam profile measurement at EAR-2

In this chapter, the experiment at EAR-2 for measuring the beam will be discussed in details. We shall present how we proceed the data analysis step by step. At the end, we shall give the results we are interested in: the integral neutron flux and beam profile.

5.1 Steps of the analysis

The Data Acqusition system (DAQ) of n_TOF consists of tens of 12 bits and 14 bits digitizers with sampling rates of 1 GS/s and 500 MS/s. The signals delivered from the detectors' preamplifiers are sent to these digitizers directly. DAQ system is triggered by the signal given by the proton beam. Once a proton bunch is delivered to the n_TOF spallation target, the DAQ is activated and digitize all of the present channels in a given time window. This DAQ system is very powerful because it records the full detector response, so that we can recover the full experiment offline and do some corrections (such as dead time, pile-up) if necessary. As a consequence, huge raw data are generated and stored in CASTOR at CERN [51]. For example, the total raw data generated at n_TOF in 2016 including both EAR-1 and EAR-2 is 1400 TB.

The analysis of the data starts from the raw data treatment. At this step, we directly access the raw data on CASTOR to extract the characteristic information of signals, such as time and amplitude, and write them into new DST (Data Summary Tape) files or ROOT [52] files which are much more reduced than raw data for further

analysis. With these new DST files or ROOT files, we can search the coincidences to identify fission events, reconstruct the trajectories of fission fragments and do other further analysis that we are interested in.

5.2 Raw data treatment

The main purpose of raw data treatment is to extract the relevant useful information from raw data for further analysis. Generally speaking, it is to scan the signal frames, to recognize the interesting pulses and pick out their characteristics, then write them into new files. There are two program packages that can treat the raw data of PPAC, one is the dedicated routine program for PPAC which can extract the useful information and write them into DST files, the other one is the n_TOF lib program developed by n_TOF collaboration which is a general treatment applicable to the wide range of detectors and signals. It writes results into ROOT files that can be directly accessed by ROOT program.

5.2.1 Dedicated PPAC routine

The dedicated PPAC routine recognizes the signals by applying derivative to signals above a setting threshold, since the waving of the baseline (especially close to the γ-flash region) could be removed and the signals of interest are still retained after derivative. However, the high frequency noise with low amplitude will be enhanced by direct derivative. So a low-pass filter is applied to smoothen the signals before derivative. Figure 5.1 [53] shows the original signals (one anode and two different cathodes) and their derivatives by convoluting the low-pass filter to remove the high frequency noise. It can be seen that the waving of the baseline at the beginning of the frame is completely removed after the derivative. The effect of high frequency noise in derivative is also inhibited since the filter is applied. However the signal peaks become bipolar.

Then two thresholds are set to the derivative bipolar signals for selection. In figure 5.2 [54], there is one anode derivative signal (blue) and one cathode derivative signal (red). The two red dash lines are the thresholds set for the derivative cathode signal. Signals crossing two thresholds with a lower-lower-upper-upper sequence are selected out. Their zero-crossing time and peak-to-peak amplitude, which are the peak time and proportional to the amplitude of original signals respectively, are saved in DST

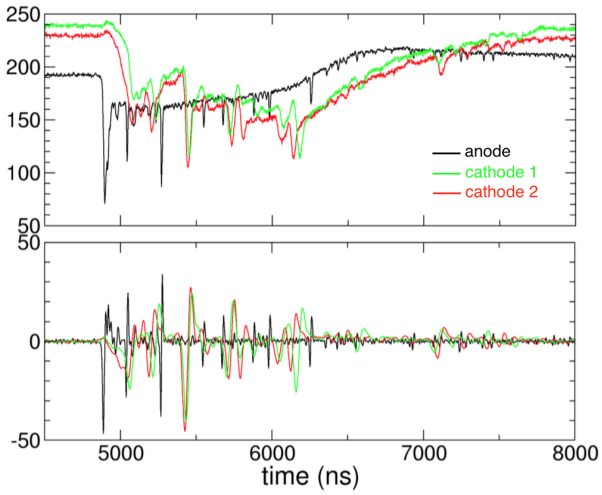

Figure 5.1: Upper part: Anode (black) and two cathode signals (red and green), Lower part: derivative of upper part with the convolution of low-pass filter

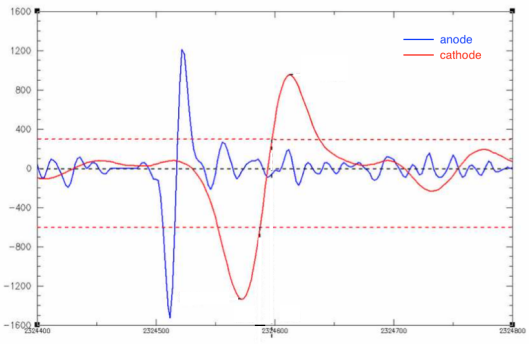

Figure 5.2: Thresholds setting applied to the derivative signal

files. Peak-to-peak amplitude of derivative signal is enough for PPAC since we are only interested in ratios of amplitudes in latter analysis.

5.2.2 n_TOF lib

The n_TOF lib package has the same philosophy as the PPAC routine to recognize the signals: first smoothen the original signals by filtering the high frequency noise, then calculate the derivative, finally recognize the signals by crossing the 2 thresholds with a lower-lower-upper-upper sequence. However, n_TOF lib can extract more signal information than PPAC routine since it is a general treatment that is applicable to a wide range of signals and detectors. For example, the output ROOT file generated by

n_TOF lib contains the following information of each signal:

- Amplitude and area of each signal (PPAC routine outputs the peak-to-peak amplitude of derivative signal instead). Since it fits the baseline of the signal frame, it can find the absolute amplitude and area. The red curve in figure 5.3 shows the fitted baseline.
- Rise time. The time interval for the leading edge to rise from 10% to 90% of the amplitude.
- FWHM (full width at half maximum of amplitude) and FWTM (full width at tenth maximum of amplitude) time.

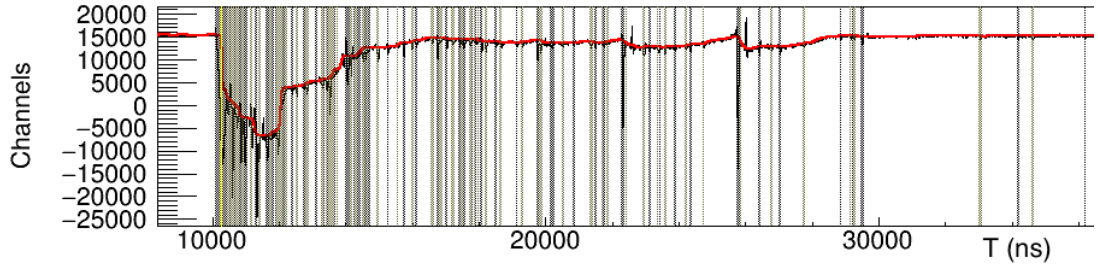

Figure 5.3: nTOFLib - Black line is an anode signal frame, red curve is the fitted baseline of signal frame.

5.3 Fission event identification by coincidence method

As mentioned in section 4.1.1, a fission event is identified by the coincidence of two adjacent PPACs surrounding the fissionning target. The diagram of the PPACMon chamber setup is shown again here (figure 5.4).

The anode signals are used for searching the coincident events. For each anode signal, we open a time window of 20 ns (from -20 ns to +20 ns) to select the coincident events. Figure 5.5 shows all the coincidences between PPAC2 and PPAC1. The horizontal axis is the anode time difference between PPAC2 and PPAC1 (T2-T1), the vertical axis is the anode amplitude of PPAC1 (A1). When a fission comes out from the central target between two adjacent PPACs, the two fission fragments reach each detector almost at the same time because they travel the same distance from target to detector. So they

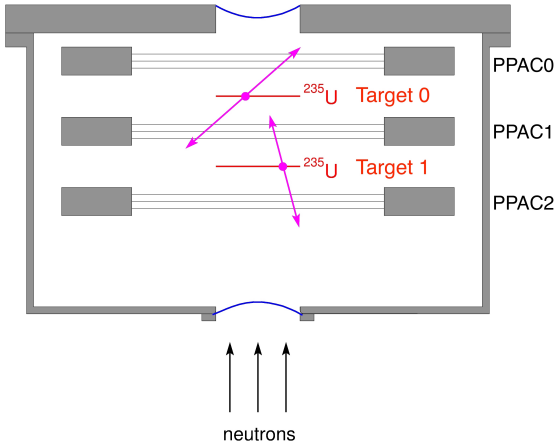

Figure 5.4: Diagram of the PPACMon chamber setup at EAR-2

are concentrated around $\Delta T \approx 0$. However, there is still a slight difference between the arriving time of two fission fragments due to the asymmetric mass division. That is, in asymmetric fission, the heavier fragment takes more time to reach the detector and releases less energy in the gas than the lighter one. That's why there are two separated bumps at central spot in figure. The left bump is mainly from the fission events that PPAC1 is hit by the heavier fragments because their flight time is longer than PPAC2, result in a negative value of T2-T1, and their amplitudes are lower due to the lesser energy they release.

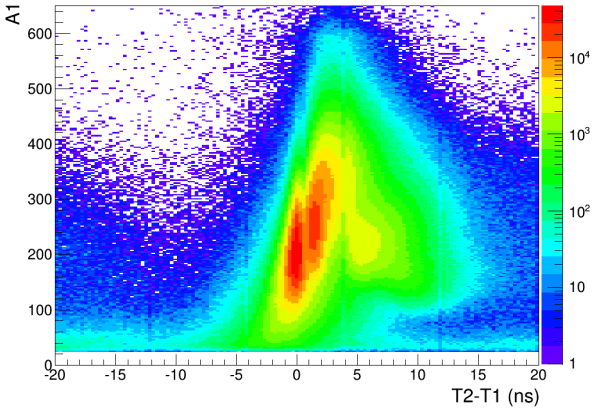

Figure 5.5: All the coincidences between PPAC2 and PPAC1 - 2D distribution of amplitude on PPAC1 versus the time difference between PPAC2 and PPAC1

There is an extra bump around 5 ns with amplitudes around 200. These events

are actually from fissions in target0 which have to be removed since they are not from the fissionning target1 that we are tagging. These fission fragments from target0, after crossing PPAC1, continue flying through target1 and are detected by PPAC2. In this case, one fission fragment crosses two detectors, the other oppositely emitted fragment is detected by the third detector, so that to the end there is a triple coincidence. We can use the time difference between PPAC2 and PPAC0 to identify the triple coincidences and determine the corresponding fissionning target. For fissions from target0, T2 is definitely larger than T0 because the travel distance from target0 to PPAC2 is three times to the path from target0 to PPAC0. Fission from the target1 is the reverse case. Figure 5.6 is the 2D distribution of anode time difference between PPAC2 and PPAC0 (T2-T0) versus the amplitude of PPAC2 (A2). It can be seen that two bumps are well separated, the left bump are the fissions from target1 since T2-T0 is less than 0 and the right part is from target0. We can apply a cut to count the left part from target1.

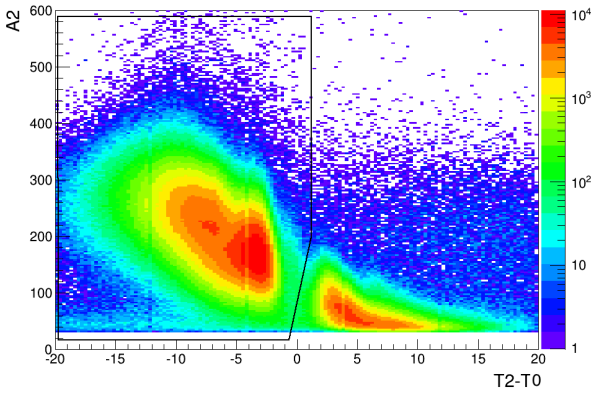

Figure 5.6: Distribution of triple coincidences - 2D distribution of the anode time difference between PPAC2 and PPAC0 versus anode amplitude of PPAC2 for all the triple coincidence events

Besides, we also need to reject the coincident events due to the spallation reactions. Spallation light nuclei coming from the impinging of high energy neutrons onto low Z elements in dead layers (C, O in mylar foil, Al in target backings and electrodes) can emit light particles (such as α particle), thus there is a coincidence between it and spallation residual. However, their amplitudes are so much lower compared with fission fragment that they can be rejected. The sum of the amplitude of the coincident events as a function of neutron energy is shown in figure 5.7. We'll explain how to determine

incident neutron energy in next section. Here we just show that there is a region for neutrons above 10 MeV with much lower amplitudes, these events are from spallation reactions instead of real fissions that has to be cut.

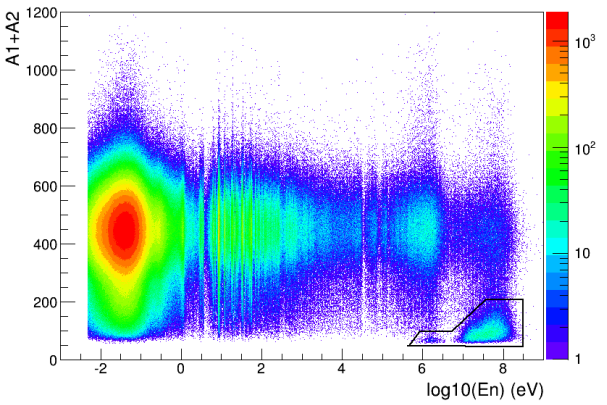

Figure 5.7: Distribution of sum of the anode amplitude of PPAC2 and PPAC1 as a function of neutron energy

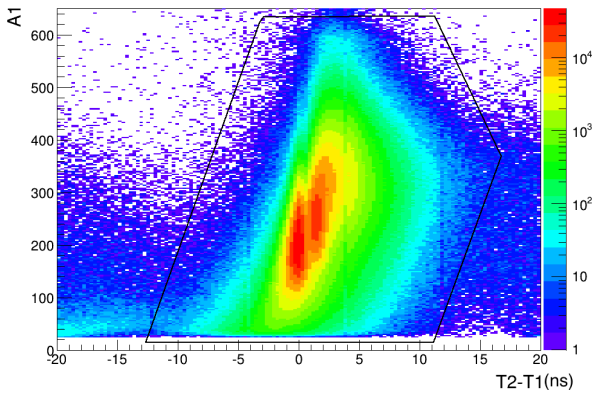

Figure 5.8: Coincidences between PPAC2 and PPAC1 only from the target1 - 2D distribution of anode time difference between PPAC2 and PPAC1 versus anode amplitude on PPAC1

Figure 5.8 shows the coincidences between PPAC2 and PPAC1 with the application of the triple coincidence identification and low amplitude cut, the extra bump from the triple coincidences is gone. Then we put another central cut as shown in the figure to insure we select coincidences more precisely and remove as much background as possible.

5.4 Neutron energy determination

The incident neutron energy is determined by its velocity

$$v = \frac{L}{T - T_0} \tag{5.1}$$

where L is the flight path, T is the time recorded by the detector and T_0 is the starting flight time. So $T - T_0$ is the time-of-flight (TOF). Among these 3 parameters, only T is precisely known because it is directly given by the anode of the PPAC. L and T_0 need to be determined. L is determined by the resonance peaks of ^{235}U at low energy (a few eV) where T_0 has a negligible impact because T is huge enough. And then T_0 is defined at high energy region where T is comparable to T_0. The details of defining the L and T_0 are discussed in following subsections.

5.4.1 Flight path L

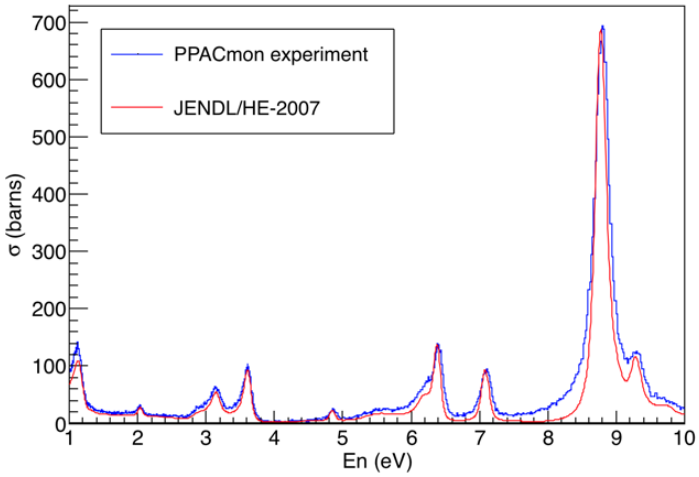

Figure 5.9: Comparison of the experimental fission rate and ^{235}U(n,f) cross section in the database

L is obtained by the comparison of the detected fission rate and the $^{235}U(n, f)$ cross section in database (JENDL/HE-2007) [55] at the resonance region where T is large enough to neglect T_0 so that we can use T instead of TOF. We compare the measured fission rate to the cross section in the database and use the sharp peaks to calibrate L. We know the flight path to EAR-2 is roughly around 20 m, so first we assume a

flight path around 20 m to calculate the fission rate as a function of neutron energy and compare it with $^{235}U(n, f)$ cross section in database. Then we adjust L until the best match is obtained. The comparison of fission rate with the cross section in database from 1 ev to 10 eV is shown in figure 5.9. The L determined here, 19.37 m, is the flight path including the moderation distance at this energy region. However we know from section 3.5 that the moderation distance varies with the energy. Therefore we can include the varying moderation distance (the most probable one) in the L determination which makes L depending on the neutron energy.

5.4.2 Starting flight time T_0

T_0 is usually determined by the prompt γ-flash signal which is a sharp narrow peak at the beginning of the signal frame in case of the measurement at EAR-1. But this method is not applicable here since the sharp peak is not visible at EAR-2. Instead, we use the pickup (PK) signal of proton beam as the time reference to determine T_0. Because the PK signal is delayed compared with the true T_0, an offset has to be added to determine TOF:

$$TOF = T - PK + offset \tag{5.2}$$

The offset is determined from both the the first fission event and simulation. Figure 5.10 is the TOF spectra of fission events with different offsets. It can be seen that the TOF spectra have an steep edge at the beginning which is supposed to be equal to the TOF of prompt γ-rays, because the first fission event could be induced by the prompt γ-rays or very high energy particles whose speed is very close to speed of light. The TOF of prompt γ-rays is

$$TOF_\gamma = \frac{L}{c} = \frac{19.37}{c} = 64.6\ ns \tag{5.3}$$

so the limitation of the TOF spectra should be located at 64.6 ns. It can be seen in figure 5.10 that the 1800 ns offset (red curve) is the good one. There are still several events before 64.6 ns, they are probably due to the width of the proton beam (7 ns RMS) and some background. With this determined 1800 ns offset, we can calculate the incident neutron energy by time-of-flight method and obtain the fission rate as a function of neutron energy.

The offset can be also checked by the simulation. The simulated fission rate can be obtained by multiplying ^{235}U(n, f) cross section [55] by a simulated flux, then we

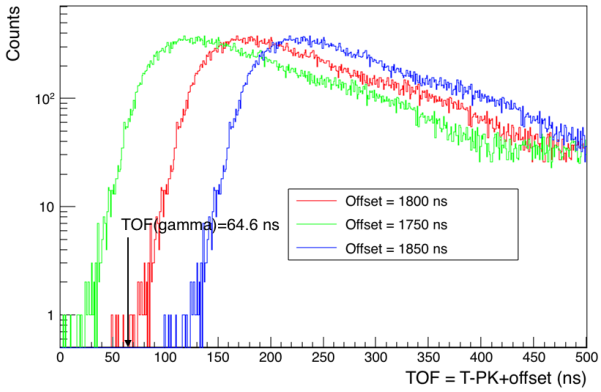

Figure 5.10: TOF spectrum with different offsets -

compare it to fission rate with different offsets (figure 5.11). It's clear that the fission rate with 1800 ns offset has a good agreement with simulated fission rate, especially at high energy (above 10 MeV). At low energy region, the fission rate is not sensitive to the offset because the TOF is so long that the offset influence is negligible.

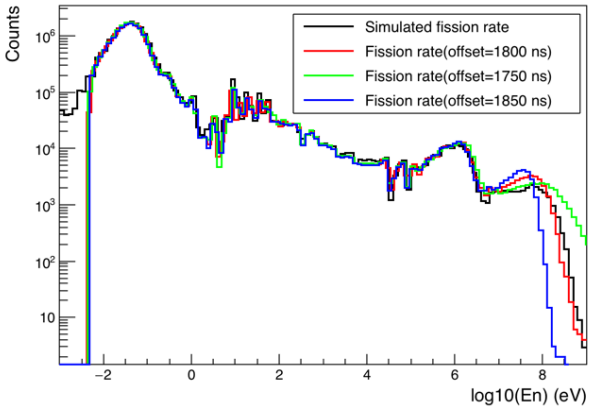

Figure 5.11: Comparison of fission rate with different offsets and simulation -

5.4.3 Fission rate

With the determined flight path L and T_0, we can obtain the TOF and the energy of the incident neutrons. The TOF spectrum and the fission rate as a function of neutron energy with 100 bins per decade (bpd) are shown in figure 5.12.

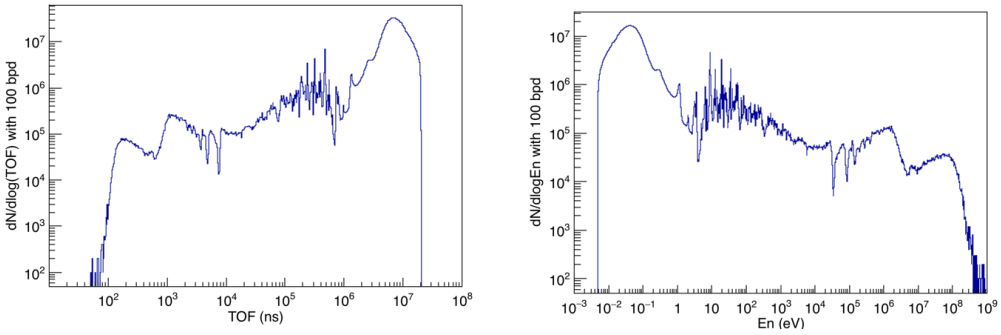

(a) Neutron TOF spectrum with 100 bpd **(b)** Fission rate with 100 bpd

Figure 5.12: TOF and fission rate spectra

5.5 Fission fragment localization

The fission events are selected by the coincidences of anode signals. However, the trajectories of fission fragments are obtained by cathode signals. As mentioned in section 4.1.2, each PPAC has two cathodes to measure the position of a fission fragment in two orthogonal directions. The strips on the cathode are connected to a delay line where the signals are propagated and read out at both ends by a preamplifier. So each cathode has 2 output signals. As a summary, one PPAC has five output signals: one anode signal for time measurement and four cathode signals for position measurement. The four cathode outputs are named as Left, Right, Top and Bottom based on the spatial setup. Left and Right signals give the position information on the horizontal direction, Top and Bottom provide the position on the vertical direction. The 5 output signals of one PPAC are shown in figure 5.13.

5.5.1 Localization method

The signal propagation in the delay is exemplified in figure 5.14. The cathode signal injected in the delay line at point x splits up into two signals that propagate oppositely until they reach the end.

The propagation time t_X is defined as

$$t_X = t_{SX} - t_{anode} \tag{5.4}$$

where X is one of the 4 cathode symbols $L(Left), R(Right), T(Top)$ or $B(Bottom)$,

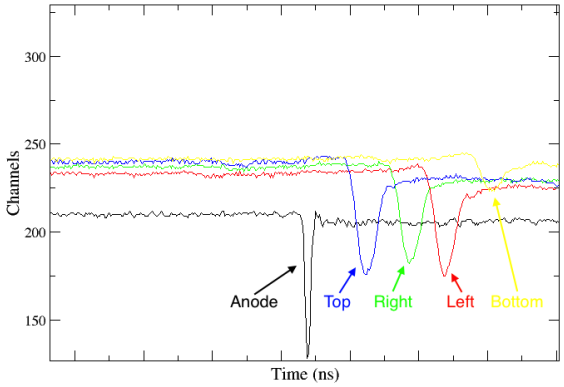

Figure 5.13: Five output signals of a PPAC

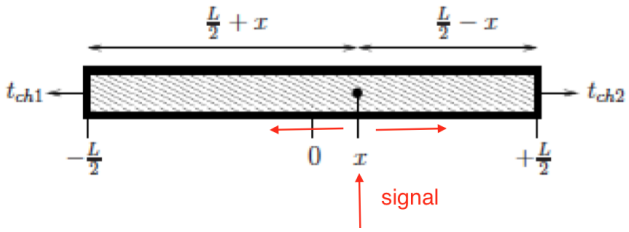

Figure 5.14: Signal propagation along a delay line of length L from a point x referred to the center.

t_{SX} is the peak time of the corresponding cathode signal, t_{anode} is peak time of the anode signal. The propagation time is:

$$\begin{aligned} t_{SL} - t_{anode} &= \delta t + \frac{\frac{L}{2}+x}{v} \\ t_{SR} - t_{anode} &= \delta t + \frac{\frac{L}{2}-x}{v} \end{aligned} \tag{5.5}$$

where v is the propagation velocity, L is the length of the delay line, δt is an additional delay taking into account the signal process in electronics. The position x can be obtained by making a subtraction of equation 5.5. The y position can be obtained in

same way based on Top and Bottom signal.

$$\begin{aligned} x &= \frac{v(t_{SR} - t_{SL})}{2} \\ y &= \frac{v(t_{SB} - t_{ST})}{2} \end{aligned} \tag{5.6}$$

The propagation velocity was measured with a fast signal generated by an electronic pulser. The signal was injected at different points of delay line, then we measured the time difference between two output signals at the both ends. With the given input position information, we can calculate the propagation velocity. With all the delay lines measured, we obtained an average propagation velocity: 2 mm/3.2 ns.

The equation 5.6 will be used for reconstructing the fission trajectory in following sections. For a given anode signal, we open a time window to search for the corresponding cathode signal couples (Left, Right) and (Top, Bottom). Then x and y position can be extracted by equation 5.6.

5.5.2 Cathode signal selection

From equation 5.4 and equation 5.5 we have the following relations:

$$\begin{aligned} t_L + t_R &= (t_{SL} - t_{anode}) + (t_{SR} - t_{anode}) = 2\delta t + \frac{L}{v} \\ t_B + t_T &= (t_{SB} - t_{anode}) + (t_{ST} - t_{anode}) = 2\delta t + \frac{L}{v} \end{aligned} \tag{5.7}$$

Above relations show that the sum of the propagation time is independent on the position but only depends on the total propagation time in the delay line which is determined by its length. This characteristic can be used as a selection criterion for cathode signals with the following procedure.

For each anode signal, we open a window starting from anode peak time and lasting 400 ns to record all the related Left and Right signals inside it. The 2D distribution of t_L versus t_R for all the anode signals of PPAC1 is shown in figure 5.15.

The highly concentrated events in diagonal region in figure 5.15 prove the relation in equation 5.7 is correct. The other events with some structures are due to the signal reflection and distortion in the delay line. The flat background events beyond the diagonal are from the high counting rate in the high energy region. The time intervals between signals are contracted in high energy region, one anode signal is followed by many cathode signals in a 400 ns window. As a consequence, many combinations show

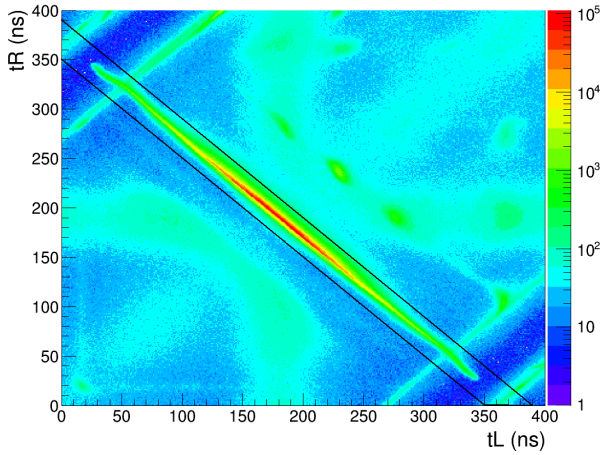

Figure 5.15: 2D plot of t_L versus t_R - All the combinations consists of one Left and one Right signal inside 400 ns windows for the anode signals of PPAC1 without coincidence requirement.

up and results in a flat background. A contour cut for diagonal region as shown in figure 5.15 can reject most of the background and select out the proper combinations of Left and Right signals.

After above selection criterion, some times, especially in high energy region, there are still more than one combinations of t_L and t_R present for one given anode signal. It brings ambiguity for selecting the correct combination since in principle one anode signal only generates one combination. In this case, we take into account the amplitude of two signals. The amplitude ratio of two signals at each end of one delay line should be almost constant because they are originally from the same signal injected on the delay line and the attenuation in the delay line is low. This gives another criterion to determine if a Left signal is probably associated with a Right signal. Figure 5.16 shows the relation between amplitude ratio and time difference of Left and Right signal. a_L and a_R is the amplitude of Left and Right signal.

It can be seen in figure 5.16 that most of the events are concentrated around $a_L/a_R = 1$. The slight slope of the distribution is due to the attenuation in the delay line. For example, when it goes to the positive direction, Left signal propagates more distance than Right signal, so the attenuation of Left signal is larger and the a_L/a_R ratio is decreasing.

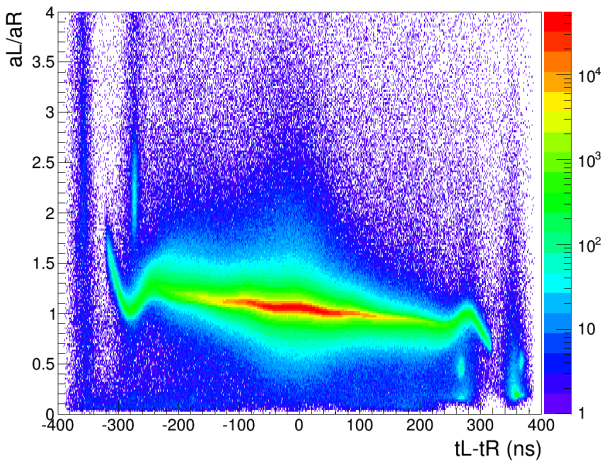

Figure 5.16: 2D plot of $t_L - t_R$ versus a_L/a_R for events in contour of figure 5.15

When there are more than one combination present for one given anode signal, we use the above two criteria to select the proper combination with the following algorithm. For all the events inside the diagonal contour in figure 5.15, figure 5.17a is the distribution of sum of the t_L and t_R with its mean (M1) and RMS ($\delta 1$) value, figure 5.17b shows the distribution of ratio a_L/a_R with its mean (M2) and RMS ($\delta 2$) value.

For each combination, we calculate the deviation from the mean value by weighting these two distributions with the following equation:

$$\delta = (\frac{t_T + t_B - M1}{\delta 1})^2 + (\frac{a_B/a_T - M2}{\delta 2})^2 \tag{5.8}$$

Then we chose the combination whose deviation is the smallest.

5.6 Beam profile reconstruction

The methods for searching the anode coincidences and for selecting the proper cathode signals for a given anode signal have been presented respectively. With coincidence and localization information, we can reconstruct the position distribution of fission fragments hitting the detectors and then obtain the beam profile. The algorithm proceeds as follows:

1) Scan the anode signals of two adjacent PPACs to find coincident events within a $\pm$20 ns window.

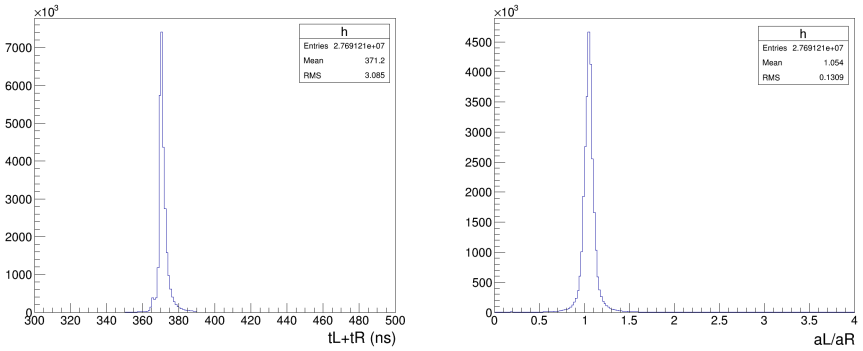

(a) Distribution of $t_L + t_R$ **(b)** Distribution of a_L/a_R

Figure 5.17: 1D distributions for events in contour of figure 5.15

2) For each coincident event, open a 400 ns window for each anode signal respectively to look for the corresponding cathode combination (Left, Right) and (Top, Bottom) with the sum limitation (diagonal contour in figure 5.15).

3) If more than one cathode combinations are present, we use the method described in section 5.5.2 to select out the most proper one. We save these coincident events with complete localization information for latter analysis.

Several cuts as shown in figure 5.6, figure 5.7 and figure 5.8 have also to be applied to identify the fissioning target and reject the low amplitude background events before reconstruction.

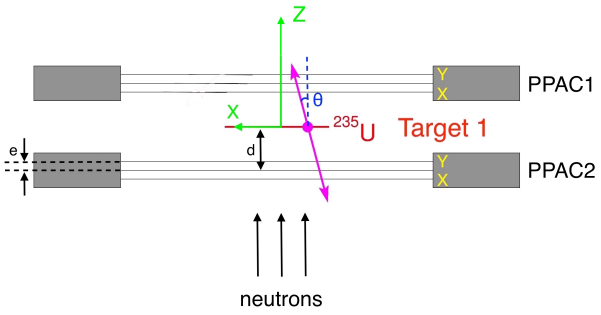

Figure 5.18: Diagram of the first detection cell in PPACmon chamber.

Figure 5.18 presents the PPAC1, PPAC2 and Target 1 in figure 5.4 with additional geometric information to exemplify the reconstruction process. As depicted in figure, we define the neutron beam direction as the Z axis. To follow the right-hand system,

we define the X axis pointing from right to left, Y axis is pointing out perpendicularly to the figure plane. The origin of the coordinate system locates on the target plane. The first cathode following the beam direction determines the position in X axis (we refer this cathode as X plane), the second cathode determines the Y position (Y plane). d is the distance from the ^{235}U target to anode, e is the distance between each anode and cathode. θ is the fission angle between fission fragment trajectory and neutron beam. We can obtain the (X, Y) position of fission fragments on each detector by equation 5.6. Figure 5.19 shows the distribution of fission fragment hitting points on PPAC1 and PPAC2.

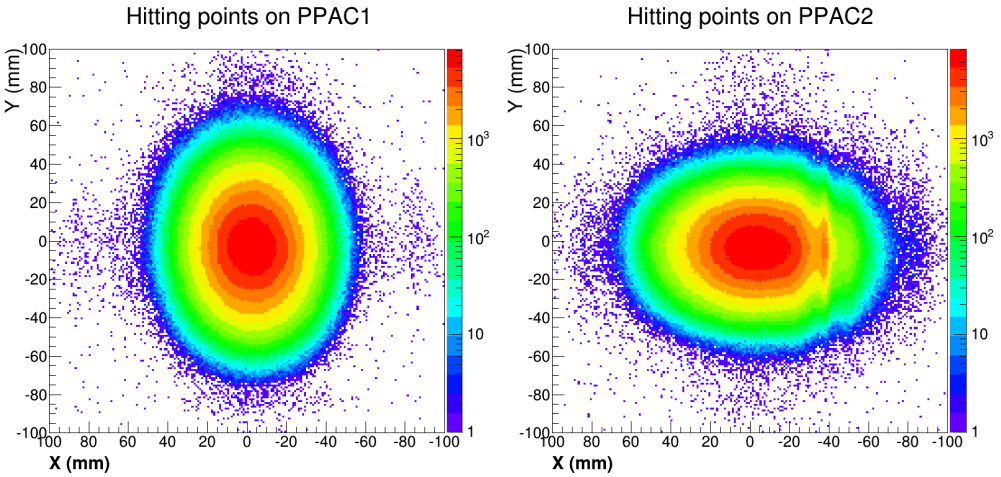

(a) Distribution on PPAC1 **(b)** Distribution on PPAC2

Figure 5.19: Distribution of fission fragment hitting points on PPAC1 and PPAC2

In figure 5.19 we can see the distributions are elongated, this is because the X and Y position are determined by two different cathodes and there is a gap between them. For example, let's look at the distribution on PPAC1 (figure 5.19a) whose X plane is closer to target than Y plane. It means fission fragment travels longer distance to reach Y plane, as a consequence the distribution in Y axis is extended. PPAC2 is the reverse case. In figure 5.19b there is a distorted region around -40 mm$\leq$X$\leq$-20 mm and -20 mm$\leq$Y$\leq$20 mm . This is caused by a hardware problem of PPAC2 during the experiment.

Since the two fission fragments are emitted in a back to back direction, we can

calculate the position of the emitting point on the target by the equation of a straight line. We define (X_1, Y_1), (X_2, Y_2) are the coordinates of hitting point respectively on cathode plane of PPAC1 and PPAC2. Z_{1X}, Z_{1Y}, Z_{2X}, Z_{2Y} are the Z coordinates of hitting point respectively on X and Y plane of PPAC1 and PPAC2. (X, Y, Z) is the coordinate of emitting point on target where Z is 0. Their relations are :

$$\begin{aligned} \frac{X - X_1}{X_2 - X_1} &= \frac{Z - Z_{1X}}{Z_{2X} - Z_{1X}} = \frac{d+e}{2d} \\ \frac{Y - Y_1}{Y_2 - Y_1} &= \frac{Z - Z_{1Y}}{Z_{2Y} - Z_{1Y}} = \frac{d-e}{2d} \end{aligned} \tag{5.9}$$

from which we can reconstruct the position (X, Y) on target by:

$$\begin{aligned} X &= \frac{(d+e)X_1 + (d-e)X_2}{2d} \\ Y &= \frac{(d-e)Y_1 + (d+e)Y_2}{2d} \end{aligned} \tag{5.10}$$

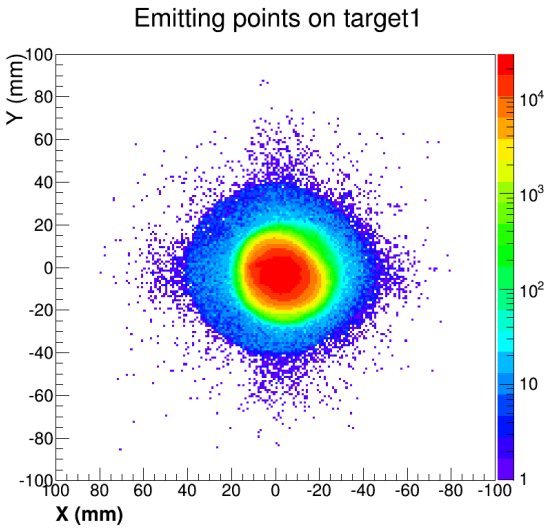

Figure 5.20: Neutron beam profile at n_TOF EAR-2 with small collimator

Figure 5.20 is the distribution of emitting points on the target1. This distribution also stands for the beam profile since the target is uniform. It can be seen that the beam profile is well collimated, circular and well centered. The interesting feature of this beam profile is that it's not as uniform as at EAR-1 which will be shown in section 6.3 (figure 6.7). The beam intensity drops lower toward periphery. This is probably caused by the conical collimator setup [41] that is different with the cylinder collimator design for EAR-1.

The fission angle $\cos\theta$ and the azimuth angle ϕ can be calculated by equation 5.11.

$$\begin{aligned} \cos\theta &= \frac{2d}{\sqrt{(X_2 - X_1)^2 + (Y_2 - Y_1)^2 + (2d)^2}} \\ tan\phi &= \frac{Y_2 - Y_1}{X_2 - X_1} \end{aligned} \tag{5.11}$$

We can use the same reconstruction method (equation 5.12) to project the X, Y positions on the two cathodes on the central anode plane.

$$\begin{aligned} X_{1anode} &= \frac{(2d+e)X_1 - eX_2}{2d} \\ Y_{1anode} &= \frac{(2d-e)Y_1 + eY_2}{2d} \\ X_{2anode} &= \frac{eX_1 + (2d-e)X_2}{2d} \\ Y_{2anode} &= \frac{-eY_1 + (2d+e)Y_2}{2d} \end{aligned} \tag{5.12}$$

where (X_{1anode}, Y_{1anode}) and (X_{2anode}, Y_{2anode}) are the coordinates of hitting points on the anode plane of PPAC1 and PPAC2.

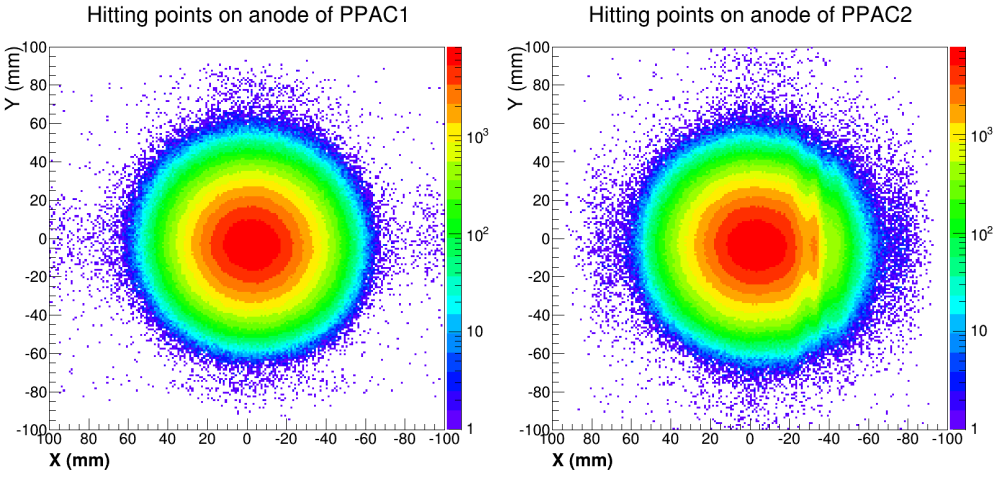

(a) Distribution on anode of PPAC1 **(b)** Distribution on anode of PPAC2

Figure 5.21: Distribution of fission fragment hitting points on the anode plane

Figure 5.21 is the distribution of hitting points on the anode plane of PPAC1 and PPAC2, the distribution is completely symmetric since the X and Y coordinates are projected on the same point on the anode plane.

5.7 Integral neutron flux at EAR-2

To obtain the neutron flux, we need to determine the efficiency ε and take into account the anisotropy of FFAD for neutrons above 1 MeV.

5.7.1 Efficiency determination

The coincidence method limits the detection efficiency of PPACs because it requires both fission fragments emerge out from the target, traverse the electrodes and reach the second gap. This is illustrated in figure 5.22 where the fissile target is red and the dead layers (aluminium target backing and mylar electrodes) are pink. It's easy for both fission fragments to be detected at small fission angle ($\theta 1$), whereas it's more difficult at large angle ($\theta 2$) because the travel path is increasing with the increase of fission angle, especially difficult for the fission fragment that has to additionally cross the target backing. So the stopping of the fission fragments before reaching the second gap at large angle limits the efficiency of PPAC. On the contrary, we can take the efficiency at fission angle $\theta = 0°$ as 100% since the fission fragments are traversing the minimum distance.

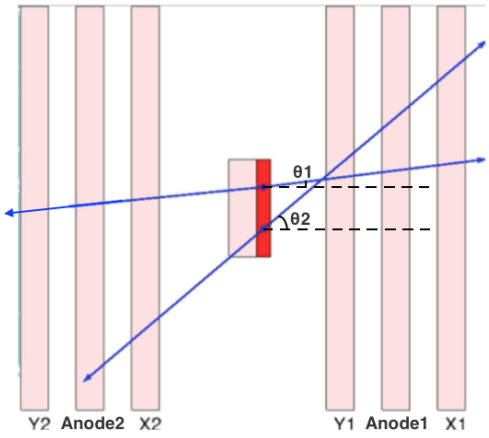

Figure 5.22: Illustration of fission fragment lost due to the large fission angle

The measured angular dependencies in different energy regions are shown in figure 5.23 where horizontal axis is the cosine of fission angle θ. In figure 5.23a where the FFAD is isotropic due to the low incident energy of neutrons, we can see that at small

angles ($\cos\theta$ close to 1) the curve is flat and is not decreasing with the increase of θ which implies the efficiency at small angles is 100%.

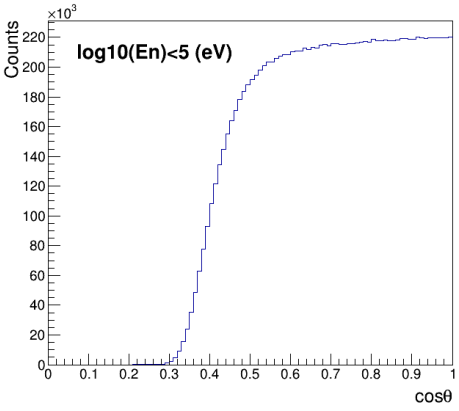

(a) Neutron energy: $\log_{10}E_n < 5$ (eV)

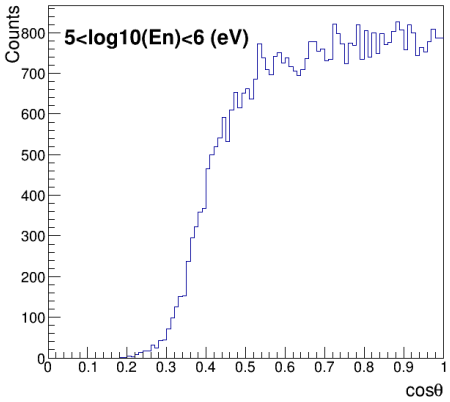

(b) Neutron energy: $5<\log_{10}E_n <6$ (eV)

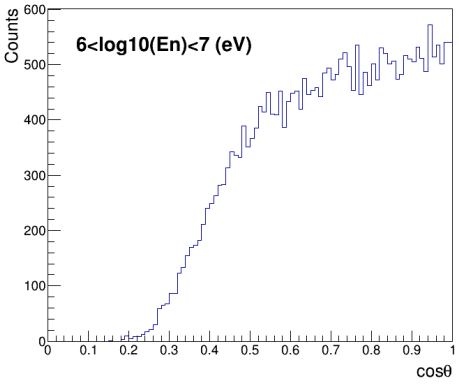

(c) Neutron energy: $6<\log_{10}E_n <7$ (eV)

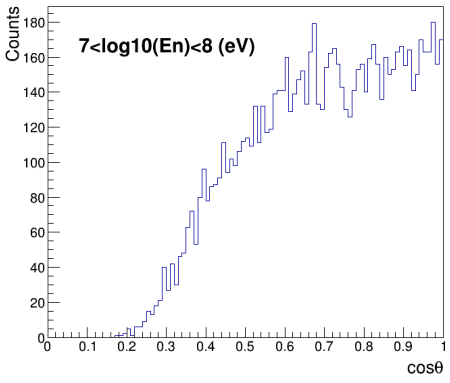

(d) Neutron energy: $7<\log_{10}E_n <8$ (eV)

Figure 5.23: Distributions of fission angle dependence in different neutron energy regions

The measured angular dependence at any direction is the multiplication of efficiency and FFAD, so based on one of them we can deduce the other one. Here we use the FFAD of ^{235}U that we measured in 2012 [53] with tilted setup to obtain the efficiency. The FFAD $W(\theta)$ in the center-of-mass frame can be represented by equation 5.14 [56]:

$$W(\theta) = K_{norm}(1 + (A-1)\cos^2\theta) \tag{5.13}$$

where θ is the fission angle, K_{norm} is a normalization factor, A is the anisotropy factor defined as

$$A = \frac{W(0°)}{W(90°)} \tag{5.14}$$

that we've already measured.

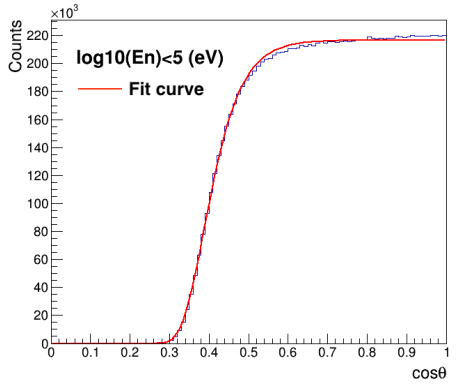

(a) Neutron energy: $\log_{10}E_n$ <5 (eV)

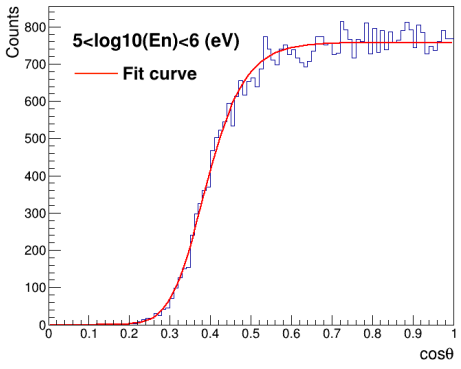

(b) Neutron energy: 5<$\log_{10}E_n$ <6 (eV)

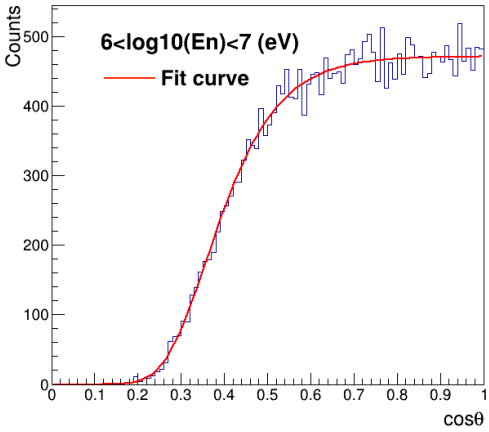

(c) Neutron energy: 6<$\log_{10}E_n$ <7 (eV)

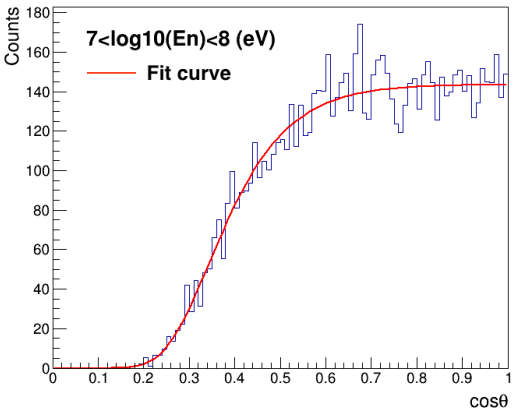

(d) Neutron energy: 7<$\log_{10}E_n$ <8 (eV)

Figure 5.24: Distribution of fission fragment angular dependence corrected by FFAD in different energy regions

The efficiency distribution as a function of $\cos\theta$ in each energy region can be achieved by dividing the angular dependencies in figure 5.23 by the corresponding FFAD. Figure 5.23a is the distribution for the neutrons under 100 keV with an isotropic FFAD due to the low incident neutron energy, so it is directly reflecting the efficiency distribution.

For the other distributions in figure 5.23 the FFAD is not isotropic any more, so we divide them by the corresponding FFAD to figure out the efficiency. Figure 5.24b, 5.24c and 5.24d are the distributions of figure 5.23b, 5.23c and 5.23d after the anisotropy correction. They reflect the efficiency distributions as a function of $\cos\theta$ in each energy range. They can be fit (red curves in figure 5.24) by a Fermi-like function (5.15) :

$$\varepsilon(\cos\theta) = \frac{a_0}{(1 + e^{a_1 - a_2\cos\theta})^{a_3}} \tag{5.15}$$

with the 4 parameters a_0, a_1, a_2, a_3 to be fit.

Figure 5.25 shows the efficiency curves normalized to 1 at 0° in different energy ranges. Their integrals give the global efficiency: 58.2%, 60.0%, 59.1% and 60.0% for energy range of (0, 100 keV), (100 keV, 1 MeV), (1 MeV, 10 MeV) and (10 MeV, 100 MeV) respectively. The similarity of the efficiency distribution and the global efficiency value in different energy ranges indicates that PPAC's efficiency is not very sensitive to neutron energy. The fitted efficiency function will be used for deducing the flux in next section.

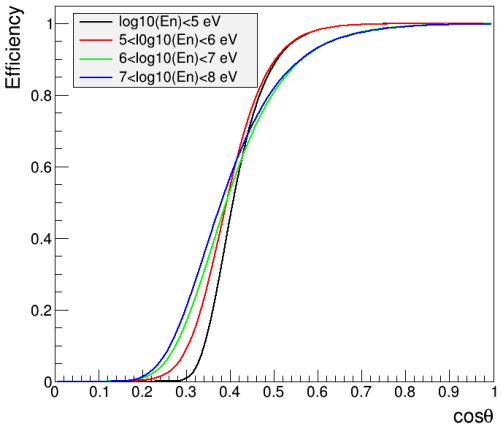

Figure 5.25: Efficiency curve of target1 in different energy regions

5.7.2 Flux calculation

The measured fission rate at neutron energy E_n in direction θ is:

$$dR(E_n, \cos\theta) = \Phi(E_n) \cdot \sigma(E_n) \cdot N \cdot \varepsilon(E_n, \cos\theta) \cdot W(E_n, \cos\theta) \cdot d\Omega_{\cos\theta} \tag{5.16}$$

where

- E_n is the neutron energy,
- R is the fission rate,
- Φ is the neutron number integrated on the target surface which is called integrated neutron flux here,
- σ is the neutron-induced fission cross section of ^{235}U (JENDL/HE-2007 evaluation is used here for calculating the flux)
- ε is the efficiency,
- N is the target thickness that can be measured by α counting in a well-defined geometric system,
- $d\Omega_{\cos\theta}$ is the solid angle at direction θ

Since the azimuth angle ϕ is isotropic and ranges uniformly from $-\pi$ to π, we have

$$d\Omega_{\cos\theta} = 2\pi d\cos\theta \tag{5.17}$$

Figure 5.26 shows the correlation between $\cos\theta$ and ϕ, where (a) is the 2D distribution of $\cos\theta$ versus ϕ and (b) is a projection of a vertical slices at $\cos\theta = 0.9$. It can be seen that at a given $\cos\theta$ we can treat ϕ as a uniform distribution and calculate its differential solid angle by equation 5.17.

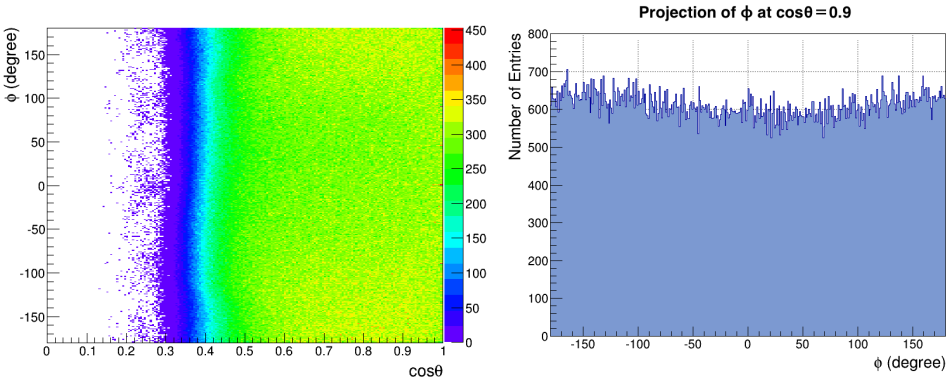

(a) **(b)**

Figure 5.26: Distribution in angles $(\cos\theta, \phi)$-(a) 2D distribution of $\cos\theta$ versus ϕ (b) Projection of a vertical slice, where $\cos\theta = 0.9$, in (a)

From equation 5.16 we can calculate the unnormalized integral neutron flux at E_n by:

$$\Phi(E_n) = \frac{R(E_n)}{\sigma(E_n) \cdot \int_0^1 \varepsilon(E_n, \cos\theta) W(E_n, \cos\theta) d\cos\theta} \tag{5.18}$$

Combining equation 5.18 with equation 5.13 and equation 5.15 we can obtain the unnormalized flux up to 200 MeV as shown in figure 5.27.

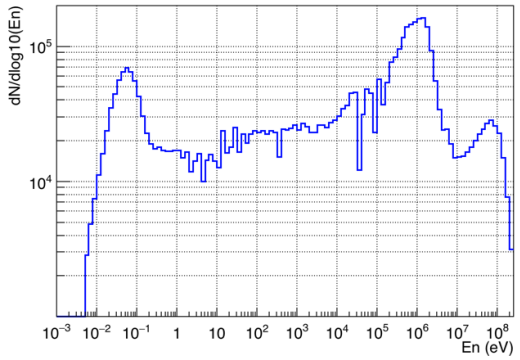

Figure 5.27: Unnormalized integral neutron flux at n_TOF EAR-2 with small collimator - Measured by PPACmon from thermal neutrons up to 200 MeV

A more dedicated and specific work for evaluating the EAR-2 integral neutron flux was done by n_TOF collaboration [43]. In this work, four detection system (Silicon Monitor, MicroMegas detector, MicroMegas monitor and PPACmon) and three neutron-induced reactions (^{6}Li(n, α), ^{10}B(n, α) and ^{235}U(n, f)) are used to characterize the absolute integral neutron flux. The results from PPACmon we present here are the only available data at high energy region (from 5 MeV to 100 MeV) thanks to its very fast signal and high time resolution. Figure 5.28 is the comparison between PPACmon and evaluated flux where PPACmon data is normalized to the evaluation. From it we can see that PPACmon can cover a large energy range. The fluctuation of PPACmon at resonance region (from 1 eV to 1 keV) is due to the influence of the resolution function λ that has been introduced in section 3.5 which is corrected in the evaluation.

5.8 Summary

We give the results of beam profile and integral neutron flux for the new neutron beam line EAR-2 at n_TOF . The beam is well centered and well collimated to circular. The

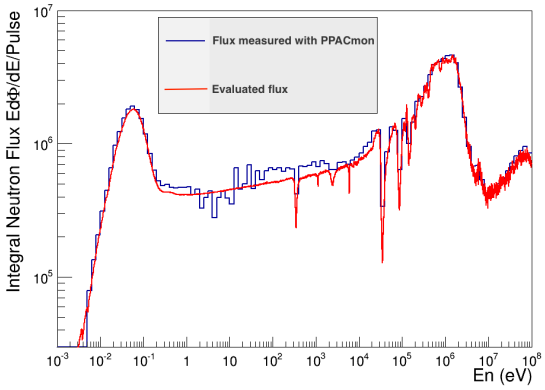

Figure 5.28: Comparison of integral neutron flux at n_TOF EAR-2 with small collimator between results from PPACmon and evaluation

interesting feature is that the intensity of beam profile decreases toward the periphery area instead of a uniform distribution as in EAR-1. This is probably caused by the conical design of the collimator at the entrance of the EAR-2. We also obtained the unnormalized integral neutron flux of EAR-2. PPACmon is the only detection system at n_TOF able to provide the data for high energy region (from 5 MeV to 100 MeV) thanks to its good time resolution and fast signal.

Chapter 6

^{237}Np(n, f) experiment at EAR-1

In this chapter, we will present the analysis of the measurement on neutron-induced fission of ^{237}Np at EAR-1. The analysis method we are using for extracting the cross section and FFAD will be described. Then we will show some results. The discussion on the results of ^{237}Np will be presented in next chapter.

6.1 Target and detector sequence

The setup of ^{237}Np(n, f) measurement at EAR-1 has been introduced in section 4.3.2, here we show the target and detector sequence again as a reminder. As depicted in figure 6.1, we refer the detectors and targets from left to right as PPAC0, PPAC1, ..., PPAC9 and target1, target2, ..., target8. In the later part of this chapter, we take the cases of target6 (cell consisting of PPAC6, ^{237}Np target, PPAC7) and target8 (cell consisting of PPAC8, ^{235}U target, PPAC9) to exemplify the analysis.

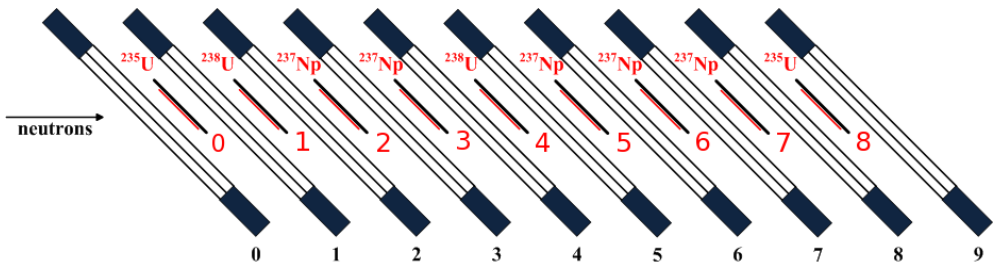

Figure 6.1: Detector and target sequence inside chamber

6.2 Fission event identification

The selection of the fission events follows the same procedure as in the case of PPACmon as described in section 5.3. We open a window from -20 ns to +20 ns as the coincidence time to select the fission events. As shown in figure 6.2, we can simply use a graphical cut to select the central spot where the events are from target8 (^{235}U).

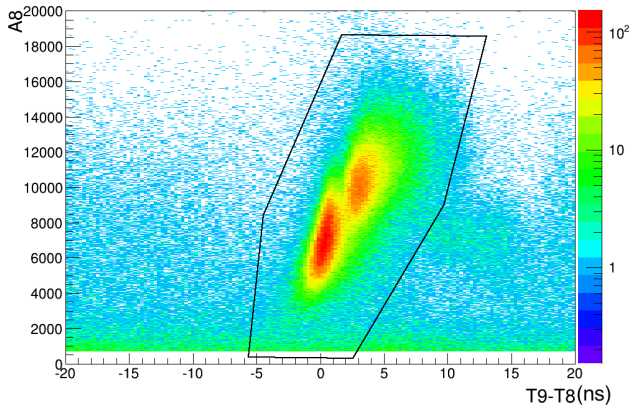

Figure 6.2: Coincidences between PPAC8 and PPAC9 - 2D distribution of anode time difference between PPAC8 and PPAC9 (T9-T8) versus the anode amplitude of PPAC8 (A8)

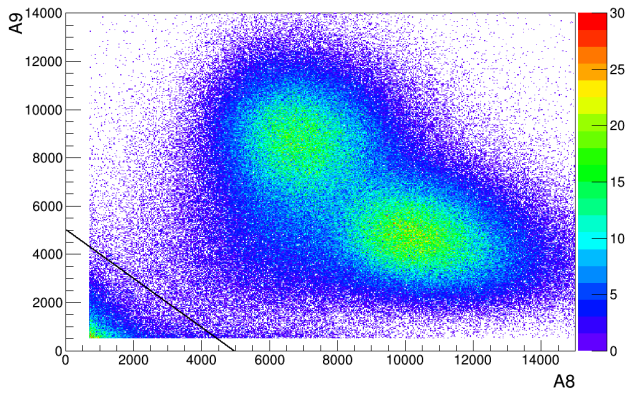

Figure 6.3: 2D distribution of anode amplitude of PPAC8 (A8) versus the anode amplitude of PPAC9 (A9) for the coincidence events

After the coincidence selection, we also need to reject the events with low amplitude that are not true fission events. Figure 6.3 shows the correlation between the anode

amplitude of PPAC8 and PPAC9 for the events inside the central graphical cut in figure 6.2. The two separated bumps corresponding to the asymmetric division of the ^{235}U target. It can be seen that the low amplitude events are so far away from the fission events that we can put a threshold for the sum of A8 and A9 to reject them. These low amplitude events are mainly the random coincidences from spallation in high energy region that has been described in section 5.3.

6.3 Fission trajectory reconstruction

To reconstruct the fission trajectory, first we need to choose the corresponding proper cathode signals for each anode signal. Here we follow the same procedure as described in section 5.5.2, which is based on the sum of the propagation time of each delay line and on the ratio of amplitude, to find the right cathode signals. Figure 6.4 shows the distribution of propagation time and the ratio of the amplitude of one cathode of PPAC8. The definition of propagation time is introduced in section 5.5.1 and equation 5.4.

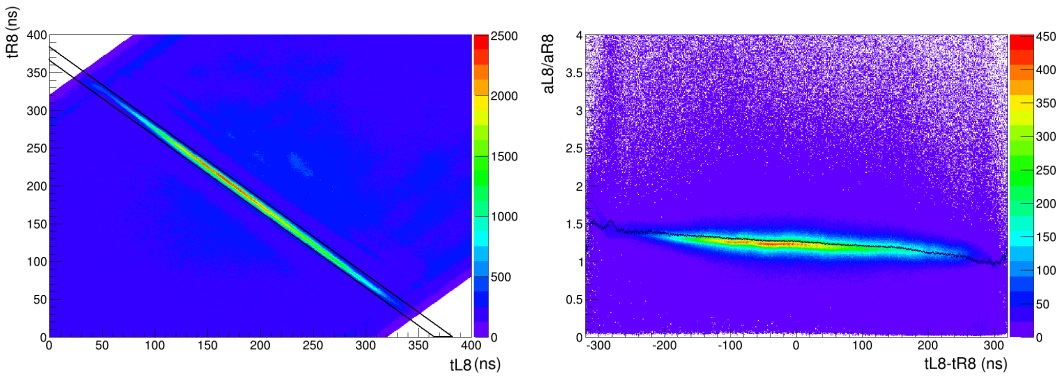

(a) **(b)**

Figure 6.4: Statistics of one cathode of PPAC8-(a) 2D distribution of propagation time, t_{L8} is the propagation time of the Left signal of PPAC8, t_{R8} is for the Right signal;(b) 2D distribution of amplitude ratio versus the difference of propagation time, a_{L8} is the amplitude of the Left signal of PPAC8, a_{R8} is the amplitude of the Right signal.

We select the events in the diagonal contour in figure 6.4a since the their sum should be a constant. Figure 6.4b is the distribution of the events inside the diagonal region which could be used as a supplementary selection criterion when more than one

combinations of Left and Right signal are present. The black curve in figure 6.4b is the profile of 2D distribution.

With the determined corresponding cathode signals for each anode signal, we can obtain the coordinates of the hitting points (X_d, Y_d) on each cathode plane (with the cathode center as the origin) by equation 6.1

$$\begin{aligned} X_d &= \frac{v(t_{SL} - t_{SR})}{2} \\ Y_d &= \frac{v(t_{SB} - t_{ST})}{2} \end{aligned} \tag{6.1}$$

where t_{SL}, t_{SR}, t_{ST} and t_{SB} are the peak time of Left, Right, Top and Bottom signal as has been defined in equation 5.4.

The top view of a basic cell of the tilted setup is shown in figure 6.5. The neutron beam enters each detector by X plane and exits from Y plane. The detectors are always centered on the beam axis. d is the distance from the target to the anode, e is the distance between anode and cathode. We define the point where the beam axis intersects the target plane as the origin of the frame (there could be an offset from target center to the origin). The reconstruction of fission trajectory is carried out in a perpendicular frame ($\vec{X}'$, $\vec{Y}'$, $\vec{Z}'$) (see in figure 6.5) where we define the X' axis as horizontal pointing from right to left, the Y' axis as vertical pointing upward and Z' axis as perpendicular to the detectors and target orienting at 45° from the beam direction. θ' and ϕ' are the polar angle and azimuth angle of the fission trajectory against and around Z' axis. θ and ϕ are the physical angles which are directly related to the beam axis. The relation between (θ', ϕ') and (θ, ϕ) will be discussed later.

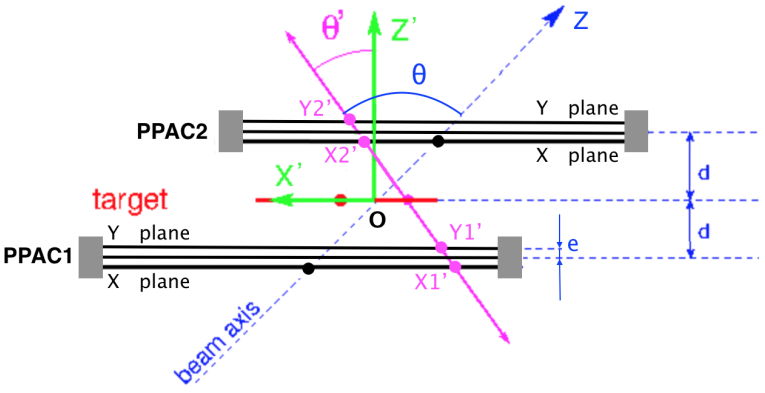

Figure 6.5: top view of a basic cell of tilted setup

The coordinates of the hitting points on PPAC1 in the perpendicular frame are

$$\begin{aligned} X_1' &= X_{1d} + d + e \\ Z_{1X}' &= -(d+e) \\ Y_1' &= Y_{1d} \\ Z_{1Y}' &= -(d-e) \end{aligned} \tag{6.2}$$

where (X_1', Z_{1X}') is the coordinates of the hitting points on the X plane, (Y_1', Z_{1Y}') is the coordinates on the Y plane. X_{1d} and Y_{1d} are the coordinates obtained by equation 6.1 taking the cathode geometric center as the reference origin. The coordinates of the hitting points on PPAC2 in perpendicular frame can be obtained by equation 6.3.

$$\begin{aligned} X_2' &= X_{2d} - (d-e) \\ Z_{2X}' &= d - e \\ Y_2' &= Y_{2d} \\ Z_{2Y}' &= d + e \end{aligned} \tag{6.3}$$

The distribution of the hitting points on PPAC8 and PPAC9 reconstructed by equation 6.2 and 6.3 are shown in figure 6.6. The cut line around X=10 in figure 6.6b is apparently caused by a strip at this position which was probably not working (no output signal from this strip) during the experiment.

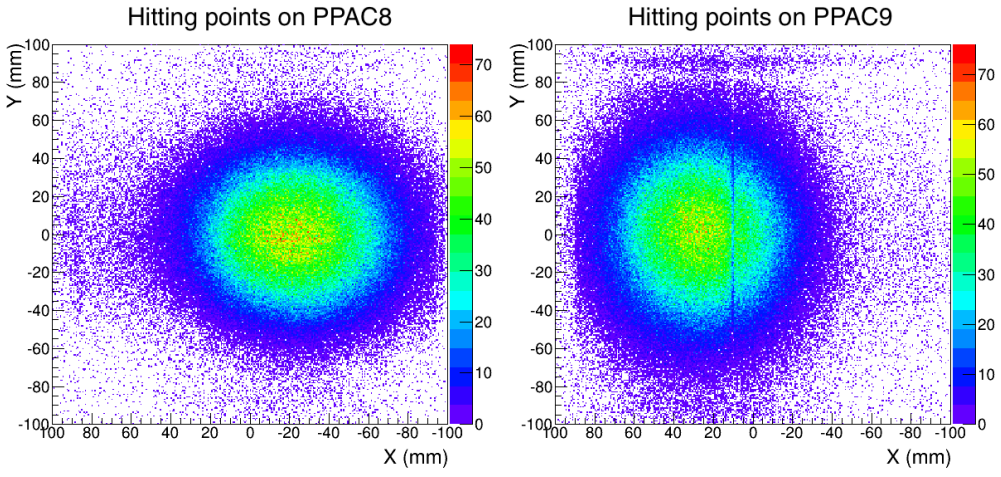

(a) **(b)**

Figure 6.6: Distribution of fission fragment hitting points on PPAC8 and PPAC9

From equations 6.2, 6.3 and based on the straight line equation 5.9, the emitting points on the target (X'_T, Y'_T) in the perpendicular frame can be calculated by equation 6.4.

$$\begin{aligned} X'_T &= \frac{X'_1(d-e) + X'_2(d+e)}{2d} \\ Y'_T &= \frac{Y'_1(d+e) + Y'_2(d-e)}{2d} \end{aligned} \tag{6.4}$$

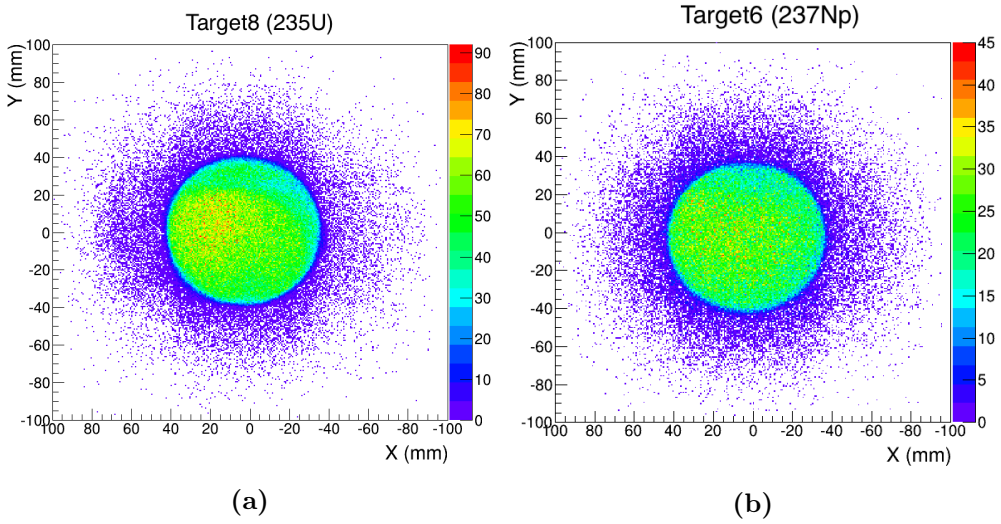

(a) **(b)**

Figure 6.7: Reconstructed emitting points on target8 (a) and target6 (b)

The distribution of the emitting points on target8 (^{235}U) and target6 (^{237}Np) reconstructed by equation 6.4 are shown in figure 6.7. We see clearly that the emitting points are concentrated in a circle with a diameter of 8 cm, this is exactly the size of the target. However, there are some reconstructed points beyond the target circle. They are due to the wrong localization in the high energy region where the counting rate is high.

The cosine of the polar angle θ' and the tangent of the azimuth angle ϕ' around $\vec{Z}'$ in the perpendicular frame can be calculated by equation 6.5:

$$\begin{aligned} \cos\theta\prime &= \frac{Z'_{2X} - Z'_{1X}}{\sqrt{(X'_2 - X'_1)^2 + (Y'_2 - Y'_1)^2 + (Z'_{2X} - Z'_{1X})^2}} \\ \tan\phi' &= \frac{Y'_2 - Y'_1}{X'_2 - X'_1} \end{aligned} \tag{6.5}$$

We are interested to know the fission angle θ and azimuth angle ϕ around the neutron beam axis since they are the relevant angles of FFAD. So we define a tilted frame ($\vec{X}$,

$\vec{Y}$, $\vec{Z}$) which is a 45° clockwise rotation about the Y'-axis of the perpendicular frame ($\vec{X}'$, $\vec{Y}'$, $\vec{Z}'$). In this tilted frame, the $\vec{Z}$ axis is the neutron beam axis. For a point with a coordinate (X', Y', Z') in the perpendicular frame, its coordinate (X, Y, Z) in 45° tilted frame can be transformed by the rotation matrix (equation 6.6):

$$\begin{bmatrix} X \\ Y \\ Z \end{bmatrix} = \begin{bmatrix} \cos 45° & 0 & \sin 45° \\ 0 & 1 & 0 \\ -\sin 45° & 0 & \cos 45° \end{bmatrix} \begin{bmatrix} X' \\ Y' \\ Z' \end{bmatrix} \tag{6.6}$$

from which we can obtain the coordinates of the hitting points in the tilted frame and calculate the physics angle $\cos\theta$ and ϕ by equation 6.7.

$$\begin{aligned} \cos\theta &= \frac{1}{\sqrt{2}}(-\sin\theta'\cos\phi' + \cos\theta') \\ \phi &= \arctan\left(\sqrt{2}\frac{\sin\theta'\sin\phi'}{\sin\theta'\cos\phi' + \cos\theta'}\right) \end{aligned} \tag{6.7}$$

and the reciprocal from (θ, ϕ) to (θ', ϕ') is:

$$\begin{aligned} \cos\theta' &= \frac{1}{\sqrt{2}}(\sin\theta\cos\phi + \cos\theta) \\ \phi' &= \arctan\left(\sqrt{2}\frac{\sin\theta\sin\phi}{\sin\theta\cos\phi - \cos\theta}\right) \end{aligned} \tag{6.8}$$

Equation 6.7 and 6.8 will be used in latter analysis for determining the efficiency and FFAD in next section.

6.4 Angular distribution

As discussed in section 5.7.1, the measured angular dependence in a given direction is the coupling of efficiency and FFAD. So based on the knowledge of one of them, we can deduce the other one. Tilted setup of PPACs is dedicated to decouple these two elements.

6.4.1 Characteristics of the tilted setup

Figure 7.1 shows the tilted setup. The blue curve stands for a fission trajectory with back-to-back emission. Z' axis is perpendicular to the detectors and targets. The angle between the fission trajectory and Z' is θ' which defines the efficiency, because the efficiency is determined by the travel distance of the fission fragment in target and dead

layers which is exclusively linked with $\cos\theta'$ (see the text in section 5.7.1). Z axis is the beam direction. Its angle with the fission trajectory is θ which defines the FFAD.

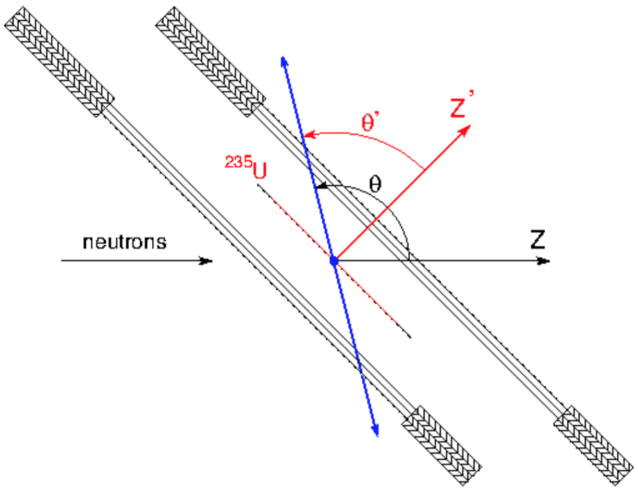

Figure 6.8: top view of a basic cell of tilted setup

For each fission event, with the tilted setup in figure 6.8, we have 2 polar angles θ' and θ which are defining efficiency and FFAD respectively. The same $\cos\theta'$ can be reached by different $\cos\theta$. Therefore as they have the same efficiency the distribution in $\cos\theta$ is the representative of the FFAD. So we obtain in this way different pieces of the FFAD from bins having the same efficiency. Conversely the same $\cos\theta$ can also be reached by different $\cos\theta'$ which represents the efficiency. So we get the efficiency dependence by pieces according to the given $\cos\theta$ intervals. This makes it possible to disentangle them because when one of them is fixed, we can deduce the other one based on the measured angular dependence.

Any given direction of fission can be defined by the couples ($\cos\theta'$, ϕ') or ($\cos\theta$, ϕ). It may also be defined with an interesting couple ($\cos\theta$, $\cos\theta'$) which is directly linked with the characteristics of tilted setup. Equations 6.7 and 6.8 show the relation between $\cos\theta$ and $\cos\theta'$. In equation 6.8, it can be seen that for a given $\cos\theta$ the range of possible $\cos\theta'$ is covered by varying ϕ in its full range [-π, π]. By using ±1 instead of $\cos\phi$ in equation 6.8, it gives the limits of the $\cos\theta'$ as a function of $\cos\theta$:

$$\cos\theta' = \frac{1}{\sqrt{2}}(\pm\sin\theta + \cos\theta) \tag{6.9}$$

which becomes as:

$$\cos^2\theta + \cos^2\theta' - \sqrt{2}\cos\theta\cos\theta' - \frac{1}{2} = 0 \tag{6.10}$$

Equation 6.10 is an ellipse tilted 45° in the ($\cos\theta$, $\cos\theta'$) plane as shown in figure 6.9 where the horizontal axis stands for the fission physics (FFAD) and vertical axis stands for the efficiency. All the measured ($\cos\theta$, $\cos\theta'$) counts should lie inside the curve as the hatched zone in figure.

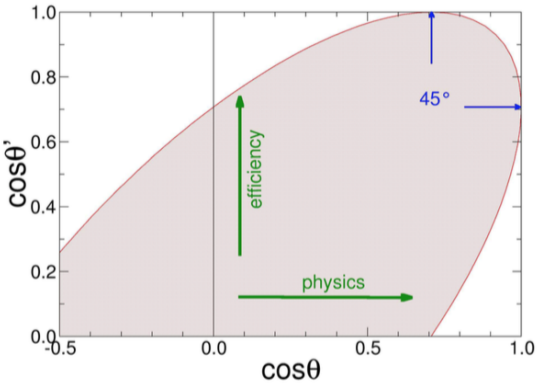

Figure 6.9: Ellipse curve from equation 6.10

The features of the ($\cos\theta$, $\cos\theta'$) plane in figure 6.9 are the following:

1) Any horizontal slice of height $\Delta\cos\theta'$ corresponds to a constant solid angle $\Delta\Omega = 2\pi\Delta\cos\theta'$ since it covers all the ϕ' in range $[-\pi, \pi]$.

2) For the same reason as 1) any vertical slice of width $\Delta\cos\theta$ corresponds to constant solid angle of $\Delta\Omega = 2\pi\Delta\cos\theta$.

3) Along a horizontal slice the efficiency is constant and the spectrum of counts in $\cos\theta$, for a given solid angle, reflects the angular distribution

4) Along a vertical slice the angular dependence is constant and the spectrum of counts in $\cos\theta'$ reflects the efficiency information

The number of fission events detected in any direction in ($\cos\theta$, $\cos\theta'$) map can be calculated by

$$\begin{aligned} dN &= CW(\cos\theta)\varepsilon(\cos\theta')d\Omega \\ &= CW(\cos\theta)\varepsilon(\cos\theta')d\cos\theta d\phi \\ &= CW(\cos\theta)\varepsilon(\cos\theta')d\cos\theta' d\phi' \end{aligned} \tag{6.11}$$

where C is a normalization constant factor including the neutron flux, cross section, target thickness and 4π solid angle, $W(\cos\theta)$ is the angular distribution which basically stands for the probability of the angular distribution whose integral on $\cos\theta$ is equal to 1, $\varepsilon(\cos\theta')$ is the detection efficiency which is only depending on $\cos\theta'$, $d\Omega$ is the differential solid angle which could be calculated either by $d\cos\theta d\phi$ or by $d\cos\theta' d\phi'$.

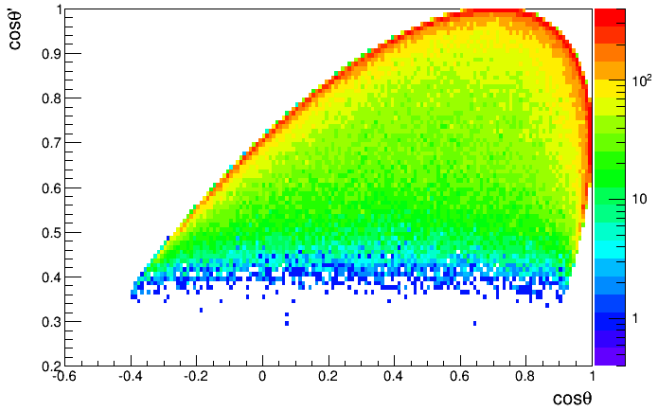

Figure 6.10: Distribution of counts in ($\cos\theta$, $\cos\theta'$) plane of ^{235}U target (target8) for E_n <100 keV

Figure 6.10 shows the ($\cos\theta$, $\cos\theta'$) distribution of ^{235}U target (target8) for neutrons below 100 keV where fission is isotropic. The elliptic shape is obvious but more counts are accumulated at the elliptic edge. For example, if we take a horizontal slice in figure 6.11a (figure 6.11a and figure 6.10 are exactly the same figure) and project it to $\cos\theta$ axis (figure 6.11b), we can see that more counts are present in the peripheral bins. This is because the peripheral bins take larger solid angles. The reason is the following: According to equation 6.11, the counts in each bin is

$$\Delta N = CW(\cos\theta)\varepsilon(\cos\theta')\Delta\Omega_{\cos\theta,\cos\theta'} \tag{6.12}$$

Since this is a horizontal slice, the efficiency is constant. And also as fission is isotropic in this energy region (E_n <100 keV), the $W(\cos\theta) = 1$. So the different bin counts are only from the solid angle.

We can directly calculate the solid angle of each bin by numerical integration using Gauss-Legendre method. Several points are taken in $\cos\theta'$ and for each of them the limits in ϕ' are computed for the horizontal limits in $\cos\theta$ by using equation 6.7. This gives

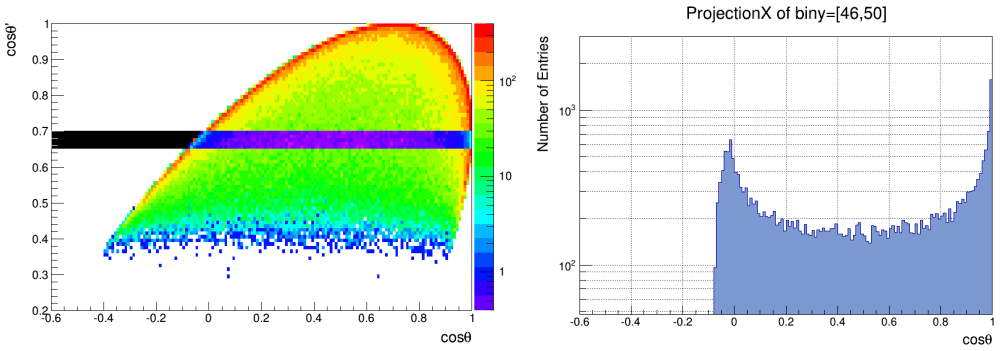

(a) (b)

Figure 6.11: (a)Distribution of counts in ($\cos\theta$, $\cos\theta'$) plane of ^{235}U target (target8) for $E_n < 100\ keV$; (b)Projection of the hatched slice in (a)

for each $\cos\theta'$ an interval $\Delta\phi'$ which is integrated over $\cos\theta'$. Figure 6.12 shows solid angle's variation of several horizontal slices. We can see that the solid angle increases quickly close to the lower and upper edge, which explains the shape in figure 6.11b.

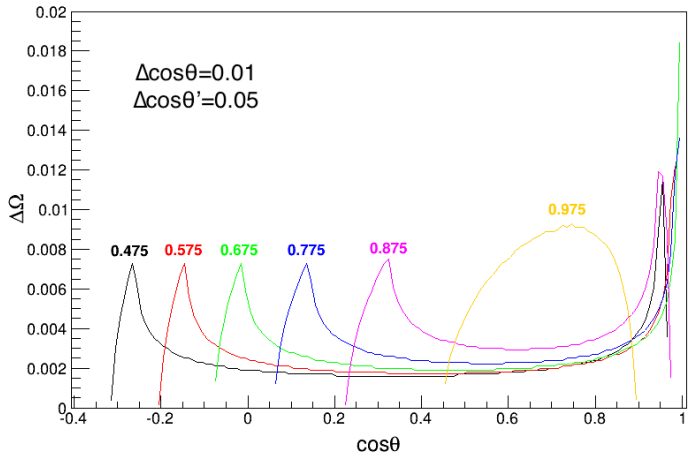

Figure 6.12: Solid angle of ($\cos\theta$, $\cos\theta'$) bins with a width $\Delta\cos\theta = 0.01$ and height $\Delta\cos\theta' = 0.05$. The numbers above each curve is the central value of $\cos\theta'$ of each horizontal slice

Based on the equation 6.12, we can obtain the product $W(\cos\theta)\varepsilon(\cos\theta')$ by dividing the counts in each bin by its solid angle:

$$W(\cos\theta)\varepsilon(\cos\theta') = \frac{\Delta N}{\Delta\Omega} \tag{6.13}$$

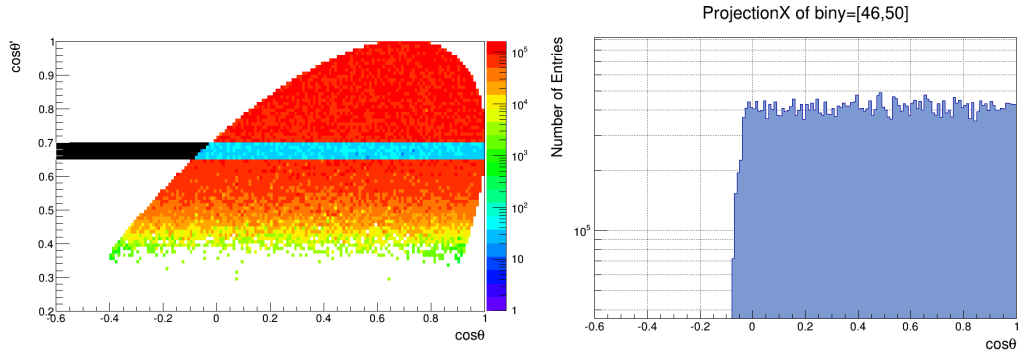

(a) (b)

Figure 6.13: (a)Distribution of counts divided by the solid angle for $E_n < 100\ keV$; (b)Projection of the hatched slice in (a)

Figure 6.13a shows the ($\cos\theta$, $\cos\theta'$) distribution of ^{235}U target (target8) for $E_n < 100\ keV$ where the counts in each bin have been divided by its solid angle. Figure 6.13b is the projection of hatched horizontal slice in Figure 6.13b. Now it's flat as expected since the solid angle of each bin has been taken into account and the angular distribution is isotropic in this energy region.

6.4.2 Correction of the geometric cut

Until now we assumed that the stopping of the fragments at large angles is the only constraint limiting the detection efficiency. However, there could be another constraint reducing the efficiency at some given direction ($\cos\theta'$, ϕ'): the geometrical cut due to the limited size of the active area of detectors. That is to say, some fission fragments are emitted out from the target successfully but land outside the active region of the detector.

This could happen for emission points at the edge of the target when the emission angles θ' regarding to Z' exceed a given threshold. Figure 6.14 illustrates the geometric cut effect on a top view of a basic cell. The detectors are always centered on the beam axis. δ is the shift of the target from the origin in X' axis. L is half length of the square active area, R is the radius of the circular target, d is the target-anode distance. θ'_{m1} and θ'_{m2} are the threshold angles for the emitting points at the edge of the target.

The efficiency loss caused by the geometric cut can be interpreted as a reduction of the visible target area in direction ($\cos\theta'$, ϕ') and it can be computed analytically. For

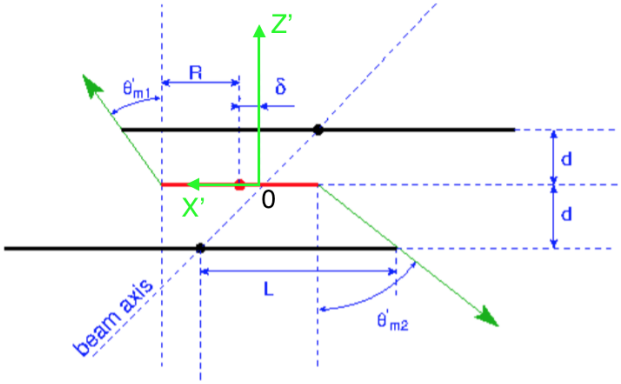

Figure 6.14: Illustration of geometric cut at a top view

a given direction $(\cos\theta', \phi')$ the geometric cut is equivalent to limit the visible area of the target as sketched in figure 6.15. The colored area is the available target area for a given fission direction, so the efficiency is the ratio of this area to the total area. The distances R_1 and R_2 depend on the fission direction and the geometrical parameters L, R, d and δ.

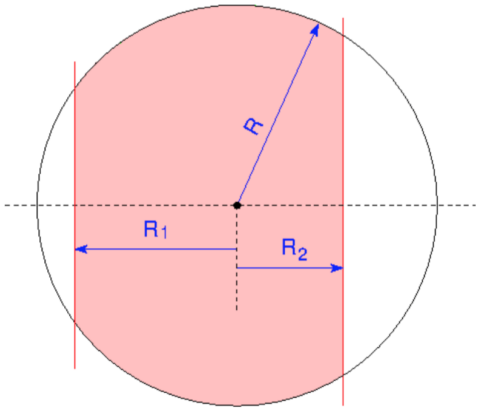

Figure 6.15: For a given emission direction $(\cos\theta', \phi')$ limitation of the possible emission points on the target due to limited detection area of the detectors.

We need to calculate the red area in figure 6.15 and obtain its fraction of the total area which will be the coefficient of the geometric limitation. The fraction is:

$$F(x_1, x_2) = \frac{g(x_1) + g(x_2)}{\pi} \tag{6.14}$$

where $x_1 = R_1/R$, $x_2 = R_2/R$, and

$$g(x) = \begin{cases} \arcsin(x) + x\sqrt{1-x^2}, & \text{if } x < 1 \\ \dfrac{\pi}{2}, & \text{if } x \geq 1 \end{cases} \tag{6.15}$$

From figure 6.14 we can obtain

$$\begin{aligned} \tan\theta'_{m1} &= \frac{L - d - R - \delta}{d} \\ \tan\theta'_{m2} &= \frac{L - d - R + \delta}{d} \end{aligned} \tag{6.16}$$

and for a given fission direction ($\cos\theta'$, ϕ'), we can obtain its x_1 and x_2 by equation 6.17:

$$\begin{aligned} x_1 &= \frac{L - d - \delta - d\tan\theta'\cos\phi'}{R} \\ x_2 &= \frac{L - d + \delta - d\tan\theta'\cos\phi'}{R} \end{aligned} \tag{6.17}$$

The geometric cut coefficient can be calculated by combining equation 6.14, 6.15 and 6.17. This coefficient is computed at the same time as the solid angle of each bin in the ($\cos\theta$, $\cos\theta'$) plane, so that the calculation returns the effective solid angle $\Delta\Omega'$ of each bin:

$$\Delta\Omega' = \Delta\Omega \times F \tag{6.18}$$

where F is defined by equation 6.14.

6.4.3 Determination of efficiency

In this section we present how we extract the efficiency based on the ($\cos\theta$, $\cos\theta'$) map as shown in figure 6.16. As already mentioned, the counts in each bin of the ($\cos\theta$, $\cos\theta'$) plane can be calculated by:

$$N_{ij} = CW(\cos\theta_j)\varepsilon_i\Delta\Omega'_{ij} \tag{6.19}$$

where N_{ij} is the counts in bin (i, j) for a broad energy range where we assume that the efficiency is constant, C is a normalization factor including the neutron flux, cross section, target quantity and 4π solid angle, $W(\cos\theta_j)$ is the angular distribution at j^{th} column averaged over the broad energy interval, ε_i is the efficiency at i^{th} horizontal line, $\Delta\Omega'_{ij}$ is the effective solid angle of bin (i, j). Since the counts in each bin cover a

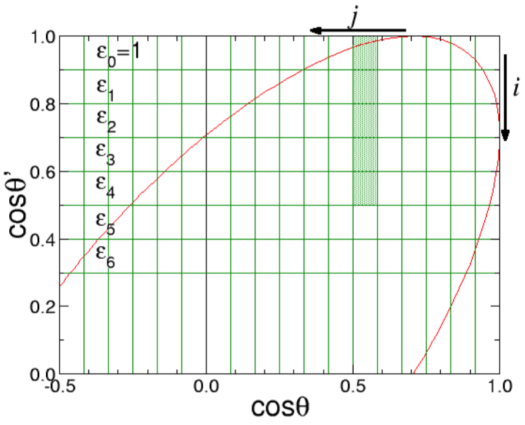

Figure 6.16: ($\cos\theta$, $\cos\theta'$) map with partitioned bins. - The bins in the same horizontal line have the same efficiency. The bins in the same column have the same angular dependence for a given energy. The horizontal lines are numbered with i, starting from top, and the columns are numbered with j starting from the right.

broad energy range, the average angular distribution is rather smooth and can be well approximated by a polynomial in $\cos\theta$ with terms of order 4:

$$W(\cos\theta) = (1 + \alpha_2 \cos^2\theta + \alpha_4 \cos^4\theta) \tag{6.20}$$

Based on equation 6.19 and 6.20 we can extract the efficiency ε_i in each horizontal line by a fit with the chi-square minimization method, where we define the chi-square as

$$\chi^2 = \sum_{i,j} [C(1 + \alpha_2 \cos^2\theta_j + \alpha_4 \cos^4\theta_j)\varepsilon_i \Delta\Omega'_{ij} - N_{ij}]^2 \tag{6.21}$$

with $\varepsilon_0 = 1$.

The fitted efficiency for ^{235}U and ^{237}Np in different neutron energy regions are shown in figure 6.17. The angular dependence is not very sensitive to the inducing neutron energy except in the high energy region (above 10 MeV), where the difference is obvious, which could come from mislocalization due to the high counting rate.

The fitted efficiencies from minimization of equation 6.21 are separated points, so the efficiency curve is not very smooth and there are some fluctuations. Instead of using them directly we use a Fermi-like function which can well reproduce the efficiency curve:

$$\varepsilon(\cos\theta') = \frac{1}{(1 + e^{a_1 - a_2 \cos\theta'})^{a_0}} \tag{6.22}$$

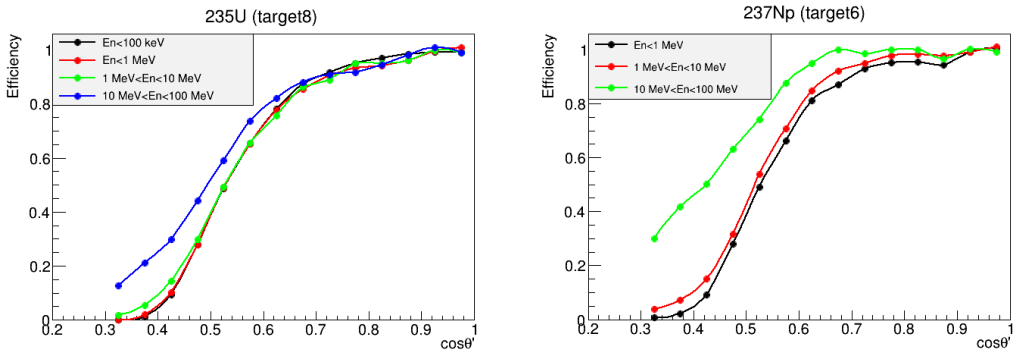

(a) **(b)**

Figure 6.17: Detection effiency as a function of $\cos\theta'$ for ^{235}U (a) and ^{237}Np (b) in different energy regions

with 3 parameters a_0, a_1 and a_2 to be fitted.

Figure 6.18 shows the efficiency curves fitted by equation 6.22 where the black dots are the efficiency points and the red line is the fit. We can see that function 6.22 is able to accurately reproduce the efficiency distribution. Therefore in the further analysis, we shall directly use this function to fit the efficiency curve to facilitate the analysis instead of fitting them slices by slices. That is to say, we define the chi-square as follow instead of equation 6.21.

$$\chi^2 = \sum_{i,j}[C(1+\alpha_2\cos^2\theta_j + \alpha_4\cos^4\theta_j)\cdot\frac{1}{(1+e^{a_1-a_2\cos\theta'_i})^{a_0}}\cdot\Delta\Omega'_{ij} - N_{ij}]^2 \qquad (6.23)$$

with 6 parameters (C, α_2, α_4, a_0, a_1, a_2) to be fitted.

6.4.4 Construction of FFAD

Once the efficiency has been determined, it is used to extract the angular distribution for any energy interval based on the characteristics of ($\cos\theta$, $\cos\theta'$) map. In figure 6.16, we know that horizontal slices are all proportional to the angular distribution: they are only scaled between each other by the product of the efficiency and solid angles corresponding to the bins. Therefore a point of the angular distribution can be obtained by summing up the counts on a column and summing up their respective weights (efficiency×solid

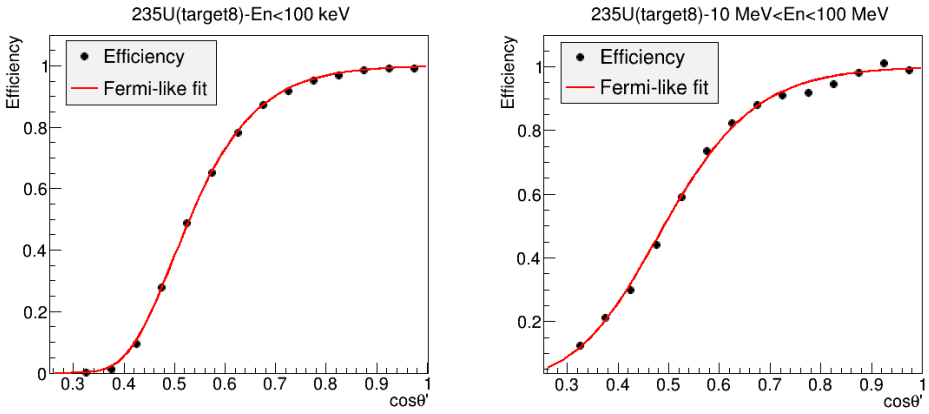

Figure 6.18: Comparison

angle) as:

$$W(\cos\theta_j) = K\frac{\sum_i N_{ij}}{\sum_i \varepsilon_i \Delta\Omega'_{ij}} \tag{6.24}$$

where K is a global normalization factor to fix the $W(\cos\theta)$ function.

It can be seen in figure 6.10 that the counts number below $\cos\theta' = 0.5$ are rather limited due to the low efficiency, so in the final results we will discard the events below $\cos\theta' = 0.5$ and extract angular distribution as follows.

For a given column j the sum of the counts is:

$$S_{1j} = \sum_{i,\cos\theta'>0.5} N_{ij} \tag{6.25}$$

The corresponding sum of effective solid angle and efficiency of above bins is:

$$S_{2j} = \sum_{i,\cos\theta'>0.5} \Delta\Omega' \times \varepsilon_i \tag{6.26}$$

where the efficiency ε_i is calculated by the Fermi-like function 6.22.

The angular distribution at this column is:

$$W(\cos\theta_j) = K\frac{S_{1j}}{S_{2j}} \tag{6.27}$$

The normalization factor K is defined based on the definition of $W(\cos\theta)$ because it can represent different quantities that are proportional to each other. For example, it can be normalized so that its integral is equal to 1 as in equation 6.11. It can be also normalized to 4π solid angle. Here we normalize the angular distribution at 90°

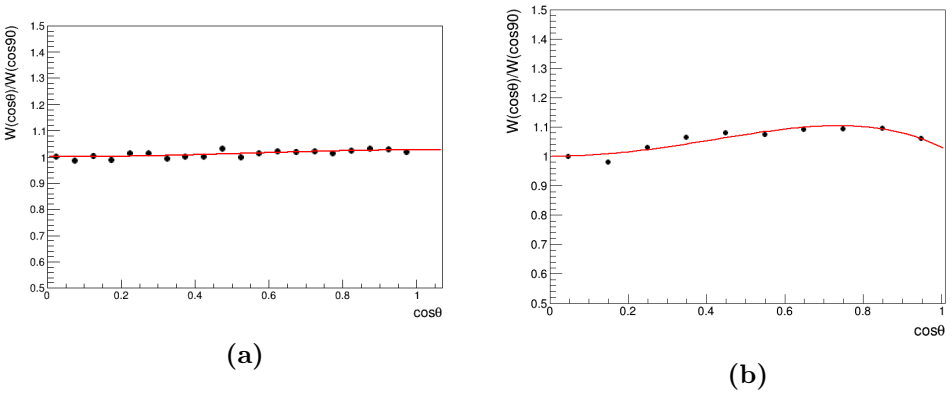

(a) **(b)**

Figure 6.19: FFAD of ^{235}U and ^{237}Np-(a)^{235}U for neutrons below 100 keV where the fission is isotropic; (b)^{237}Np for neutrons between 1 MeV and 2 MeV where the the fission is anisotropic.

to 1 ($W(\cos 90°) = W(0) = 1$), since it is convenient to obtain the anisotropy factor A which is defined as:

$$A = \frac{W(\cos 0°)}{W(\cos 90°)} \tag{6.28}$$

Figure 6.19 shows the FFAD obtained by the above procedure for 2 selected cases: ^{235}U at low energy (less than 100 keV) and ^{237}Np from 1 MeV to 2 MeV. Figure 6.19a is as flat as we expect since the fission of ^{235}U at low energy (less than 100 keV) is isotropic. For ^{237}Np above 1 MeV, the anisotropy of fission shows up and the fission fragments are preferentially emitted in forward direction due to the momentum transfer giving by incident neutrons, this is what we can see in figure 6.19b.

Chapter 7

Results and discussion

In this chapter, we will present the method to deduce the cross section. The first results of ^{237}Np neutron-induced fission cross section from fission threshold up to 5 MeV will be presented. The comparison between our results, the evaluation and some other experimental data will be shown and discussed.

7.1 Integral Efficiency determination

The approaches to extract the efficiency ($\varepsilon(\cos\theta')$) and FFAD ($W(\cos\theta)$) have been introduced respectively in details in section 6.4.3 and section 6.4.4. However, the probability to detect a fission at a given angle is the product of efficiency and FFAD, which will be referred as global efficiency in latter part. Here we show again the tilted setup (figure 7.1) to illustrate the following analysis.

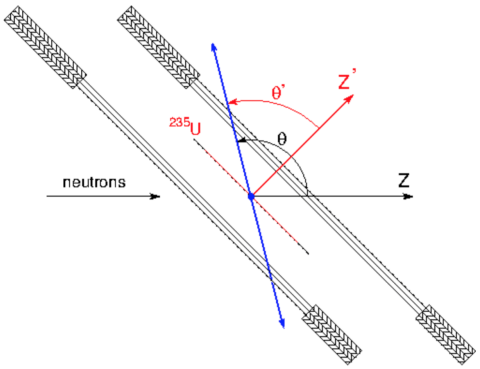

Figure 7.1: top view of a basic cell of tilted setup

The efficiency $\varepsilon(\cos\theta')$ we extracted in section 6.4.3 with respect to the Z' axis is a function of $\cos\theta'$. Figure 7.2 shows the efficiency of ^{237}Np (target6) as a function of $\cos\theta'$ for neutrons from 1 MeV to 5 MeV which is fitted by Fermi-like function (equation 6.22). It can be converted to the efficiency as a function of $\cos\theta$ which can facilitate the determination of global efficiency, because the FFAD is also a function of $\cos\theta$.

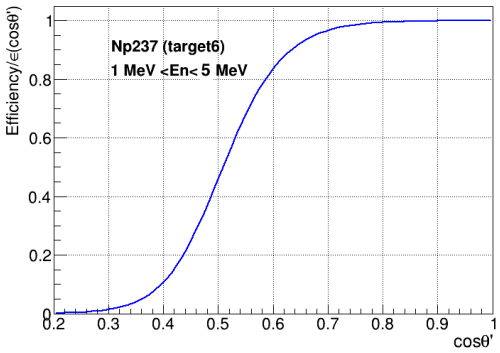

Figure 7.2: Efficiency of ^{237}Np target (target6) as a function of $\cos\theta'$ for neutrons from 1 MeV to 5 MeV

The efficiency $P(\cos\theta)$ corresponds to the integration of $\varepsilon(\cos\theta')$ on all the possible ϕ angles for this given $\cos\theta$,

$$P(\cos\theta) = \frac{1}{\pi}\int_0^{\pi} \varepsilon(\cos\theta')d\phi \tag{7.1}$$

where $\varepsilon(\cos\theta')$ has a distribution as shown in figure 7.2, and $\cos\theta'$ is given by equation 7.2.

$$\cos\theta' = \frac{1}{\sqrt{2}}(\sin\theta\cos\phi + \cos\theta) \tag{7.2}$$

According to equation 7.1 and equation 7.2 we can obtain the efficiency as a function of $\cos\theta$ as shown in figure 7.3. We can see that this kind of efficiency distribution permits us to cover all the angles from 0 to 90 degree, thus we can obtain the FFAD over the whole angular distribution. This is a strong advantage of tilted setup compared to perpendicular setup (figure 5.18). In the perpendicular setup, the fission fragments can not be detected in large angles because efficiency drops dramatically with the increase of the fission angle. At 90°, the detectors are physically not present, therefore the detection of fission fragments is simply impossible.

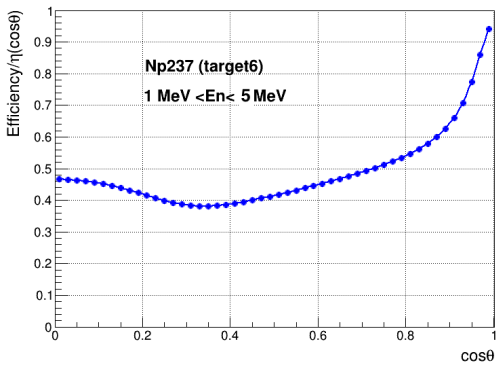

Figure 7.3: Efficiency of the tilted setup as a function of $\cos\theta$ - ^{237}Np target (target6) for neutrons from 1 to 5 MeV

As mentioned in section 6.4.3 FFAD can be well approximated by a polynomial in $\cos\theta$ with terms of order 4:

$$W(\cos\theta) = (1 + \alpha_2 \cos^2\theta + \alpha_4 \cos^4\theta) \tag{7.3}$$

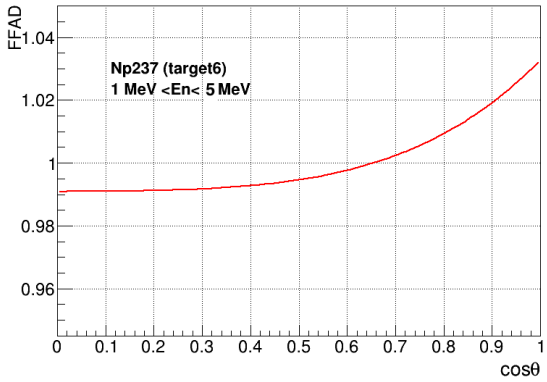

Figure 7.4: Fitted FFAD of ^{237}Np (target6) for neutrons from 1 to 5 MeV.

Figure 7.4 is the angular distribution of ^{237}Np (target6) fitted by equation 6.21 for neutrons from 1 MeV to 5 MeV. We apply it to the efficiency curve (figure 7.3) and make the integration of their product by equation 7.4, in order to obtain the global efficiency η which will be used for calculating the cross section.

$$\eta = \int_0^1 W(\cos\theta) P(\cos\theta) d(\cos\theta) \tag{7.4}$$

The efficiencies as a function of $\cos\theta'$ of 3 ^{237}Np targets and reference ^{235}U target (target8) from 1 MeV to 5 MeV are shown in figure 7.5. In this energy range, the effect of the anisotropy of FFAD on the global efficiency is rather small, because the FFAD is quite flat before the second chance fission. It can be simply checked by taking different anisotropy parameters and FFAD functions. We take 2 different FFAD functions, polynomial with order 2 and order 4, to calculate the global efficiency of ^{237}Np (target6) and ^{235}U (target8) with different anisotropy parameters. It can be seen from figure 7.6 that the global efficiency is increasing with the increase of the anisotropy, and the increasing slope depends on the form of FFAD. However the anisotropy correction on the global efficiency is rather tiny. The maximum anisotropy of ^{235}U is expected to be around 1.3 at the level of second chance fission, which induces a variation of global efficiency of less than 2%. We will only take into account energy range from 1 MeV to 5 MeV which is even before the second chance fission, so the effect is even less than 1%.

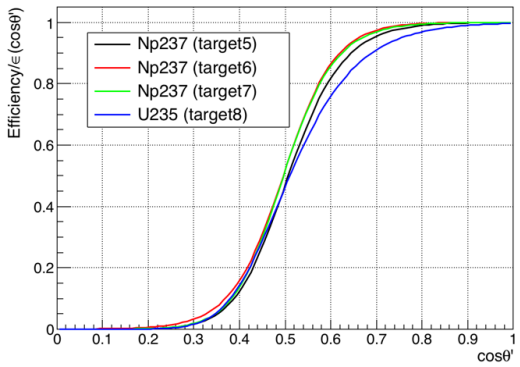

Figure 7.5: Efficiency of 3 ^{237}Np targets and reference ^{235}U target from 1 MeV to 5 MeV

If we consider the FFAD is isotropic, then the global efficiency is simply the integral of the curves in figure 7.5. Table 7.1 lists the global efficiency of targets in case of isotropic and anisotropic respectively. For anisotropy correction we use the average FFAD between 1 to 5 MeV fitted from our data. The global efficiencies in table 7.1 will be used to calculate the cross section in later part.

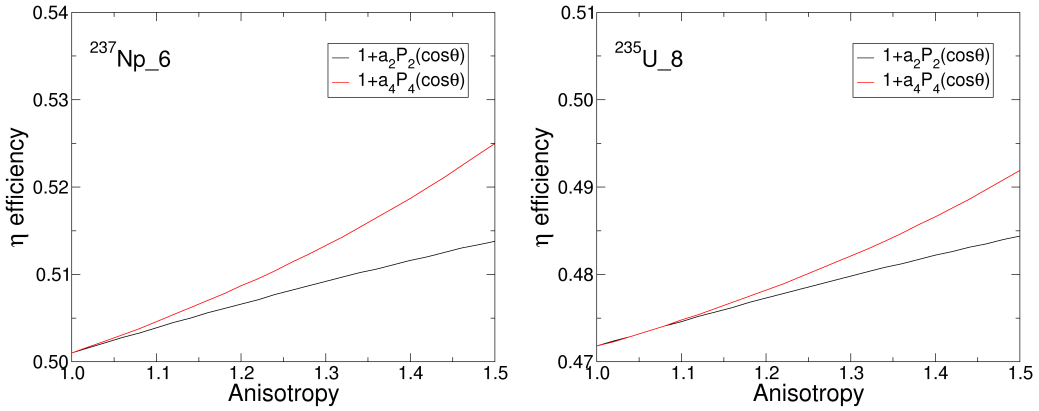

(a) ^{237}Np target (target6) **(b)** ^{235}U target (target8)

Figure 7.6: Distribution of the global efficiency versus the anisotropy

Target	mass	Global efficiency	
	mg	Isotropic	Anisotropic
^{237}Np (target5)	16.1	0.487	0.488
^{237}Np (target6)	15.4	0.502	0.503
^{237}Np (target7)	16.1	0.499	0.5
^{235}U (target8)	14.0	0.475	0.475

Table 7.1: The global efficiency in case of isotropic and anisotropic FFAD of different targets

7.2 Neutron-induced fission cross section of ^{237}Np from 1 MeV to 5 MeV

The neutron-induced fission cross section σ is:

$$\sigma(E_n) = \frac{R(E_n)}{\Phi(E_n)\eta(E_n)N} \tag{7.5}$$

where in our case

- E_n is neutron energy,
- R is the fission rate,
- Φ is the integral neutron flux on the target,

- N is the target thickness (atoms/cm^2) that has been measured by α counting,
- η is the global efficiency including the anisotropy correction for FFAD.

In the experiment, the integral neutron flux for all the targets is the same because the material quantity in the beam is so tiny that the attenuation of the flux is negligible. Therefore according to equation 7.5 we can obtain the cross section ratio of ^{237}Np over ^{235}U by

$$\frac{\sigma_7(E_n)}{\sigma_5(E_n)} = \frac{R_7(E_n)}{R_5(E_n)} \times \frac{\eta_5(E_n)}{\eta_7(E_n)} \times \frac{N_5}{N_7} \tag{7.6}$$

where 7 stands for the ^{237}Np and 5 stands for the ^{235}U.

The analysis method to select the fission event and extract the fission rate have been presented in details in section 5.3, section 5.4 and section 6.2. The procedures to extract the efficiency and make the anisotropy correction to obtain the global efficiency have been presented respectively in section 6.4.3 and section 7.1. It should be noticed that in our method, the efficiency can only be obtained when the cathode localization signals are present besides the anode signal. Therefore the efficiency we extracted according to the previous description is the efficiency with localization. It is different if the localization signals are not considered and only anode signals are requested. A discussion will be dedicated in next section.

7.3 Anode versus localization application

7.3.1 Consistency of the fission rate

In this thesis work, we analyzed 3 ^{237}Np targets (target 5, 6, 7 in figure 6.1) and a ^{235}U target (target 8 in figure 6.1) as reference. Before using the fission rate to calculate the cross section, it is very important to check the consistency of the fission rates from different targets because it checks the reliability of the data. The consistency can be checked by comparing the normalized fission rates of different targets, which is calculated by

$$R_{nor}(E_n) = \frac{R(E_n)}{m \times \eta} \tag{7.7}$$

where $R_{nor}(E_n)$ is the normalized fission rate, $R(E_n)$ is the measured fission rate, m is the target mass, η is the global efficiency.

The normalized fission rates should be identical, since they take into account all the factors involved in the relative fission rate. Due to the unavoidable systematic uncertainty, there should be some dispersion between different normalized fission rate, but the dispersion is expected to be very small, around 2-3%. The dispersion can be calculated by dividing each normalized fission rate by the average of them which is defined as:

$$< R_{nor}(E_n) >= \frac{R_5(E_n) + R_6(E_n) + R_7(E_n)}{m_5\eta_5 + m_6\eta_6 + m_7\eta_7} \tag{7.8}$$

where 5, 6, 7 stand for the target 5, 6, 7 respectively.

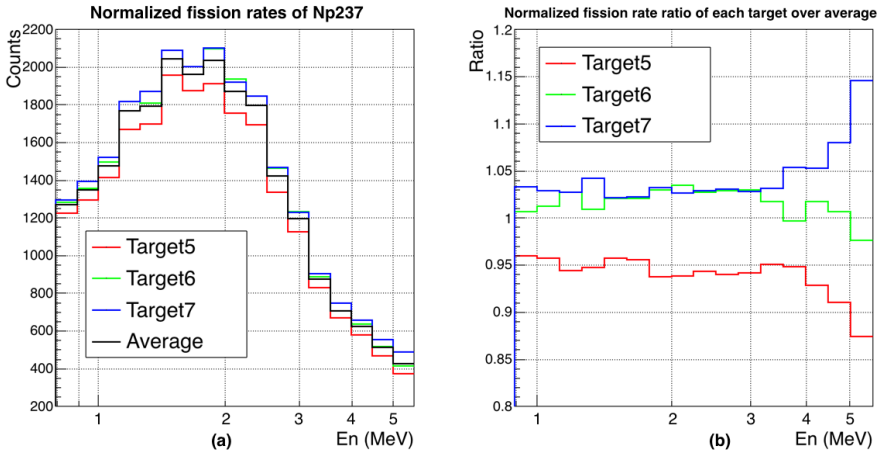

Figure 7.7: Comparison of normalized fission rate of 3 ^{237}Np targets. The left figure is the comparison of the 3 normalized fission rates. The right figure presents the ratios of each fission rate divided by the average fission rate.

The comparison of the normalized fission rates of 3 ^{237}Np targets is shown in figure 7.7 (a). Figure (b) shows their dispersion. We can see the fission rates are not well consistent since the discrepancy almost reaches 10% at 5 MeV. With this bad consistency, these fission rates are not reliable, hence we can not use them to deduce the fission cross section. This discrepancy is caused by the pile up effect of the cathode localization signals leading to a loss of fission events when the localization is requested. Because the cathode signals are wider than anode. This pile up is energy dependent (counting rate dependent) but it does not distort the angular dependencies we have extracted up to now. As an alternative for the cross section determination, we can consider only the anode signals without localization. This is developed in next subsection.

7.3.2 Relation between anode and cathode signal

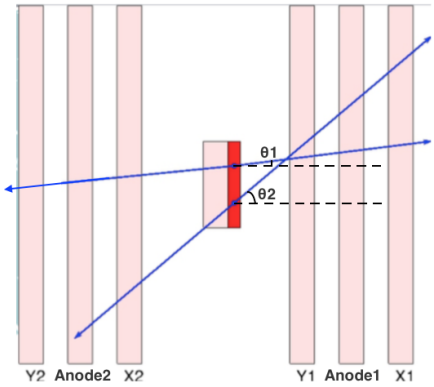

Figure 7.8: Detection of fission by PPACs

Figure 7.8 illustrates the detection principle of a fission event by a pair of PPACs. A PPAC consists of a central anode and 2 surrounding cathodes. The anode is used to measure the time and to perform the coincidence to identify fission, the 2 cathodes are used to locate the fission fragment in X and Y direction. It can be seen from figure 7.8 that an anode signal will appear as soon as a fission fragment traverses the first cathode facing the target. This anode signal can be immediately used to perform the coincidence requirement to identify the fission. However, the localization of this fission fragment requires the fission fragment to go through the anode, otherwise the second cathode signal will be missing and the reconstruction of the fission trajectory cannot be achieved. It means when we need the localization information, we need both cathodes deliver signals. Therefore the efficiency for events detected in the anode is higher than those whose localization signals are present, because some fission fragments may stop in the anode. In this case the anode signal is present and could be counted as a fission event, but if the localization is requested this event has to be discarded due to the lack of the localization information.

Now let's look at the relation between fission rate with localization requirement and without localization (only anode coincidence is applied regardless of cathode signal). The (a), (b), (c) in figure 7.9 and (a) in figure 7.10 shows the fission rate of 3 ^{237}Np targets and the ^{235}U target. The red curves are the fission events determined only by anode coincidence without localization, the black ones are the fission events acquired by anode coincidence with supplementary localization requirement. We can see that

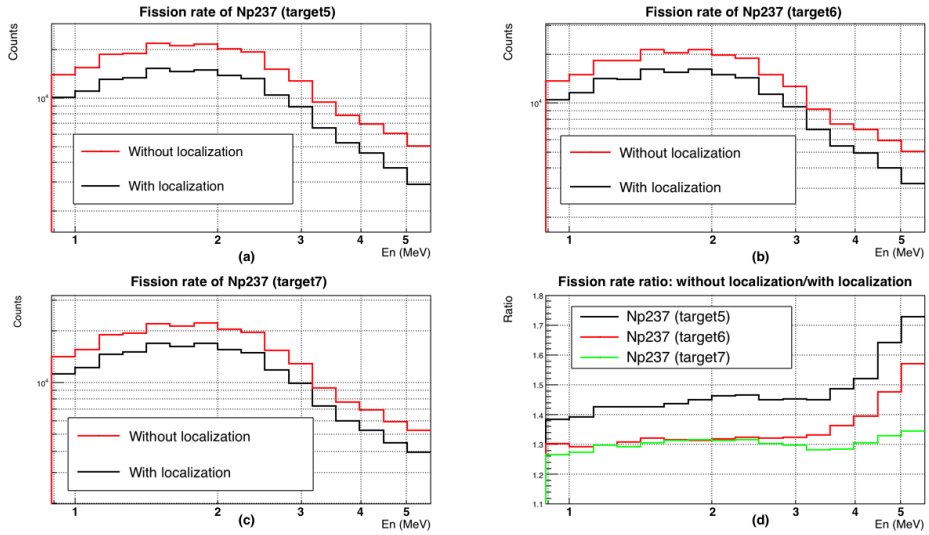

Figure 7.9: Fission rates of ^{237}Np targets. (a), (b) and (c) are the fission rates of 3 ^{237}Np targets with and without the localization; (d) is the the ratios without localization over with localization.

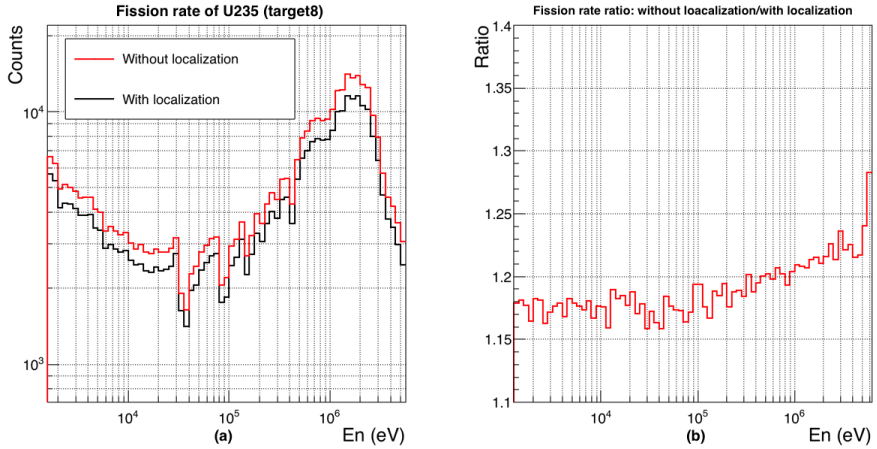

Figure 7.10: Fission rates of ^{235}U targets. (a) presents the fission rates of ^{235}U target with and without the localization; (d) presents the their ratio without localization over with localization.

the counting with localization scales down respect to the anode signals, meaning that the corresponding efficiency is lower as we expect. However, from figure 7.9 (d) and figure 7.10 (b), we see that the ratios are not constant along the energy. This is the effect of the pile up of cathode signals. Since cathode signals are wider than the anode

signal, with the increase of the neutron energy, more pile ups show up which really affect the identification of the cathode signal, hence it affects the fission rate with localization.

However, the pile up does not affect the measured angular dependencies and angular efficiency since pile up is not depending on angle or localization but is only changing with energy. Figure 7.11 shows the efficiency of Np target in different energy range. We can see that the angular dependence is still consistent from 1 to 6 MeV as expected, therefore our method to determine the efficiency and FFAD is still reliable.

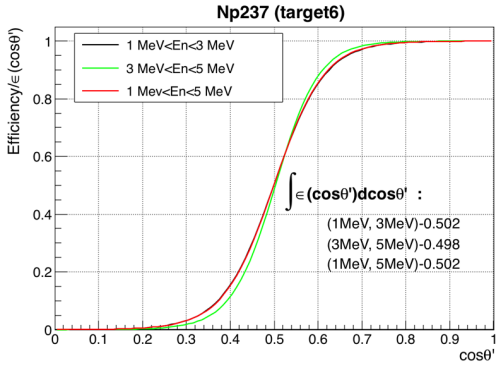

Figure 7.11: Effciency of ^{237}Np (target6) in 3 different energy range

Based on the above discussion we see the fission rate with the localization requirement is affected by the pile up and is not reliable. Now we have to rely on the fission rate without localization to deduce the cross section. First important thing is still to check their consistency with the normalized fission rates. In our PPAC measurement, we only know the efficiency with the localization, but the efficiency related to the anode signals only is not definitely known since it's impossible to directly reconstruct it without the localization information. Therefore here we assume temporarily that the efficiency without localization is the same for the three ^{237}Np target and we normalize the fission rate only by the mass:

$$R_{nor}(E_n) = \frac{R(E_n)}{m} \tag{7.9}$$

and define their average as

$$< R_{nor}(E_n) >= \frac{R_5(E_n) + R_6(E_n) + R_7(E_n)}{m_5 + m_6 + m_7} \tag{7.10}$$

The left part of figure 7.12 shows the comparison of the normalized fission rate by taking only anode signals. The right figure shows their dispersion. We can see that the

anode coincidences without localization lead to distributions more consistent between each other. They are dispersed within ±3% discrepancy, resulting from the systematic uncertainty. This indicates that these fission rates without localization are more reliable and can be used to deduce the cross section.

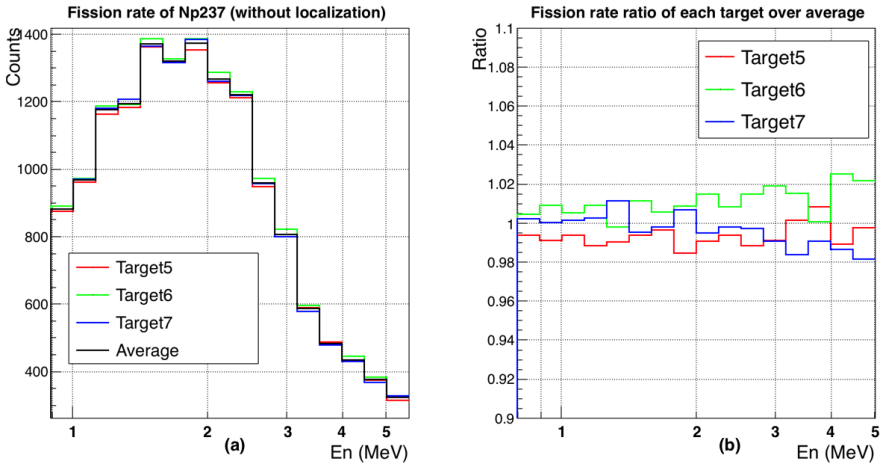

Figure 7.12: Comparison of normalized fission rate of 3 ^{237}Np targets without localization. The left figure is the comparison of the 3 normalized fission rates without localization. The right figure presents the ratios of each fission rate divided by the average fission rate.

7.3.3 Efficiency of the fission rate without localization

The reliability of the fission rate without localization has been checked. Apart from it, to deduce the cross section we also need to know the efficiency ratio of ^{235}U and ^{237}Np target. However, we don't know the efficiency of anode coincidence, we only know the angular dependence when the localization is involved. Here we assume that the efficiency without the localization is defined by the same angular dependence as the one with localization. This hypothesis can be checked if we use the efficiency from localization to normalize the fission rate without localization. We use equation 7.7 and 7.8 to normalize the anode fission rate. Figure 7.13 shows the consistency of the fission rate treated in this way, it can bee seen that they are dispersed within ±3%, which is favoring our assumption. Therefore, we will use the efficiency ratio with localization to estimate the efficiency ratio without localization to calculate the cross section.

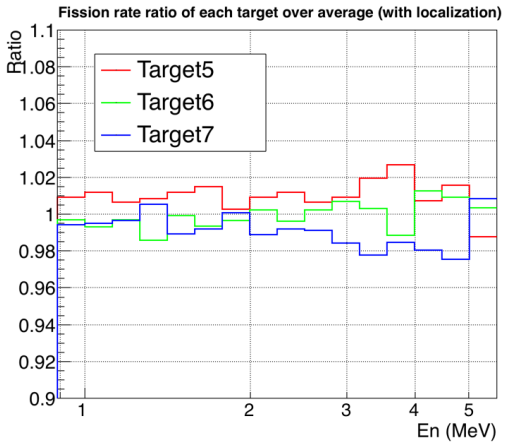

Figure 7.13: Dispersion of the fission rate without localization - The fission rate is obtained without localization but is normalized by the localization efficiency

7.4 Cross section and discussion

We use the normalized fission rate to deduce the fission cross section ratio of ^{237}Np relative to ^{235}U by

$$\frac{\sigma_7(E_n)}{\sigma_5(E_n)} = \frac{< R_{nor7}(E_n) >}{R_{nor5}(E_n)} \times C \tag{7.11}$$

where $< R_{nor7}(E_n) >$ is the average of the normalized fission rates of 3 ^{237}Np targets, which is calculated by equation 7.8 with the efficiency listed in table 7.1, $R_{nor5}(E_n)$ is the normalized fission rates of ^{235}U calculated by equation 7.7 with its efficiency, C is a correction constant taking into account the different mass number of ^{237}Np and ^{235}U, namely 237/235.

Figure 7.14 is the comparison of the neutron-induced fission cross section ratio of ^{237}Np relative to ^{235}U. We can see that our result is about 3-4% higher than the ENDF-B/VII.0 evaluation above 1 MeV. We also find that our data are about 2.2% lower compared with our previous measurement in 2010 [6]. This difference is mainly from the efficiency. In our previous measurement, since PPAC is perpendicular to the beam, we can not extract its efficiency as we've done in this work. Therefore it was assumed that the efficiency is the same for all the targets. In this work, we obtained the efficiency for different targets thanks to the tilted setup. We find that the efficiency of same targets (same original source, same backing, same thickness) is quite similar, for example target 5 and 7, as we expected before. However, differences exist for different actinide targets.

For example, the efficiency of ^{235}U target (target8) is 4.4% lower than the average efficiency of 3 ^{237}Np targets. As a consequence of taking into account this factor in this work, our measured cross section tend to be lower than previous one.

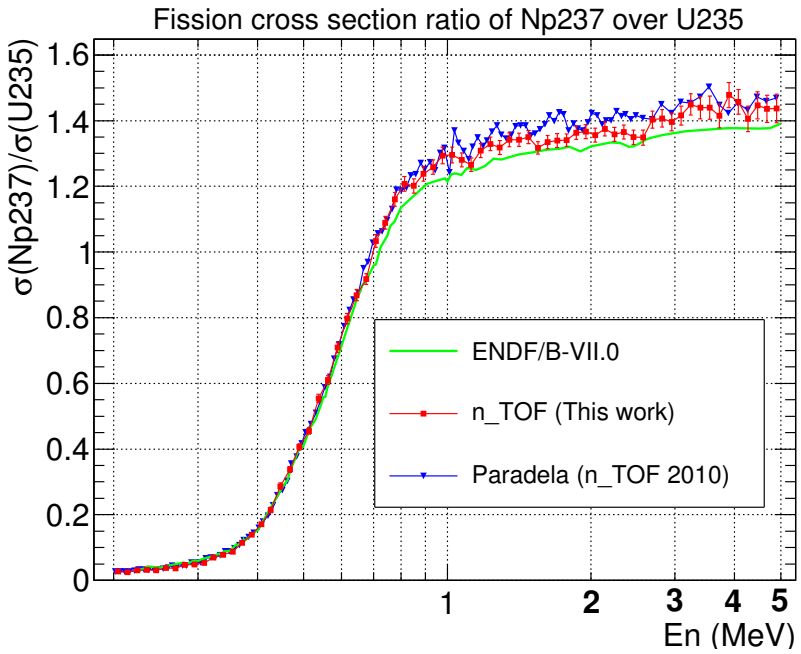

Figure 7.14: The neutron-induced fission cross section ratio of ^{237}Np relative to ^{235}U from 1 to 5 MeV. - The results of this work are compared to the ENDF/B-VII.0 evaluation and our previous measurement data [6]. The error bars of the present data in this work only stands for the statistical uncertainties.

Figure 7.15 is the comparison of the neutron-induced fission cross sections of ^{237}Np. Our results are obtained by multiplying the ENDF/B-VII.0 fission cross secion of ^{235}U to the ratio in figure 7.14. It is compared with the evaluation and some experimental data. It can be seen that our data can well reproduce the shape of the ENDF/B-VII.0 evaluation. However, it is slightly, about 3-4%, higher than the evaluation above 1 MeV. The two black circle points are the measurement by Diakaki et al [57]. Their result at 4.58 MeV is consistent with our result, whereas their data at 4.85 MeV is identical to the evaluation.

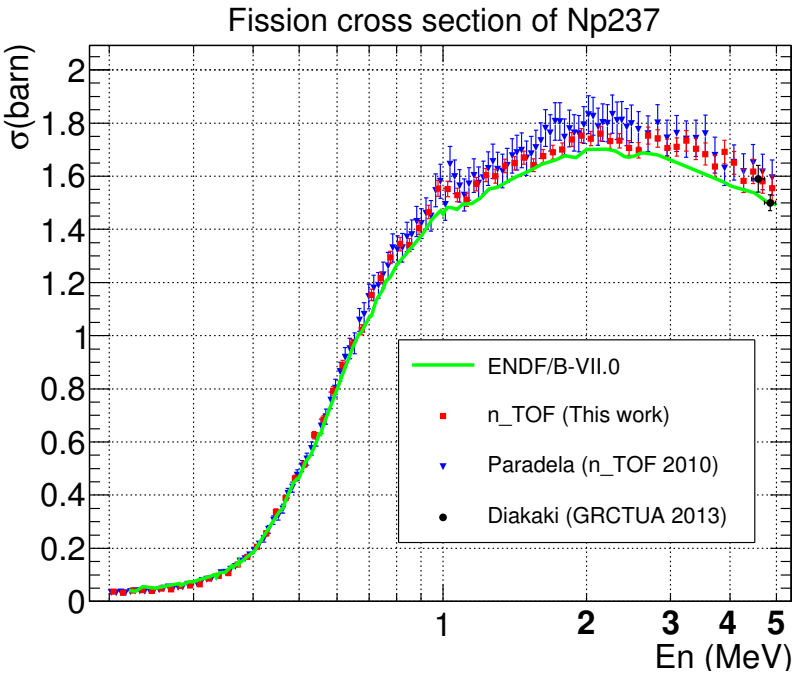

Figure 7.15: The neutron-induced fission cross section of ^{237}Np from 1 to 5 MeV - The results of this work are compared to the ENDF/B-VII.0 evaluation and some experimental data [6, 57]. The error bars of the present data in this work only stands for the statistical uncertainties.

Chapter 8

Conclusions and outlook

8.1 Conclusions

- EAR-2 beam measurement

We present the first PPACmon experiment, done at n_TOF EAR-2, for characterizing the beam profile and neutron flux at this new facility. The obtained neutron beam profile shows that the beam intensity is much lower in the peripheral region, forming a halo around the central intense part. This is different with the beam profile at EAR-1 which is quasi-uniform. This beam profile feature of EAR-2 is caused by the collimator located before the experimental hall, which has a conical design for the inner hole [41]. The measured beam profile could be a reference for the future experiment design and analysis.

The TOF, fission rate and unnormalized flux spectra at EAR-2 are obtained by PPACmon, finally contributing to the flux evaluation. From the fission rate we can see that PPACmon is able to monitor the neutrons from thermal energy up to 200 MeV, which makes it the detection system covering the largest energy range at n_TOF . Especially, PPACmon is the only one that can provide data for the high energy region, from a few MeV to 200 MeV, due to its fast signal and reliable method to identify the fission event.

- ^{237}Np(n, f) measurement

The experiment at n_TOF EAR-1 for studying the neutron induced fission of ^{237}Np is presented. The experimental and analysis methods for extracting the FFAD and

deducing the fission cross section are described. The fission rates of ^{237}Np and the reference ^{235}U as a function of neutron energy are obtained. The first results of ^{237}Np neutron-induced fission cross section until 5 MeV are obtained relative to ^{235}U, using the ENDF/B-VII.0 evaluation as a reference.

In this experiment, the target quantities of ^{237}Np and ^{235}U are well-known since they were measured in a well-defined geometric system with an uncertainty less than 1%. The efficiency with cathode localization is obtained and the anisotropy of FFAD are corrected to obtain the global efficiency from 1 MeV and 5 MeV. Based on the hypothesis that the efficiency without localization is proportional to the efficiency with localization, we obtained the cross section ratio of ^{237}Np over ^{235}U from the fission rate solely from the anode coincidence and the efficiency ratio with localization. A first results of fission cross section ratio of ^{237}Np relative to ^{235}U from threshold up to 5 MeV are presented. The results are about 3-4% higher than the ENDF/B-VII.0 evaluation, and 2-3% lower than our previous measurement in 2010.

8.2 Outlook

For the beam measurement at EAR-2, since the prompt γ-flash sharp peak is not visible for PPACmon, we used the first fission event and a simulated neutron flux to determine the T_0. Another option is to use the fission threshold of some isotopes to determine the T_0. We have done another experiment with PPACmon at EAR-2 with one ^{235}U and one ^{238}U target, intending to use the fission threshold of ^{238}U around 1 MeV as a reference to deduce the T_0.

Concerning the ^{237}Np(n, f) measurement, this thesis gives the first results. There are some analysis left to be done to complete the work.

1. As mentioned in chapter 6 and 7, the pile up of the cathode signal not only brings some mislocalizations, but also generates some difficulties to use the fission rate with localization. Besides, we also found some other issues in the raw data, for example, high frequency oscillation occurs sometimes. Fortunately, these issues can be solved by a more sophisticated routine dedicated to PPAC. It needs a full long reprocessing of the raw data. This is foreseen to be done in the near future.

2. As long as the raw data are treated by the PPAC dedicated routine, with the expected improvement of localization and sufficient statistics, we can extract the FFAD

in high energy region. Therefore we expect to obtain the FFAD and neutron-induced fission cross section of ^{237}Np up to hundreds of MeV.

3. In this thesis, we presented the results of three ^{237}Np targets (target 5, 6 and 7) and one ^{235}U target (target 8). The remaining targets will be analyzed in the future, especially the two ^{237}Np targets (target 2 and 3). They will be compared with the three ^{237}Np targets and the consistency of the cross section will be checked.

References

[1] J. Chadwick. **Possible existence of a neutron**. *Nature*, **129**:312, 1932.

[2] E. Fermi. **Possible production of elements of atomic number higher than 92**. *Nature*, **133**:898–899, 1934.

[3] O. Hahn and F. Strassmann. **Über den nachweis und das verhalten der bei der bestrahlung des urans mittels neutronen entstehenden erdalkalimetalle**. *Naturwissenschaften*, **27**:11, 1939.

[4] L. Meitner and O. R. Frisch. **Disintegration of uranium by neutrons: a new type of nuclear reaction**. *Nature*, **143**:239–240, 1939.

[5] June 2017. `http://www.world-nuclear.org/information-library/current-and-future-generation/nuclear-power-in-the-world-today.aspx`.

[6] C. Paradela et al. **Neutron-induced fission cross section of ^{234}U and ^{237}Np measured at the cern Neutron Time-of-Flight (n_TOF) facility**. *Physical Review C*, **82**:034601, 2010.

[7] I. Garlea et al. **Integral neutron cross sections measured around 14 MeV**. *Romanian Journal of Physics*, **37**:19–25, 1992.

[8] J. W. Meadows. **The fission cross section of ^{230}Th, ^{232}Th, ^{233}U, ^{234}U, ^{236}U, ^{238}U, ^{237}Np, ^{239}Pu and ^{242}Pu relative to ^{235}U at 14.74 MeV neutron energy**. *Annals of Nuclear Energy*, **15**:421, 1988.

[9] K. Merla et al. **Absolute measurements of neutron induced fission cross-sections of ^{235}U, ^{238}U, ^{237}Np and ^{239}Pu using the time correlated associated particle method (TCAPM)**. In *Nuclear data for science and technology*, 1992.

[10] R. Jiacoletti et al. **Fission cross sections of Neptunium-237 from 20 eV to 7 MeV determied from a nuclear-explosive experiment**. *Nuclear Science and Engineering*, **48**:412–419, 1972.

[11] F. Tovesson and T. S. Hill. **Neutron induced fission cross sections of ^{237}Np from 100 keV to 200 MeV**. *Physical Review C*, **75**:034610, 2007.

[12] O. Shcherbakov et al. **Neutron-induced fission cross section of ^{233}U, ^{238}U, ^{232}Th, ^{239}Pu, ^{237}Np, ^{nat}Pb and ^{209}Bi relative to ^{235}U in the energy range range 1-200 MeV**. *Journal of Nuclear Science and Technology*, **Supp. 2**:230–233, 2002.

[13] R. Sanchez et al. **Criticality of a ^{237}Np sphere**. *Nuclear Science and Engineering*, **158**:1–14, 2008.

[14] L. S. Leong et al. **Criticality experiments for validation of cross sections: The neptunium case**. *Annals of Nuclear Energy*, **54**:36–42, 2013.

[15] P. Salvador-Casti nira et al. **Neutron-induced fission cross section of ^{240,242}Pu up to $\mathbf{E}_n$ = 3 MeV**. *Nuclear Data Sheets*, **119**:55–57, 2014.

[16] P. Salvador-Casti nira et al. **Neutron-induced fission cross section of ^{240,242}Pu**. *Physics Procedia*, **64**:177–182, 2015.

[17] E. Chiaveri. **Proposal for n_TOF experimental area 2**. Technical Report CERN-INTC-2012-029, CERN, 2012.

[18] F. Gunsing et al. **Nuclear data measurements at the upgraded neutron time-of-flight facility n_TOF at CERN**. In *14th International Conference on Nuclear Reaction Mechanisms*, jan 2015.

[19] A. Bracco et al. *Perspectives of nuclear physics in Europe: NuPECC long range plan 2010*. European Science Foundation, 2010.

[20] G. Gamow. **Mass defect curve and nuclear constitution**. *Proceedings of the Royal Society of London. Series A, Containing Papers of a Mathematical and Physical Character*, **803**:632–644, 1930.

[21] C. F. V. Weizsäcker. **Zur theorie der kernmassen**. *Zeitschrift für Physik A Hadrons and Nuclei*, **96**:431–458, 1935.

[22] J. W. Rohlf. *Modern Physics from alpha to Z0*. Wiley, 1994.

[23] N. Bohr and J. A. Wheeler. **The mechanism of nuclear fission**. *Physical Review*, **56**:426–450, 1939.

[24] S. Cohen and W.J. Swiatecki. **The deformation energy of a charged drop: Part v: Results of electronic computer studies**. *Annals of Physics*, **22**:406–437, 1963.

[25] R. Vandenbosch and J.R. Huizenga. *Nuclear Fission*. Academic Press, 1973.

[26] M.G. Mayer. **On closed shells in nuclei**. *Physical Review*, **74**:235, 1948.

[27] O. Haxel et al. **On the "magic numbers" in nuclear structure**. *Physical Review*, **75**:1766, 1949.

[28] M.G. Mayer. **Nuclear configurations in the spin-orbit coupling model. i. empirical evidence**. *Physical Review*, **78**:16, 1950.

[29] May 2017. `hyperphysics.phy-astr.gsu.edu/hbase/Nuclear/shell.html`.

[30] S. G. Nilsson. **Binding states of individual nucleons in strongly deformed nuclei**. *Danske Videnskab. Selskab., Mat.-fys Medd.*, **29**:1–16, 1955.

[31] C. Wagemans. *The nuclear fission process*. CRC press, 1991.

[32] K. H. Schmidt et al. **General description of fission observables: GEF model code**. *Nuclear Data Sheets*, **131**:107–221, 2016.

[33] K. H. Schmidt et al. **General description of fission observables-JEFF Report 24. GEF Model**. Technical Report NEA-DB-DOC-2014-1, Organisation for Economic Co-operation and Development, 2014.

[34] J. E. Brolley et al. **Angular dependence of the neutron-induced fission process. II**. *Physical Review*, **99**:159–165, 1955.

[35] R. L. Henkel et al. **Angular distribution of fragments from neutron-induced fission of U^{238} and Th^{232}**. *Physical Review*, **103**:1292–1295, 1956.

[36] R. Kroning R. et al. **The symmetrical top in the undalotary mechanic**. *Physical Review*, **29**:262, 1927.

[37] E. P. Wigner. *Group Theory and its application to the quantum mechanics of atomic spectra*. Academic press, 1959.

[38] C. Rubbia et al. **A HIGH RESOLUTION SPALLATION DRIVEN FACILITY AT THE CERN-PS TO MEASURE NEUTRON CROSS SECTIONS IN THE INTERVAL FROM 1 eV TO 250 MeV: A RELATIVE PERFORMANCE ASSESSMENT**. *No. CERN-LHC-98-002-EET-Add. 1*, 1998.

[39] E. Berthoumieux et al. **The neutron Time-Of-Flight facility nTOF at CERN (I): Technical Description**. *nTOF-PUB-2013-001*, 2013.

[40] U. Abbondanno et al. **CERN nTOF facility: performance report**. *CERN/INTC-O-011*, 2010.

[41] C. Weiss et al. **The new vertical neutron beam line at the CERN n_TOF facility design and outlook on the performance**. *Nuclear Instruments and Methods in Physics Research Section A*, **799**:90–98, 2015.

[42] M. Barbagallo et al. **High-accuracy determination of the neutron flux at n_TOF** . *The European Physical Journal A*, **49**:156, 2013.

[43] M. Sabate-Gilarte et al. **High-accuracy determination of the neutron flux in the nex experiemntal area EAR2-n_TOF at CERN**. *The European Physical Journal A*, 2017(in press).

[44] C. Guerrero et al. **Performance of the neutron time-of-flight facility n_TOF at CERN**. *The European Physical Journal A*, **49**:27, 2013.

[45] J. Lerendegui-Marco et al. **Geant4 simulation of the n_TOF -EAR2 neutron beam: Characteristics and prospects**. *The European Physical Journal A*, **52**:100, 2016.

[46] M. Fatyge et al. **Linear momentum transfer in 40-150 MeV proton-induced reationS with** ^{238}U. *Physical Review C*, **32**(5):1496–1505, 1985.

[47] A. Breskin et al. **A Simple and accurate method for bidimensional position read-out of parallel plate avalanche counters**. *Nuclear Instruments and Methods*, **146**:461–463, 1977.

[48] J. Pancin et al. **Measurement of the n_TOF beam profile with a micromegas detector**. *Nuclear Instruments and Methods in Physics Research Section A*, **524**:102–114, 2004.

[49] C. Guerrero et al. **The n_TOF Total Absorption Calorimeter for neutron capture measurements at CERN**. *Nuclear Instruments and Methods in Physics Research Section A*, **608**:424–433, 2009.

[50] C. Lederer et al. $^{197}Au(n,\gamma)$ **cross section in the unresolved resonance region**. *Physical Review C*, **83**:034608, 2011.

[51] April 2017. `http://castor.web.cern.ch`.

[52] April 2017. `https://root.cern.ch`.

[53] *Fission fragment angular distribution and fission cross section validation.* PhD thesis, Université Paris Sud, 2013.

[54] *Measurement of the U-234(n,f) cross section with PPAC detectors at the n_ TOF facility.* PhD thesis, Universidad de Santiago de Compostela, 2005.

[55] T. Fukahori and A. Yu. Konobeyev. **JENDL/HE-2007**.

[56] G.A. Tutin et al. **An ionization chamber with Frisch grids for studies of high-energy neutron-induced fission**. *Nuclear Instruments and Methods in Physics Research Section A*, **457**:646–652, 2001.

[57] M. Diakaki et al. **Determination of the ^{237}Np(n, f) reaction cross section for En = 4.5-5.3 MeV, using a MicroMegas detector assembly**. *The European Physical Journal A*, **49**:62, 2013.

Résumé en français

1. Installation

L'installation de temps de vol de neutrons n_TOF au CERN est basée sur une source de spallation constituée d'une cible épaisse de plomb bombardé e par des protons de 20 GeV/c. C'est une installation unique au monde pour la mesure de données nucléaires en raison de sa gamme étendue en énergie des neutrons (du thermique à 1 GeV) et de sa haute résolution en énergie. Deux lignes de faisceau y sont actuellement utilisables. La première est horizontale avec une longueur de vol de ∼185 mètres envoyant des neutrons dans l'aire expérimentale 1 (EAR-1), la seconde est verticale aboutissant à l'aire expérimentale 2 (EAR-2) située à ∼20 mètres de la cible de spallation.

2. Détecteurs et cibles de mesure

Le système de mesure est basé sur des détecteurs à plaques parallèles à avalanche (PPAC) qui sont des détecteurs gazeux utilisant du C_3F_8 à la pression de ∼4 mbar. Chacun est constitué d'une anode centrale et de deux cathodes, situées de part et d'autre. Quand une particule chargée traverse le détecteur l'anode délivre un signal rapide donnant l'instant de passage et les cathodes mesurent les positions et Y à l'aide de lignes à retard.

Les cibles de mesure sont très minces, de l'ordre de centaines de $\mu g/cm^2$. Elles sont électro-déposées sur de minces feuilles d'aluminium (2 ou 0.7 μm). Les cibles et leurs supports doivent être très minces pour permettre la sortie des deux fragments de fission, la mesure étant basée sur leur détection en coincidence.

3. Mesures

Dans ce travail de thèse un expérience sur chacune des lignes de faisceau a été réalisée. La première a été réalisée à EAR-2 pour la mesure des propriétés du faisceau de neutron (flux de neutrons, forme du profil). La seconde, réalisée à EAR-1, était dédiée à la mesure de la section efficace de fission de ^{237}Np et à la distribution angulaire des fragments de fission (FFAD).

- **Caractéristiques du faisceau à EAR-2**

EAR-2 était construit depuis 2014 et encore en cours de caractérisation. C'est une nouvelle ligne de faisceau en complément de EAR-1 avec sa particularité d'un flux de neutron élevé: environ 40 fois plus fort qu'à EAR-1. Elle étend les possibilités de mesure à n_TOF pour des échantillons accessibles seulement en quantité très réduite ou ayant de faibles sections efficaces. Avec la mise en service de EAR-2 il était urgent de connaître ses caractéristiques pour la définition des expériences et leur analyse, le flux de neutrons étant d'une importance particulière. Notre système de PPAC est un bon candidat pour effectuer ces mesures en raison du temps de réponse rapide, de la bonne résolution en temps et donc en énergie, et de la capacité de localisation. Nous avons donc développé un moniteur PPAC (PPACmon) pour caractériser les propriétés du faisceau à EAR-2.

Le PPACmon contient trois détecteurs PPAC et deux cibles de ^{235}U perpendiculaires au faisceau de neutrons, chaque cible étant située entre deux PPAC. Quand un neutron incident induit une fission dans une des deux cibles les deux fragments sont émis à 180° l'un de l'autre. Cette fission est identifiée par la détection simultanée des deux fragments. Cette méthode est particulièrement sélective des fissions, rejetant la plupart des évènements de bruit de fond provenant des réactions autres que la fission, abondantes à haute énergie dans le domaine de la spallation.

Après sélection d'un évènement de fission l'énergie du neutron l'ayant produit est déterminé par temps de vol (TOF) et on obtient le nombre de fissions en fonction de l'énergie des neutrons. Comme l'efficacité de détection des PPAC ne dépend pas de l'énergie des neutrons, elle a été considérée comme constante sur la gamme en énergie traitée. La dépendance en énergie du flux est alors obtenue en divisant le nombre de fissions en fonction de l'énergie par la section efficace de fission de ^{235}U extraite des

bases de données. The flux absolu résulte de la normalisation de cette dépendance par rapport à d'autres mesures donnant ce flux absolu sur certains domaines en énergie.

La position des fragments traversant les PPAC est enregistrée et il est donc possible de reconstruire la trajectoire de fission en supposant une émission à 180°. On peut ainsi remonter au point d'émission sur la surface de cible étendue. La distribution des points d'émission est représentative de la forme géométrique du flux de neutrons car les cibles d'émission ont une bonne homogénéité.

- **Mesure de ^{237}Np(n, f) à EAR-1**

Le ^{237}Np est un isotope abondamment produit dans les réacteurs actuels et est un actinide mineur de longue durée de vie actuellement présent dans les déchets. Il pourrait à ce titre est un candidat à l'incinération dans des réacteurs à neutrons rapides. Une telle perspective réclame une connaissance précise de son interaction avec les neutrons en particulier sa section efficace de fission. Pour cette raison cette section efficace a fait l'objet de plusieurs mesures dans les dix dernières années auprès de diverses installations. La plus récente, réalisée à n_TOF au CERN en 2010, apparaît comme 6% plus élevée que la plupart des mesures et les bases de données. Cette singularité pourrait mettre en doute sa validité, cependant certains points plaident en faveur d'une section efficace plus élevée que celle contenue dans les bases de données : 1) les sections efficaces préalablement mesurées reposent souvent sur des normalisations mutuelles à certaines énergies, 2) les expériences de criticité sont mieux reproduites avec le jeu de données de n_TOF . La situation a donc besoin d'être clarifiée et une mesure absolue et précise de la section efficace de ^{237}Np(n,f) est souhaitable.

La mesure de la section efficace de fission de ^{237}Np induite par neutrons a été réalisée à EAR-1. Le système utilise dix PPAC et neuf cibles de fission parmi lesquelles cinq cibles de ^{237}Np, deux cibles de ^{235}U et de ^{238}U utilisées comme références de section efficace permettant de déterminer le flux de neutrons. Les quantités d'atomes dans ces cibles ont été mesurées par comptage alpha dans une géométrie bien définie avec une précision inférieure à 1% essentiellement définie par l'angle solide. L'identification des fissions suit la même démarche que pour le PPACmon avec détection en coincidence des fragments et reconstruction de la trajectoire de fission.

La différence principale par rapport au PPACmon réside dans le fait que détecteurs et cibles sont inclinés à 45° par rapport au faisceau de neutrons. Au prix d'une plus

grande taille la mesure est moins sensible à la distribution angulaire des fragments (FFAD) et elle assure un découplage de l'efficacité de détection et de la distribution angulaire, le nombre de fissions à un angle donné étant proportionnel au produit de l'efficacité et de la distribution angulaire. On peut pour chaque fission définir deux angles polaires, le premier par rapport au neutron incident et noté $\cos\theta$, le second par rapport à la normale aux détecteurs et cibles et noté $\cos\theta'$. Un $\cos\theta'$ donné peut être atteint avec toute une gamme de $\cos\theta$, et tous ces évènements ont la même efficacité de détection, leur distribution est donc une représentation fidèle de la distribution angulaire (FFAD). On obtient ainsi la FFAD par morceaux. Réciproquement un même $\cos\theta$ est atteint par une gamme de $\cos\theta'$ et leur distribution est proportionnelle à l'efficacité de détection. Ceci rend possible la reconstruction de l'efficacité de détection par morceaux. Le système permet donc le découplage et la mesure séparée de l'efficacité de détection et de la distribution angulaire de fission.

Quand l'efficacité de détection est mesurée pour chaque cible, le rapport des sections efficaces ^{237}Np/^{235}U est extrait. Nous en avons finalement déduit la section efficace ^{237}Np(n,f) entre 1 et 5 MeV à partir de la section efficace standard de ^{235}U. Les valeurs ainsi obtenues sont 3-4% plus hautes par rapport à ENDF-BVII.0, mais 2.2% au-dessous de la mesure n_TOF de 2010.

4. Conclusion

- **Caractérisation du faisceau à EAR-2**

Le profil du faisceau ainsi que le flux de neutrons non normalisé ont été mesurés à EAR-2. Le profil met en évidence un halo autour du pic central. Il diffère du profil à EAR-1 qui est quasiment uniforme. C'est la conséquence des différences de conception du collimateur final et la parallaxe induite par des distances très différentes. Nous avons montré que le PPACmon peut contrôler le faisceau de neutrons depuis l'énergie thermique jusqu'à 200 MeV ce qui en fait le système de détection couvrant la plus grande gamme en énergie à n_TOF . En particulier il est le seul système de détection accédant à la partie haute énergie du spectre des neutrons, depuis quelques MeV jusqu'à 200 MeV.

- **Mesure de ^{237}Np(n,f) à EAR-1**

Dans les mesures antérieures notre système ne permettait pas la mesure de l'efficacité de détection cible par cible et nous avions supposé que l'efficacité était la même pour les cibles de même épaisseur, support compris. Dans le présent travail de thèse l'inclinaison à 45° permet de résoudre le problème et apporte un bon contrôle de l'efficacité cible par cible. Nous avons trouvé que des éléments cibles différents donnaient des efficacités différentes malgré une épaisseur similaire. Les causes en sont la rugosité différente du dépôt ainsi que la composition chimique différente, une teneur plus grande en oxygène et hydrogène (eau, radicaux OH) ralentissant plus les fragments de fission. Il s'agit donc d'une amélioration significative du système de détection par rapport à la version antérieure.

Les premiers résultats de la section efficace ^{237}Np(n,f) de 1 à 5 MeV sont obtenus en relatif à ^{235}U en utilisant ENDF/B-VII.0 comme référence. Les valeurs sont 2-3% plus basses que la mesure précédente obtenue en 2010 à n_TOF avec le système de PPAC, en raison de la correction d'efficacité. Elles restent supérieures de 3-4% par rapport à l'évaluation ENDF/B-VII.0. Le résultat est donc cohérent avec les mesures de criticité qui demandent une section efficace ^{237}Np(n,f) supérieure à celle des bases de données, bien que légèrement inférieure à celle de la mesure antérieure avec le système de PPAC.

université PARIS-SACLAY | ÉCOLE DOCTORALE PHENIICS

Titre : Caractérisation de la nouvelle ligne de neutron à n_TOF CERN, et étude de la fission induite par neutrons de ^{237}Np

Mots clés : fission, neutron, détecteur gazeux, n_TOF

Résumé : L'installation n_TOF au CERN est une source pulsée de neutrons, unique au monde pour la mesure de données nucléaires sur le spectre en énergie le plus étendu, avec deux lignes actuellement exploitées. Une ligne horizontale alimente l'aire expérimentale 1 (EAR-1) avec une base de vol de ~185 mètres. La seconde ligne est verticale et alimente l'aire 2 (EAR-2) à ~20 mètres de la cible de production

La première partie de ce travail de thèse concerne la caractérisation du faisceau de neutrons (flux, profil géométrique, spectre en énergie) de la nouvelle ligne EAR-2, particulièrement importante pour la définition des expériences et leur analyse. Une mesure a été réalisée à EAR-2, basée sur des détecteurs PPAC enregistrant la fission de ^{235}U, à partir de laquelle nous avons obtenu le profil et le flux sur la gamme en énergie accessible (thermique à 200 MeV).

La seconde partie de la thèse a pour but l'étude de la fission de ^{237}Np. Cet isotope est abondamment produit dans les réacteurs nucléaires actuels et est un des constituants des déchets à vie longue. A ce titre on peut le considérer comme une cible potentielle pour l'incinération en réacteur rapide. Ceci a motivé des mesures récentes de sa section efficace de fission. Cependant des déviations importantes sont apparues, en particulier la mesure effectuée à n_TOF en 2010 est 6% supérieure aux évaluations basées sur les mesures antérieures. Ceci a motivé une nouvelle mesure à n_TOF avec une configuration permettant une mesure précise de l'efficacité de détection, pour apporter une réponse au problème. Ce travail a permis de mettre en évidence une dépendance de l'efficacité de détection avec l'élément, résultant des conditions de l'électrodéposition. Après application de cette correction d'efficacité dans la région 1 à 5 MeV la section efficace de fission ainsi extraite est 2 à 3% plus petite par rapport à la mesure de 2010, cependant elle reste 3 à 4% plus forte que les évaluations.

Title : Characterization of the new neutron line at CERN-n_TOF and study of the neutron-induced fission of ^{237}Np

Keywords : fission, neutron, gaseous detector, n_TOF

Abstract : The neutron time-of-flight (n_TOF) facility at CERN is a unique worldwide pulsed neutron source to measure the nuclear data over the widest energy range with two beam lines currently exploited. One is horizontal with a ~185 meters flight path, sending neutrons to experimental area-1 (EAR-1). The second one is a new line sending neutrons vertically to experimental area-2 (EAR-2) with a ~20 meters flight path.

The first part of this PhD work is dedicated to the characterization of the beam (flux, geometrical profile, energy spectrum) of the new EAR-2 neutron beam, of the utmost importance for the experimental proposals and analyses. An experiment was carried out at EAR-2, based on PPAC detectors looking at fission of ^{235}U, and the beam profile and neutron flux have been obtained for the entire available energy range (from thermal to 200 MeV).

The second part of the thesis aims to study the neutron-induced fission of ^{237}Np. ^{237}Np is abundantly produced in present nuclear reactor and is one of the major long-lived components of nuclear waste which can be considered as a potential target of incineration in fast neutron reactors. Consequently its neutron-induced fission cross section has been measured at different facilities. However, significant discrepancies exist between different experiments. Especially, the recent one performed at n_TOF in 2010 is about 6% higher by comparison to the evaluation data based on previous experiments. Therefore an experiment has been performed at n_TOF EAR-1 to measure its fission cross section, in a configuration allowing an accurate control of the detection efficiency, aiming to give a definite answer to the puzzle. In this work, we found that the efficiencies for different target elements are different, even though they have similar thickness, reflecting the conditions of electrodeposition. After application of this efficiency correction in the energy range from 1 to 5 MeV, the newly extracted fission cross section is 2-3% lower compared with our previous measurement in 2010, however they are 3-4% higher than the evaluation.

Université Paris-Saclay
Espace Technologique / Immeuble Discovery
Route de l'Orme aux Merisiers RD 128 / 91190 Saint-Aubin, France